Supporting information for

Inhibition of 14-3-3/Tau by hybrid small-molecule-peptides operating via two different binding modes.

Sebastian A. Andrei,[†ξ] Femke A. Meijer,[†ξ] João Filipe Neves,[§] Luc Brunsveld,[†] Isabelle Landrieu,[§] Christian Ottmann,[†ζ]* and Lech-Gustav Milroy[†]**

† Department of Biomedical Engineering and Institute of Complex Molecular Systems, Laboratory of Chemical Biology, Technische Universiteit Eindhoven, Den Dolech 2, 5612 AZ Eindhoven, The Netherlands

§ UMR 8576 CNRS-Lille University, 59000 Villeneuve d'Ascq, France

ζ Department of Chemistry, University of Duisburg-Essen, Universitätsstrasse 7, 45117 Essen, Germany

ξ These authors contributed equally to the work.

Co-crystal structures of 14-3-3 and modified Tau peptides

First, the structural data of modified Tau peptides **4.2e-I**, **4.2f-I** and **4.2f-II** in complex with 14-3-3 are described in detail and the binding modes are compared.

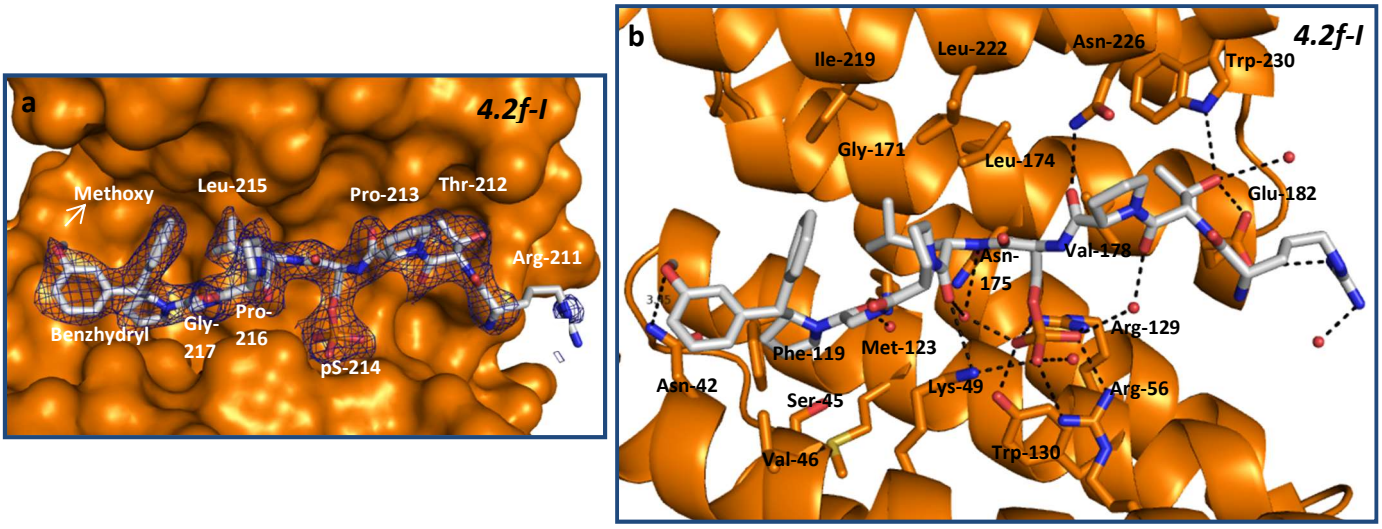

Figure S1. A) Crystal structure of the **4.2f-I** peptide (white sticks) in complex with 14-3-3σ (orange surface). The 2Fo-Fc electron density (contoured at 1σ) is shown as a blue mesh. B) Overview of the polar contacts (black dashed lines) between **4.2f-I** (white sticks) and 14-3-3σ (orange cartoon). Water molecules are shown as raspberry red spheres.

The structure of **4.2f-I** (methoxy substituent at the *meta*-position) in complex with 14-3-3σ (shown in Figure S1A) was solved with a resolution of 1.40 Å. Figure S1B shows a more detailed picture of the interactions between the modified peptide and the residues in the binding groove of 14-3-3σ. The N-terminal residues of the peptide (Arg-211, Thr-212, Pro-213) interact with 14-3-3σ specifically via polar contacts (depicted with dashed lines). The basic amino acid residues Arg-56, Arg-129, Lys-49, and Tyr-130 of 14-3-3 coordinate the binding of the phosphate group (pS-214) into the pocket via ionic interactions and hydrogen bonds, which is the standard binding mode of a phospho-peptide interacting with 14-3-3. The C-terminal portion of the peptide (Leu-215, Pro-216, Gly-217) interacts with the protein primarily via

hydrophobic interactions with hydrophobic residues on Helix 7 and 9 of 14-3-3 (e.g. Ile-219, Leu-222, Leu-174). At the C-terminus of the peptide, the electron density for the methoxy-substituted benzhydryl pyrrolidine moiety can be clearly observed (Figure S1A). This moiety binds to 14-3-3 in an open mode – in contrast to the closed binding mode of the unsubstituted benzhydryl Tau peptide **3.2a** –[1] and does not address the deep-lying hydrophobic Phe-119/Met-123/Lys-122 pocket. Nevertheless, the oxygen of the methoxy substituent is located at a distance of 3.1 Å from Asn-42 at Helix 3 (Figure S1B), which enables the formation of a hydrogen bond between the substituent of the benzhydryl moiety and this asparagine residue.

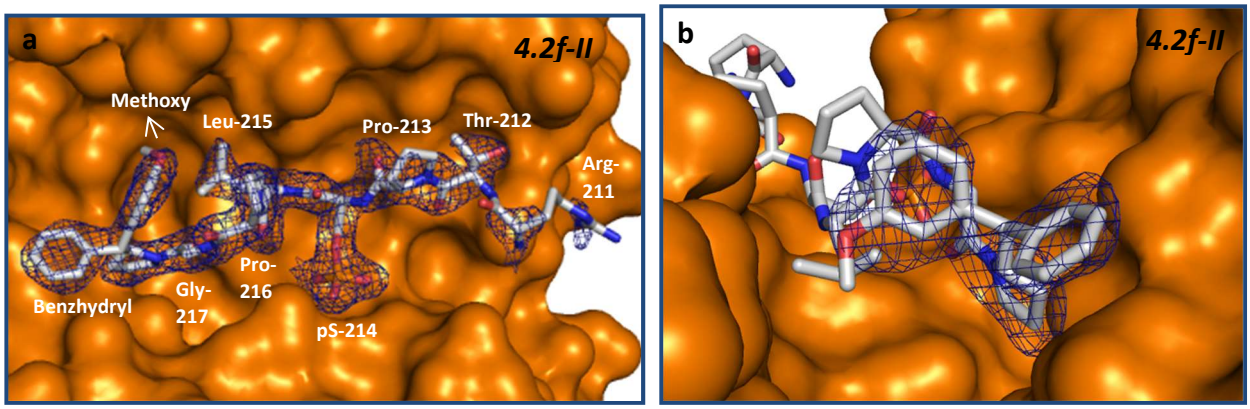

Figure S2. A) Crystal structure of the **4.2f-II** peptide (white sticks) in complex with 14-3-3σ (orange surface). The 2Fo-Fc electron density (contoured at 1σ) is shown as a blue mesh. B) Enlarged picture of the crystal structure of **4.2f-I** (white) in complex with 14-3-3σ (orange). The electron density for the substituted benzhydryl moiety (SR) is shown as a blue mesh.

In Figure S2A, the structure of **4.2f-II** (methoxy substituent at the meta-position) in complex with 14-3-3σ is shown, which was solved with a resolution of 1.45 Å. It is interesting to compare this structure with the structure of **4.2f-I** since these are two different diastereomers of the same methoxy-substituted benzhydryl (at the meta position), coupled to the Tau peptide epitope. The peptide **4.2f-II** itself interacts with 14-3-3 in a similar way as **4.2f-I**, with similar polar contacts and hydrophobic interactions, except the Leu-215 residue appears to have a

slightly different orientation. Again, the substituted benzhydryl pyrrolidine moiety binds to 14-3-3 in an open mode, and does not address the deep-lying Phe-Met-Lys pocket (Figure S2B). In comparison with **4.2f-I**, a clear difference in the orientation of the methoxy substituent can be observed. For **4.2f-I**, the methoxy substituent is oriented toward Helix 3 and 5 of 14-3-3, potentially making an interaction with Asn-42. By contrast for **4.2f-II**, the methoxy substituent is oriented toward Helix 7 and 9 and is not able to form a specific interaction with the protein. This might also explain the difference in binding affinity between **4.2f-I** and **4.2f-II**, since the affinity of the former was measured to be between 2- (FP) and 3.5-fold (ITC) higher than the latter.

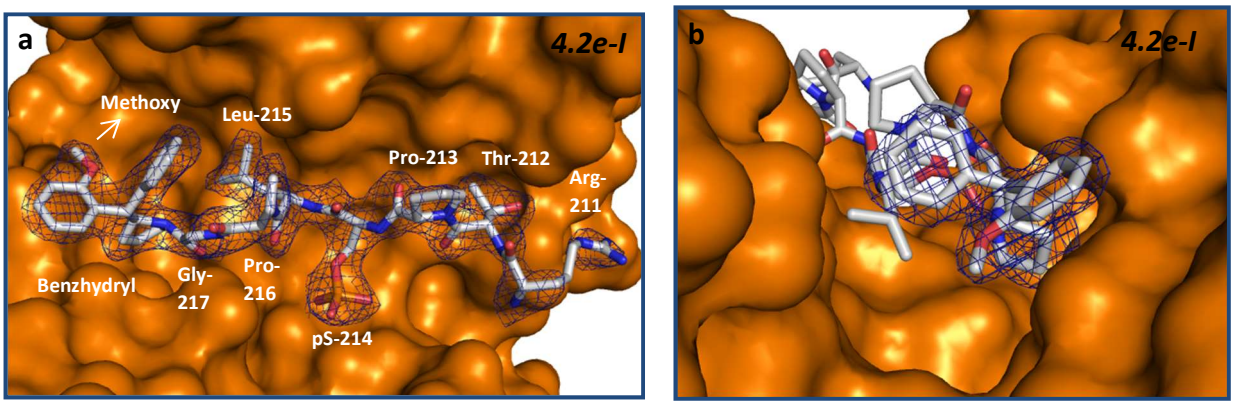

Figure S3. A) Crystal structure of the **4.2e-I** peptide (white sticks) in complex with 14-3-3σ (orange surface). The 2Fo-Fc electron density (contoured at 1σ) is shown as a blue mesh. B) Enlarged picture of the crystal structure of **4.2e-I** (white) in complex with 14-3-3σ (orange). The electron density for the substituted benzhydryl moiety (SS) is shown as a blue mesh.

The structure of **4.2e-I** (methoxy at the *ortho*-position) in complex with the 14-3-3 protein (Figure 3A), was solved with a resolution of 1.25 Å. For this structure, the peptide itself again binds in a similar mode as in the structures for **4.2f-I** and **4.2f-II** with similar polar and hydrophobic interactions. A notable difference is the Lys-49 residue of 14-3-3 which does not make an interaction with the phospho-residue in the case of **4.2e-I**. For the benzhydryl moiety

of **4.2e-I** (Figure S3B), the same binding mode was observed as for **4.2f-I**, with a similar orientation of the ortho methoxy substituent.

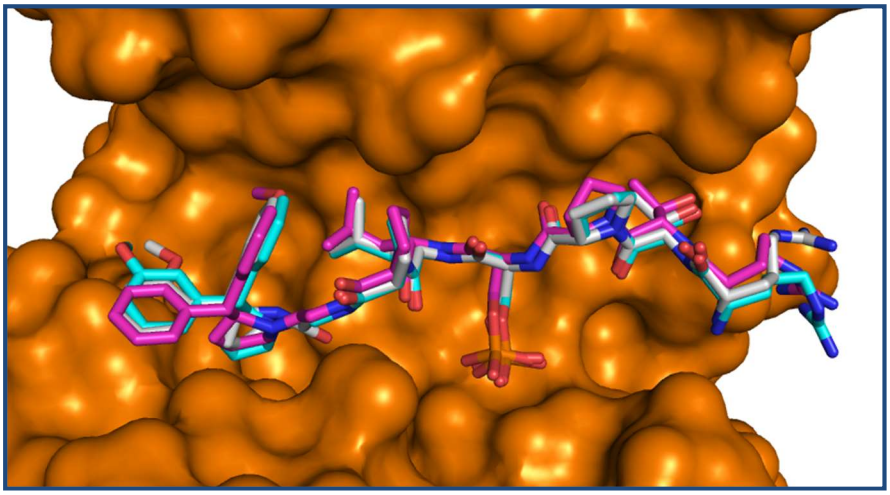

Figure S4. A) Overlay of the crystal structures of modified peptides **4.2e-I** (white)**, 4.2f-I** (cyan), **4.f-II** (pink) in complex with 14-3-3σ (orange).

In Figure S4, an overlay of the structure of the three different peptides is shown, in which it can be clearly observed that they all interact with 14-3-3σ in a similar way. Only small differences are observed for the Arg-211 residue, which is caused by its flexibility, and also for Leu-215 which appears to be rotated for **4.2e-I**. The substituted pyrrolidine benzhydryl moiety shows a clearly similar binding mode.

Comparison of the crystal structures of 4.2e-I, 4.2f-I and 4.f-II with the structures of other modified Tau peptides

In order to further explain the structure-activity relationship of the modified Tau peptides, the previous crystal structures were compared with previously published Tau-derived peptides (described by Milroy *et al*)[1] in complex with 14-3-3. **4.2f-I** is used as an example in the different

overlays of the crystal structures in this section and is representative for all the three peptides (**4.2e-I**, **4.2f-I** and **4.2f-II**), since they have the same binding mode.

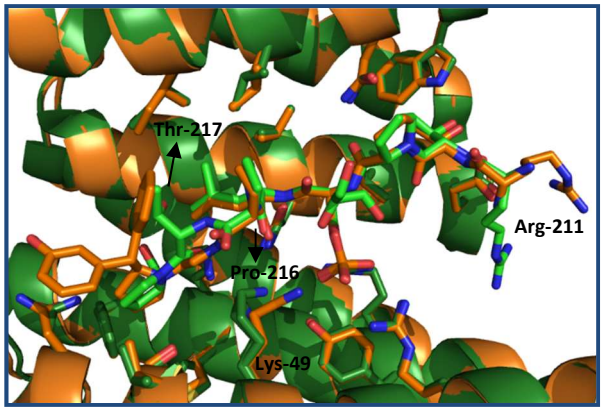

Figure S5. Overlay of the crystal structures of peptide **4.2f-I** (orange) and the Tau epitope (green) (PDB: 4FI5) in complex with 14-3-3σ.

First, the binding mode of **4.2f-I** is compared with the original Tau epitope, which is similar to **4.2f-I** but without a benzhydryl moiety at the C-terminus. In Figure S5, an overlay of these two peptides in complex with 14-3-3 is shown. The conformations of both the peptide and the protein are mostly similar, except for small differences in Arg-211 of the peptide and Lys-49 of the protein because of high flexibility. The conformation of the C-terminal part of the peptides – from the Pro-216 moiety – becomes more different. At position 217, a threonine residue is present in the Tau epitope which points towards Helix 7 and 9 of the 14-3-3 protein, while in the case of **4.2f-I**, a glycine residue is present at the same position, which results in a slightly different binding mode. Interestingly, one of the phenyl rings of the benzhydryl moiety of **4.2f-I** is oriented at the same position in the binding groove as the threonine residue of the tau epitope.

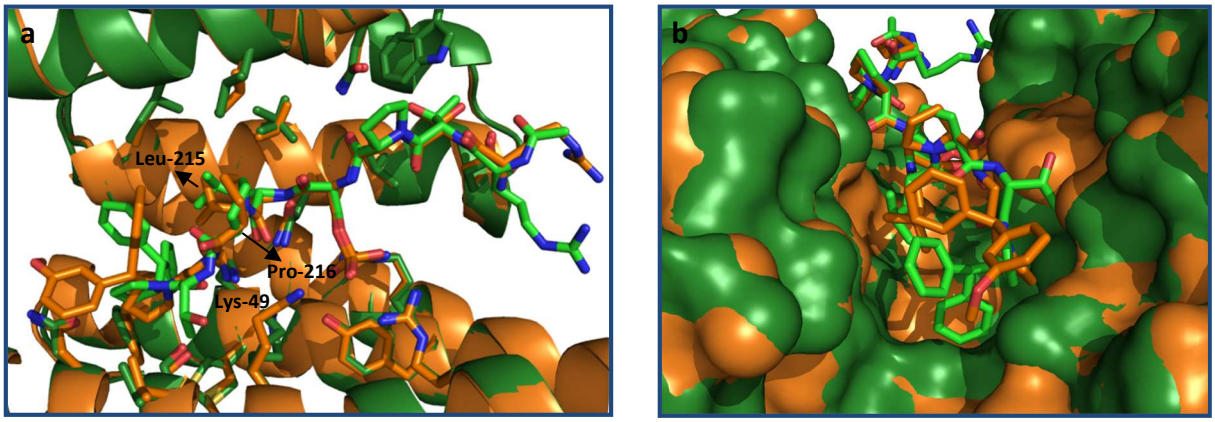

Figure S6. Overlay of the crystal structures of peptide **4.2f-I** (orange) and **3.2a** (green) (PDB: 4Y3B) in complex with 14-3-3σ.

In Figure S6A, **4.2f-I** is compared with **3.2a** (numbered **3b** in the reference),[1] which contains the unsubstituted benzhydryl moiety and a threonine residue at the C-terminus. Except for some minor differences in the protein (Lys-49) and in the peptide (Leu-215 & Pro-216), the structures are broadly similar. However, the benzhydryl pyrrolidine moiety exhibits a clearly different orientation as can be observed in Figure S6B. Since there are two differences between the peptides – the substituent and the glycine residue – both might cause the distinct binding mode of the benzhydryl moiety. The introduction of the methoxy substituent might result in a preferred open conformation because of sterics, which could prevent the moiety from binding into the deeper pocket. Besides, the glycine residue instead of the Threonine at the C-terminus could also affect the orientation of the moiety, because of the higher conformational flexibility of the glycine residue. In order to answer this question, it would be relevant to also elucidate the crystal structure of the peptide with a Glycine at the C-terminus, coupled to the benzhydryl moiety without a substituent. In this way it could be observed whether the benzhydryl moiety would also point upward in that case.

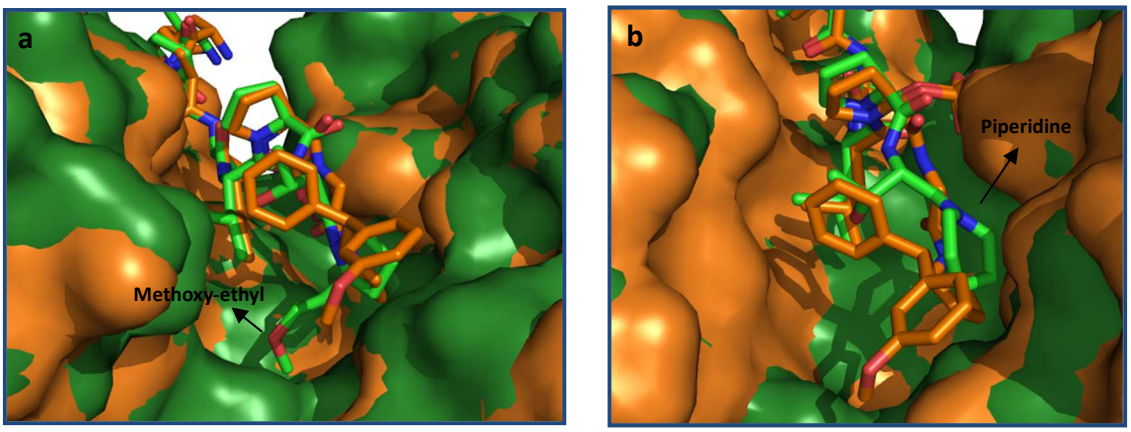

Figure S7. Overlay of the crystal structures of peptide **4.2f-I** (orange) and A) methoxy ethyl pyrrolidine (green) (PDB: 4Y32) and B) piperidine derivatives (PDB: 4Y5I) in complex with 14-3-3σ.[1]

Additionally, the structure of **4.2f-I** in complex with 14-3-3σ was compared to two other modified Tau-derived peptides, consisting of the Tau epitope modified with a methoxy ethyl pyrrolidine and with a piperidine moiety . The synthesis and biochemical and structural analysis of these peptides are described in Milroy *et al*. In Figure S7A it can be observed that methoxy ethyl pyrrolidine derivative (IC_{50} = 90.1 μM) binds in a similar way to 14-3-3, except for the C-terminal part. The methoxy ethyl pyrrolidine interacts with the deep Phe-Met-Lys pocket, similar to **3.2a**. An overlay of the structure of the piperidine derivative (IC_{50} = 301 μM) and **4.2f-I** is shown in Figure S7B, revealing that the piperidine moiety is more solvent exposed similar to the substituted benzhydryl pyrrolidine moiety.

An overlay of the substituted benzhydryl pyrrolidine moiety of **4.2f-I** was made with fusicoccin A (Figure S8, looking from the 14-3-3 protein binding groove). Interestingly, fusicoccin also interacts with Asn-42 via the oxygen in the ring of the glycosidic moiety (3.62 Å distance). Furthermore, the unsubstituted phenyl ring of the benzhydryl moiety occupies the same region of the 14-3-3 binding pocket as the hydrophobic part of fusicoccin. The OMe-substituent at the

A-ring of Fusicoccin clearly addresses the hydrophobic Phe-Met-Lys pocket. Besides, a clear difference in the conformation of 14-3-3 can be observed in this overlay: for fusicoccin-A there is a significant shift in the position of Helix 9, which is possibly caused to enable the formation of polar contacts between Asp-215 and fusicoccin.

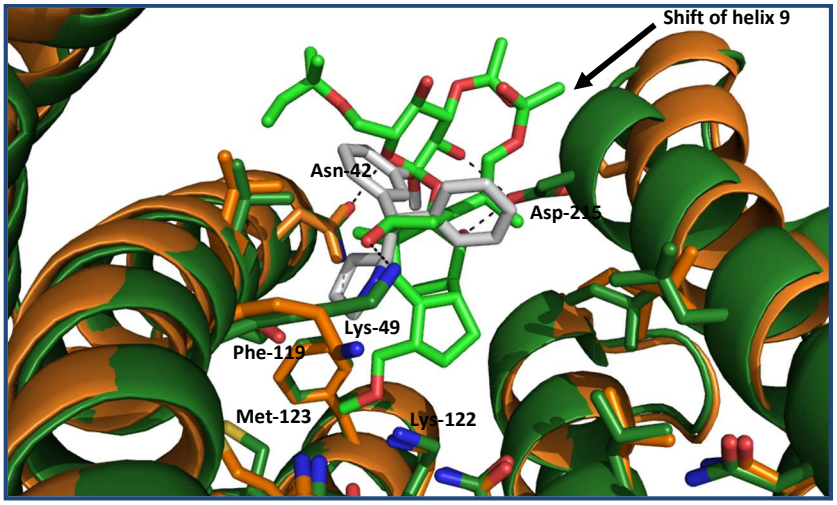

Figure S8. Overlay of the crystal structures of the benzhydryl moiety of peptide **4.2f-I** (white) and Fusicoccin-A (green) (PDB: 4JDD) in complex with 14-3-3σ (view: looking down the 14-3-3 binding groove). Polar contacts are shown as dashed lines.

The number of crystal structures available allowed us to perform an extensive comparison of the binding of the various C-terminally modified Tau peptides. The peptides modified with unsubstituted benzhydryls, **3.2d** (Figure S9) and **3.2e** (Figure S10), both exhibit a "closed fold", which is characterized by the pro-*S* benzhydryl phenyl ring being buried deep in a pocket formed by F119, I168, M123 and the hydrophobic part of K122. In doing so, the other phenyl moiety is positioned in close proximity to I219, further increasing the hydrophobic characteristics of this interaction. The D-alanine modified Tau peptide, **3.2d**, seems to adopt a slightly more closed state than **3.2e**. The C-terminal amino acids in this series contain an α-substituent, either L-valine or D-alanine, which forces K49 to adopt a more buried

conformation. Moving further N-terminal, proline and leucines residues of the peptide contact the hydrophobic “roof” formed by L174, I219 and I222 of 14-3-3, while simultaneously forming a hydrogen bond between the main chain of the Tau-derived peptide and N175 on 14-3-3. The phosphoserine is the deeply buried in the 14-3-3 phosphate binding pocket formed by R56, R129 and Y130. Next follows a hydrogen bond between the Tau main chain and residue N226 of 14-3-3, followed by a proline residue, which adopts slightly different conformations between **3.2d** and **3.2e**. This seems to be caused by the N-terminal threonine. This residue is buried deeply by hydrogen bonding with W230 and E182, firmly locking it into place. This residue is not seen in the **3.2e** structure, suggesting a higher flexibility in this case, though this crystal structure is of lesser quality in general.

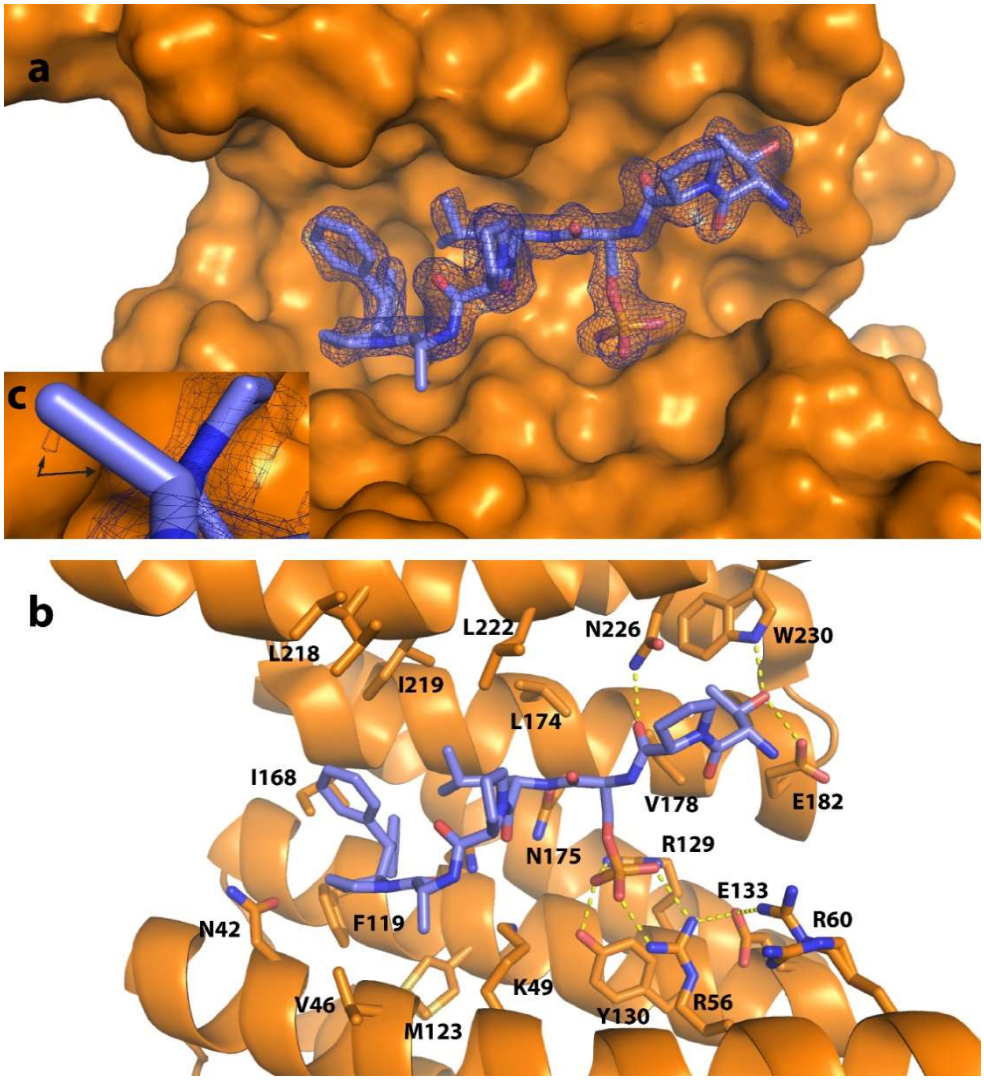

Figure S9. A) Crystal structure of the **3.2d** peptide (purple sticks) in complex with 14-3-3σ (orange surface). The 2Fo-Fc electron density (contoured at 1σ) is shown as a blue mesh. B) Overview of the amino acid residues (orange stick) in contact with **3.2d** with polar contacts indicated by yellow dashed lines. C) A zoomed in perspective of the side chain methyl group of the C-terminal D-alanine residues and associated electron density.

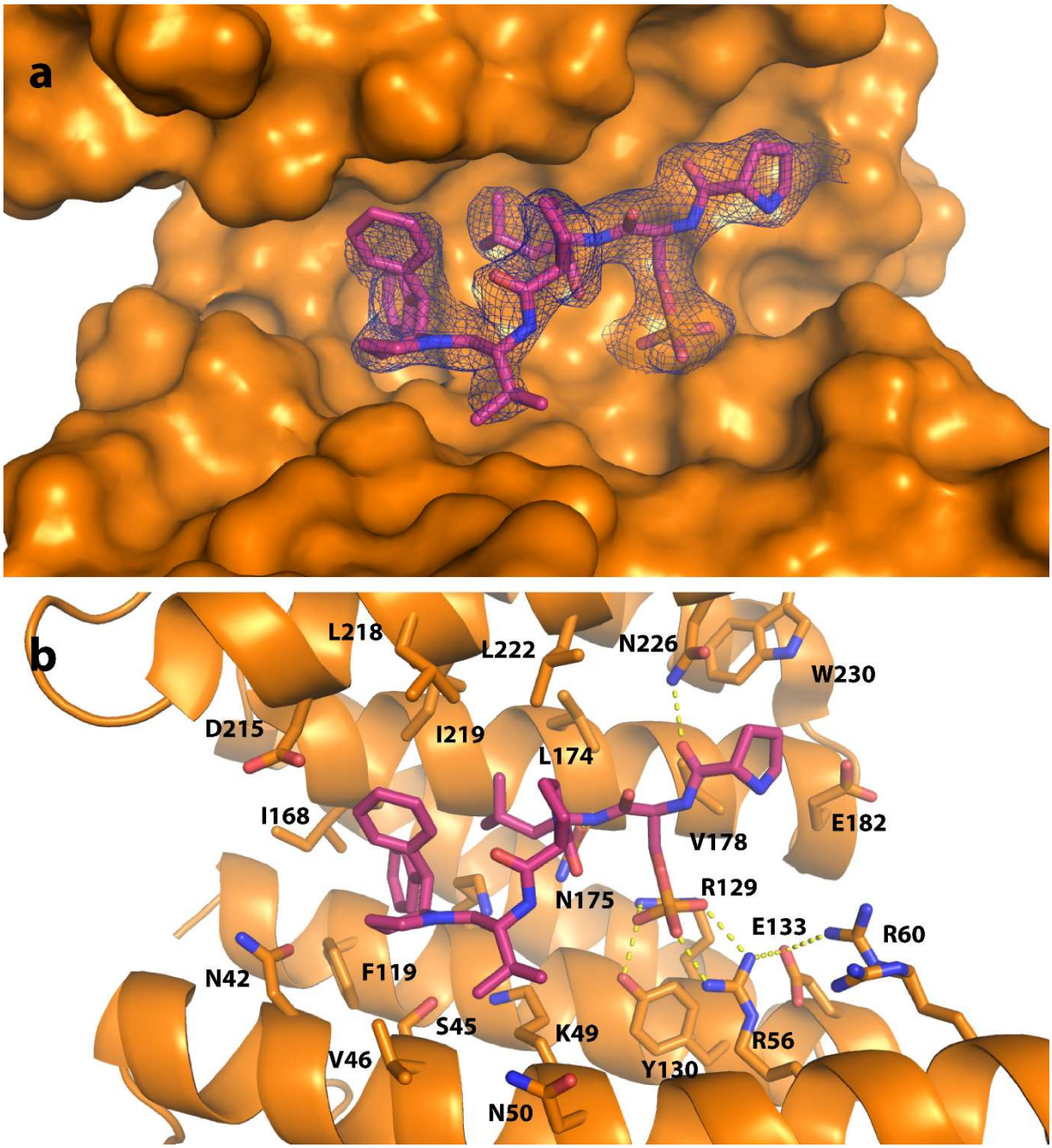

Figure S10. A) Crystal structure of the **3.2e** peptide (purple sticks) in complex with 14-3-3σ (orange surface). The 2Fo-Fc electron density (contoured at 1σ) is shown as a blue mesh. B) Overview of the amino acid residues (orange stick) in contact with **3.2e** with polar contacts indicated by yellow dashed lines.

Comparing these structures with the structures containing asymmetrically substituted benzhydryls, **4.2b** (Figure S11), **4.2c-I** (Figure S12), **4.2e-I** (Figure S13), **4.2f-I** (Figure S14) and **4.2f-II** (Figure S15), show very similar overall binding folds. The first major difference is the "open fold" of the benzhydryl moiety. As a result, the pro-*S* phenyl ring of the benzhydryl moiety now extends towards I219, leaving the deep pocket free. The second pro-*R* phenyl ring now slightly contacts V46, partially maintaining some hydrophobic contact. In the case of **4.2c-I** (Figure S12) the methoxyethoxy substituent is clearly seen in the electron density. Its terminal methoxide partially fills up the now open pocket by contacting I168. In the case of **4.2f-I** (Figure S14) a hydrogen bond is observed between the methoxy substituent and N42. Its diastereomer, **4.2f-II** (Figure S15) does not make this interaction, as the methoxy substituent is on the other benzhydryl ring. Its regioisomer **4.2e-I** (Figure S13) does bear the methoxy substitution on the correct ring, but the distance and angle between the methoxy oxygen and N42 are not compatible with hydrogen bonding.

The more open fold and the lack of an α-substituent on the C-terminal amino acid allow K49 to adopt a more extended, surface exposed conformation in these structures. Moving N-terminal, the overall fold of the peptide is identical to the unsubstituted structures. The only exception being the most N-terminal part, where the N-terminal arginine and sometimes the capping acetylation of the peptide can be observed in the electron density. This part of the peptide forms an elaborate hydrogen bonding network with the 14-3-3 protein residues W230 and E182. It must however be noted that these structures are generally of higher quality, so it is difficult to judge whether the visibility of the N-terminus is related to the substitution pattern of the benzhydryl modification.

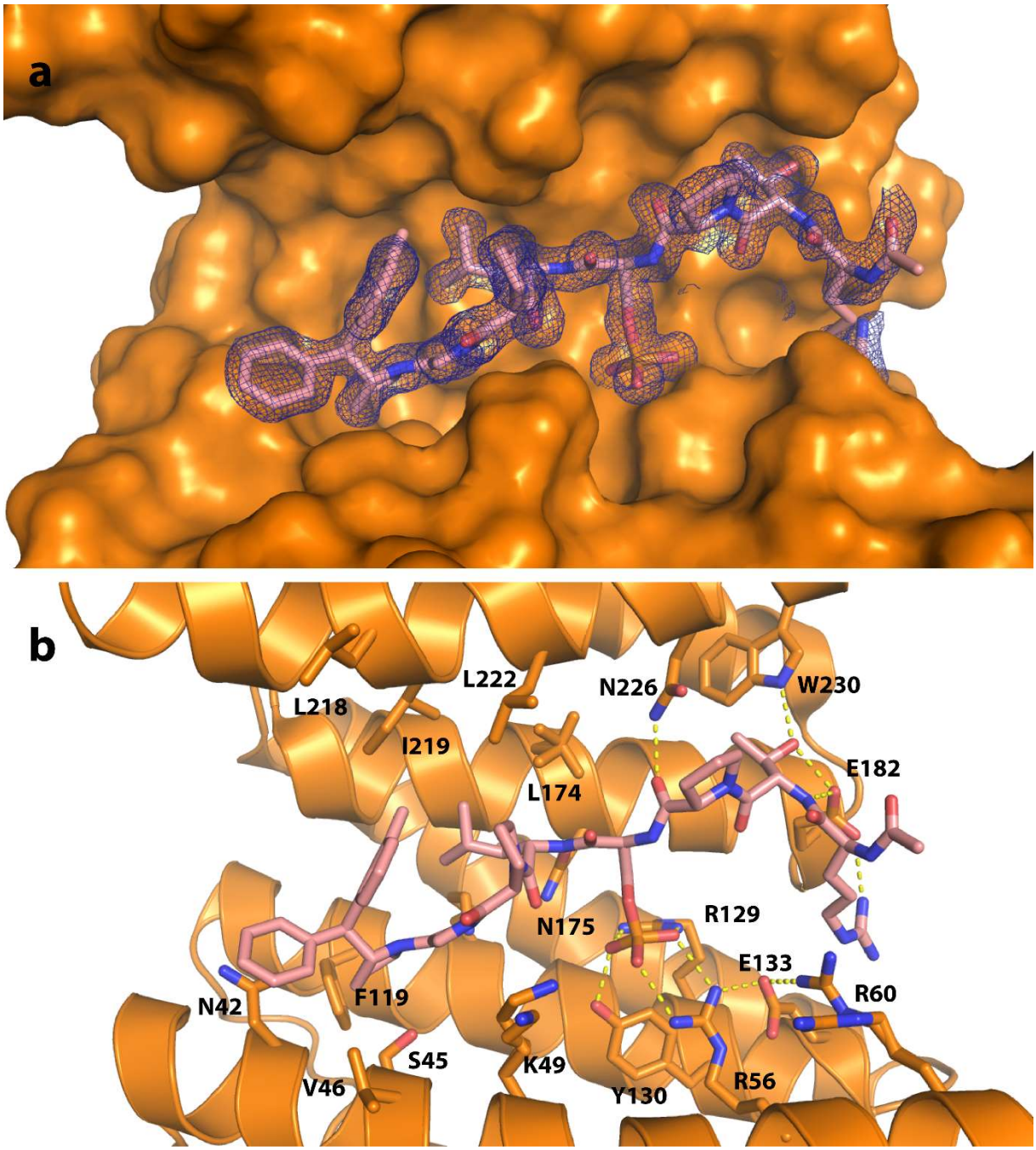

Figure S11. A) Crystal structure of the **4.2b** peptide (purple sticks) in complex with 14-3-3σ (orange surface). The 2Fo-Fc electron density (contoured at 1σ) is shown as a blue mesh. B) Overview of the amino acid residues (orange stick) in contact with **4.2b** with polar contacts indicated by yellow dashed lines.

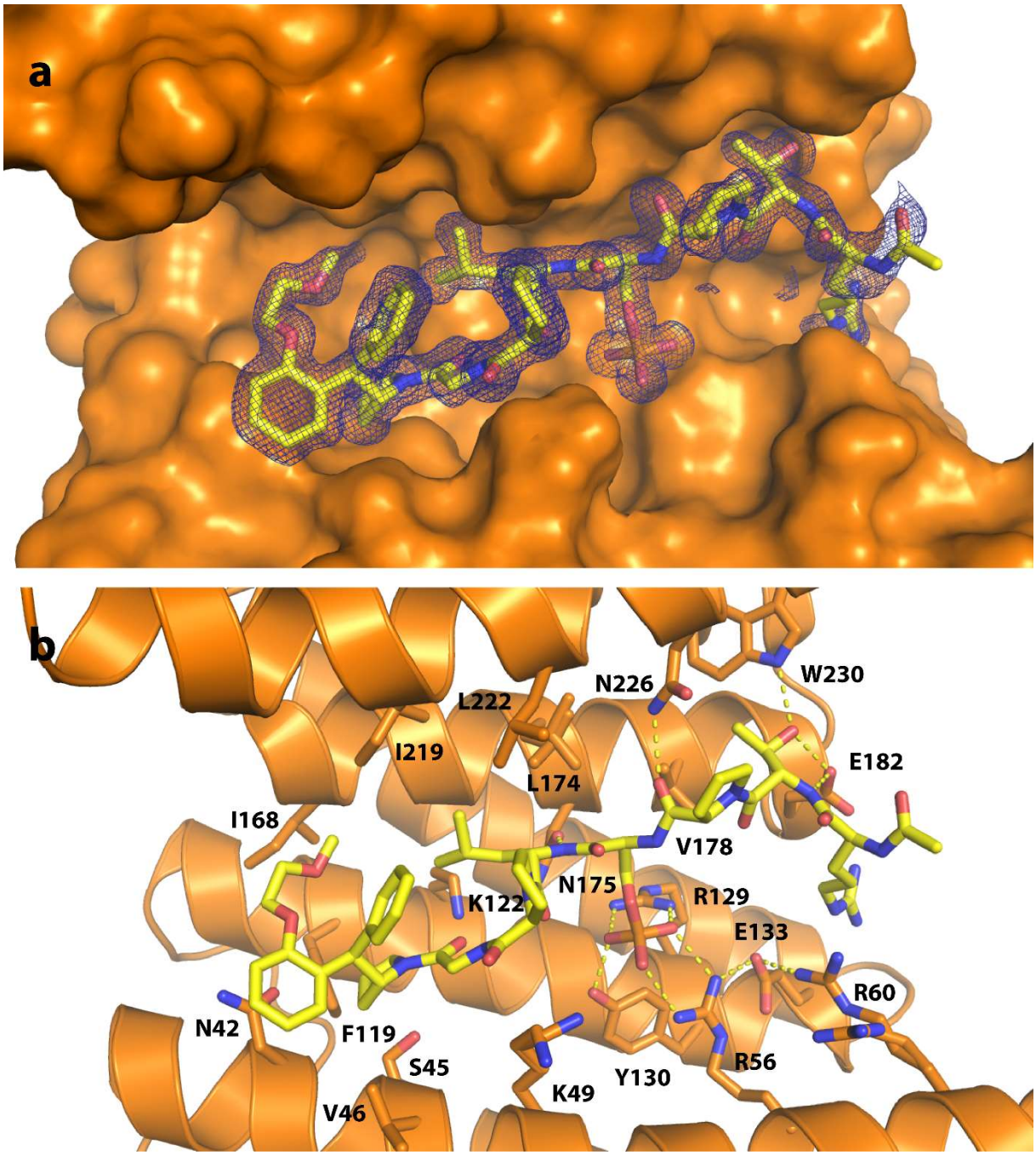

Figure S12. A) Crystal structure of the **4.2c-I** peptide (purple sticks) in complex with 14-3-3σ (orange surface). The 2Fo-Fc electron density (contoured at 1σ) is shown as a blue mesh. B) Overview of the amino acid residues (orange stick) in contact with **4.2c-I** with polar contacts indicated by yellow dashed lines.

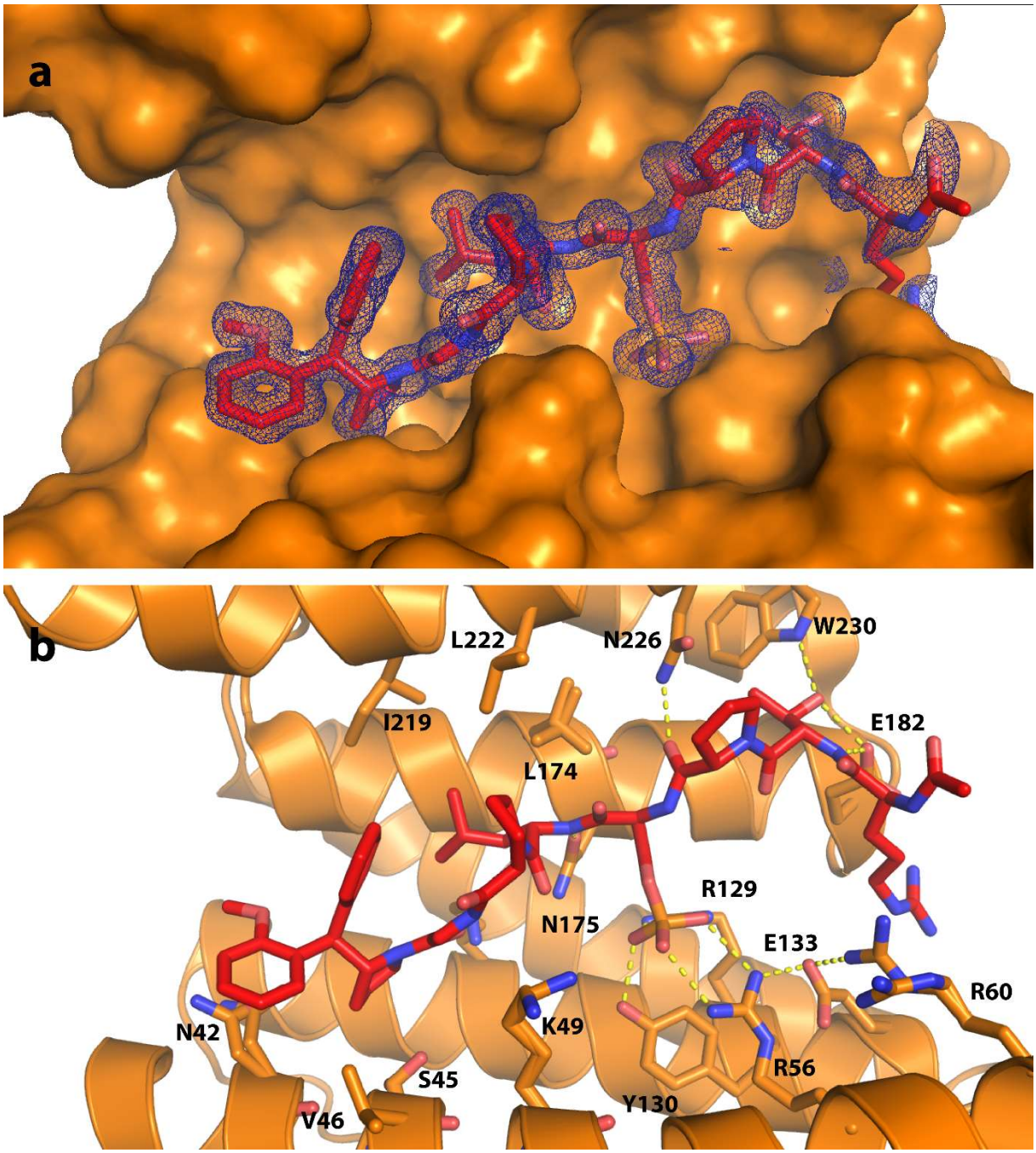

Figure S13. A) Crystal structure of the **4.2e-I** peptide (purple sticks) in complex with 14-3-3σ (orange surface). The 2Fo-Fc electron density (contoured at 1σ) is shown as a blue mesh. B) Overview of the amino acid residues (orange stick) in contact with **4.2e-I** with polar contacts indicated by yellow dashed lines.

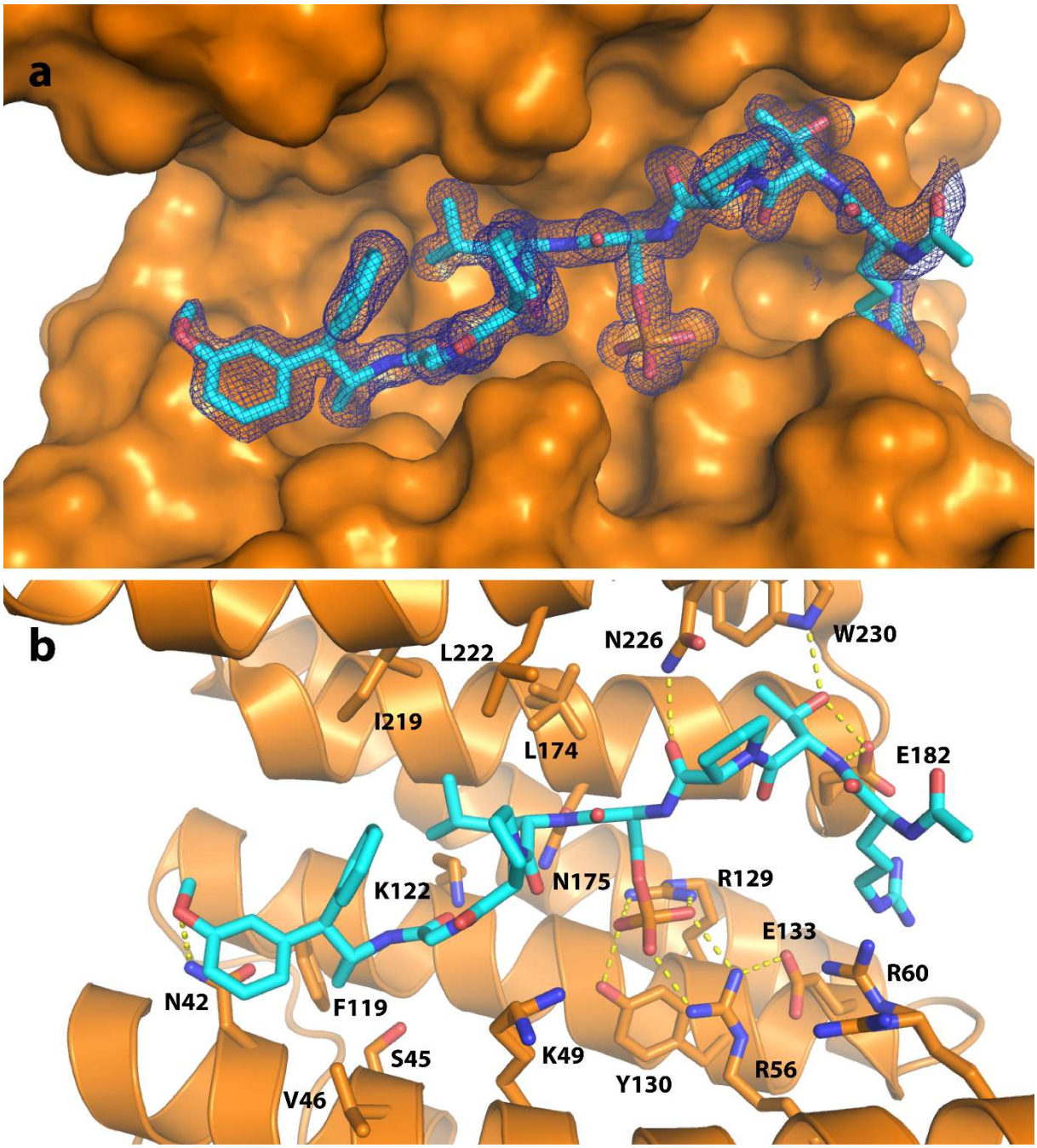

Figure S14. A) Crystal structure of the **4.2f-I** peptide (purple sticks) in complex with 14-3-3σ (orange surface). The 2Fo-Fc electron density (contoured at 1σ) is shown as a blue mesh. B) Overview of the amino acid residues (orange stick) in contact with **4.2f-I** with polar contacts indicated by yellow dashed lines.

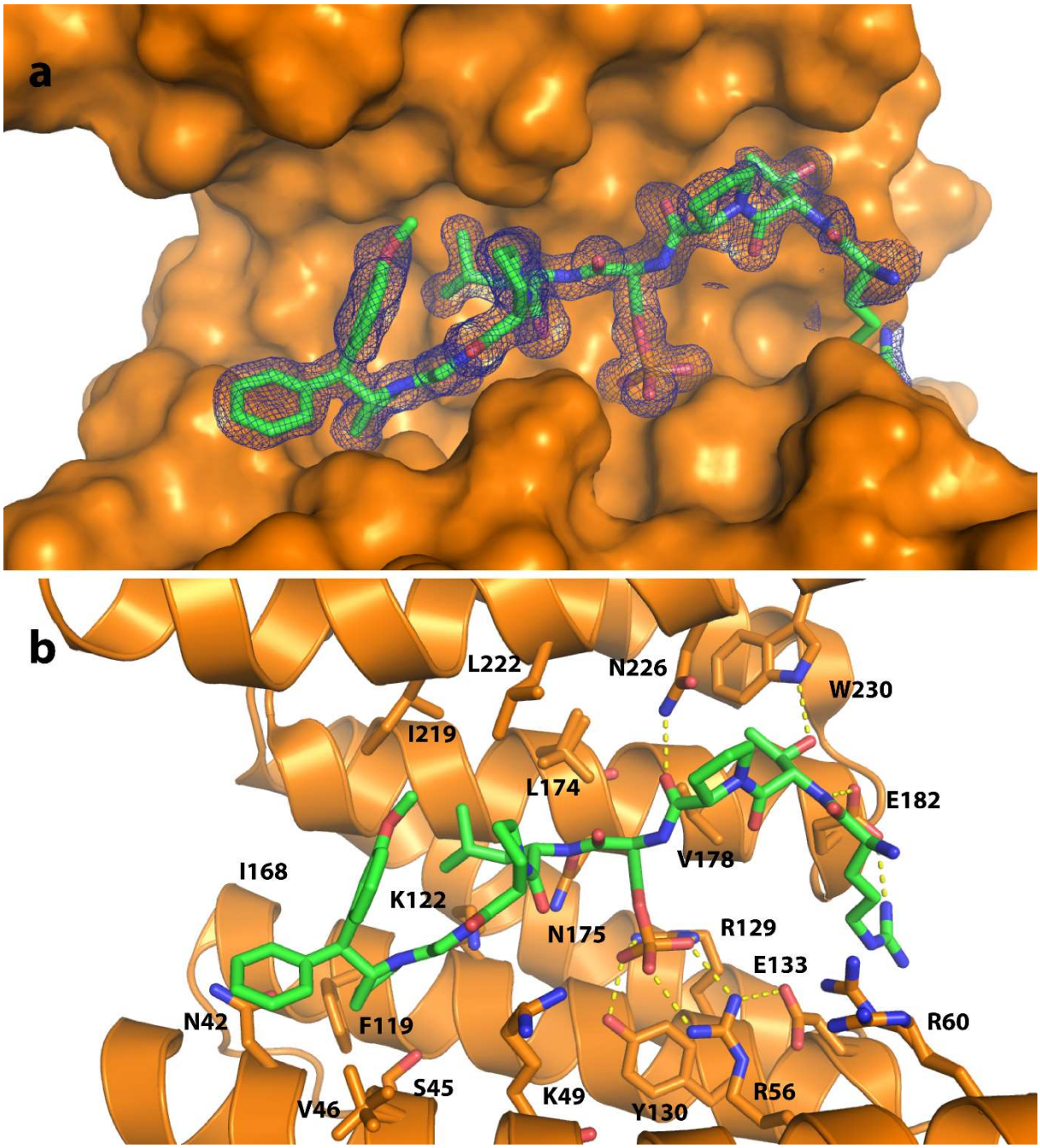

Figure S15. A) Crystal structure of the **4.2f-II** peptide (purple sticks) in complex with 14-3-3σ (orange surface). The 2Fo-Fc electron density (contoured at 1σ) is shown as a blue mesh. B) Overview of the amino acid residues (orange stick) in contact with **4.2f-II** with polar contacts indicated by yellow dashed lines.

Table S1. Data collection and refinement statistics of 4.2e-I, 4.2f-I and 4.2f-II with 14-3-3σ.

	3.2d	3.2e	4.2b	4.2c-I	4.2e-I	4.2f-I	4.2f-II
PDB code	6FI5	6FI4	6FBY	6FAW	6FAU	6FAV	6FBW
Data collection							
Resolution (Å)[a]	45.4 - 1.70 (1.73 - 1.70)	74.2 - 2.0 (2.05 - 2.00)	46.8 - 1.50 (1.53 - 1.50)	46.8 - 1.40 (1.42 - 1.40)	47.4 - 1.25 (1.27 - 1.25)	47.33 - 1.40 (1.42 - 1.40)	47.4 - 1.45 (1.47 - 1.45)
Space group	C 2 2 2	C 2 2 2	P 21 21 21	P 21 21 21	P 21 21 21	P 21 21 21	P 21 21 21
Cell parameters (Å)	a=81.93, b=112.21, c=62.36	a=62.38, b=148.5, c=78.04	a=62.76, b=70.23, c=128.0	a=62.85, b=70.23, c=128.0	a=62.80, b=70.26, c=128.2	a=62.79, b=70.14, c=128.3	a=62.88, b=70.24, c=128.5
R_{merge}[a,b]	0.225 (1.90)	0.061 (1.11)	0.10 (1.19)	0.073 (1.18)	0.085 (1.15)	0.091 (1.23)	0.081 (1.26)
Average $I/\sigma_{(I)}$[a,b]	8.4 (1.3)	21.2 (2.6)	15.2 (2.3)	18.3 (2.3)	13.9 (2.3)	14.3 (2.2)	17.7 (2.2)
$CC_{1/2}$ (%)[a,b,c]	0.995 (0.428)	99.9 (82.4)	99.9 (67.7)	99.9 (64.7)	99.9 (69.2)	99.9 (62.1)	99.9 (66.3)
Completeness (%)[a,b]	100.0 (100.0)	100.0 (100.0)	100.0 (100.0)	99.9 (99.9)	100.0 (99.9)	100.0 (100.0)	100.0 (100.0)
Redundancy[a,b]	11.1 (10.6)	12.4 (12.8)	12.2 (12.4)	12.4 (12.2)	12.2 (12.5)	12.1 (11.8)	12.4 (12.6)
Refinement							
Number of protein/solvent /ligand atoms	1968/363/24	1817/133/21	4093/718/47	4056/701/54	4221/762/52	4082/691/50	4026/670/46
R_{work}/R_{free} (%)	18.70/22.69	20.03/22.96	14.05/17.97	14.32/17.14	14.48/16.42	14.44/17.09	15.11/17.84
Unique reflections used in refinement	31950	24916	91195	111894	156936	112006	101399
R.m.s. deviations from ideal values bond lengths (Å) / bond angles (°)	0.005/0.94	0.004/0.87	0.008/1.11	0.010/1.26	0.006/1.12	0.008/1.17	0.008/1.12
Average protein/solvent /ligand B-factor ($Å^2$)	19.94/36.44/ 33.87	53.92/54.29/ 80.51	20.17/35.41/ 30.98	20.62/34.20/ 27.96	17.99/32.30/ 30.64	19.66/34.21/ 28.58	22.27/35.94/ 26.68
Ramachandran favored (%)	98.20	97.18	98.67	98.67	98.89	98.67	98.87
Ramachandran allowed (%)	1.80	2.82	1.33	1.33	1.11	1.33	1.13
Ramachandran outliers (%)	0	0	0	0	0	0	0

[a] Number in parentheses is for the highest resolution shell

[b] As reported by Aimless version 0.5.32.

[c] $CC_{1/2}$ = Pearson's intradataset correlation coefficient, as described by Karplus and Diederichs.[2]

X-ray diffraction data was collected at the DESY Petra-III P11 beamline[3,4] (derivative 3.2d) or the Swiss Light Source (SLS) PXII - X10SA beamline, Paul Scherrer Institut, Villigen, Switzerland (all other derivatives). The data was indexed and integrated using iMosflm and scaled and merged using Aimless.[5] Phasing was done by molecular replacement using Phaser and 5HF3 as a starting model.[6,7] This was followed by iterative rounds of refinement and manual model building using Phenix.Refine and COOT respectively.[8] Model validation was performed using MolProbity prior to PDB submission.

Isothermal titration calorimetry (ITC) data

Table S2. Summary of all ITC data.

	1st duplicate measurement						*2nd duplicate measurement*					
	K_d	±	*N*	*ΔH*	*TΔS*	*ΔG*	K_d	±	*N*	*ΔH*	*TΔS*	*ΔG*
3.2a	5.4	0.4	1.07	-2.5	5.0	-7.5	4.2	0.5	1.03	-2.5	5.1	-7.6
3.2b	5.6	0.5	1.25	-2.5	5.0	-7.5	6.1	1.0	1.23	-2.6	4.8	-7.4
3.2c	3.3	0.7	1.17	-2.4	5.4	-7.8	4.7	1.0	1.18	-2.6	5.0	-7.6
3.2d	3.0	0.6	1.15	-1.7	6.1	-7.8	5.0	1.1	1.38	-2.1	5.4	-7.5
3.2e	2.2	0.7	1.16	-1.5	6.6	-8.1	2.4	1.6	0.86	-1.8	6.2	-8.0
3.2f	3.4	0.6	0.97	-1.9	5.8	-7.7	5.7	3.2	1.01	-2.0	5.4	-7.4
	K_d	±	*N*	*ΔH*	*TΔS*	*ΔG*	K_d	±	*N*	*ΔH*	*TΔS*	*ΔG*
4.2a	8.9	0.7	1.22	-4.0	3.1	-7.1	11.0	0.9	1.01	-5.4	1.6	-7.0
4.2b	9.4	2.0	0.99	-3.9	3.2	-7.1	9.8	2.1	0.97	-3.8	3.3	-7.1
4.2c-I	2.7	0.3	0.94	-5.8	2.1	-7.9	3.6	0.7	0.8	-6.4	1.3	-7.7
4.2c-II	9.0	0.5	1.09	-4.7	2.5	-7.2	8.3	5.8	1.13	-4.6	2.6	-7.2
4.2d-I	6.4	0.6	0.75	-5.7	1.6	-7.3	7.6	0.7	0.75	-6.1	1.1	-7.2
4.2d-II	20.6	2.4	0.97	-2.9	3.8	-6.7	19.0	2.5	0.96	-3.4	3.3	-6.7
4.2e-I	3.6	0.6	1.13	-3.1	4.6	-7.7	5.0	0.6	1.09	-3.2	4.3	-7.5
4.2e-II	12.7	0.9	1.13	-3.5	3.5	-7.0	13.6	2.5	1.17	-3.6	3.3	-6.9
4.2f-I	4.7	0.6	0.86	-4.7	2.8	-7.5	6.3	0.9	0.85	-5.0	2.4	-7.5
4.2f-II	16.5	2.0	0.97	-5.0	1.8	-6.8	14.8	2.4	0.86	-6.1	0.8	-6.9
4.2g	6.3	1.1	1.15	-3.9	3.5	-7.4	9.9	2.6	1.02	-4.5	2.6	-7.1

Figure S16. ITC data for tau inhibitor 3.2a.

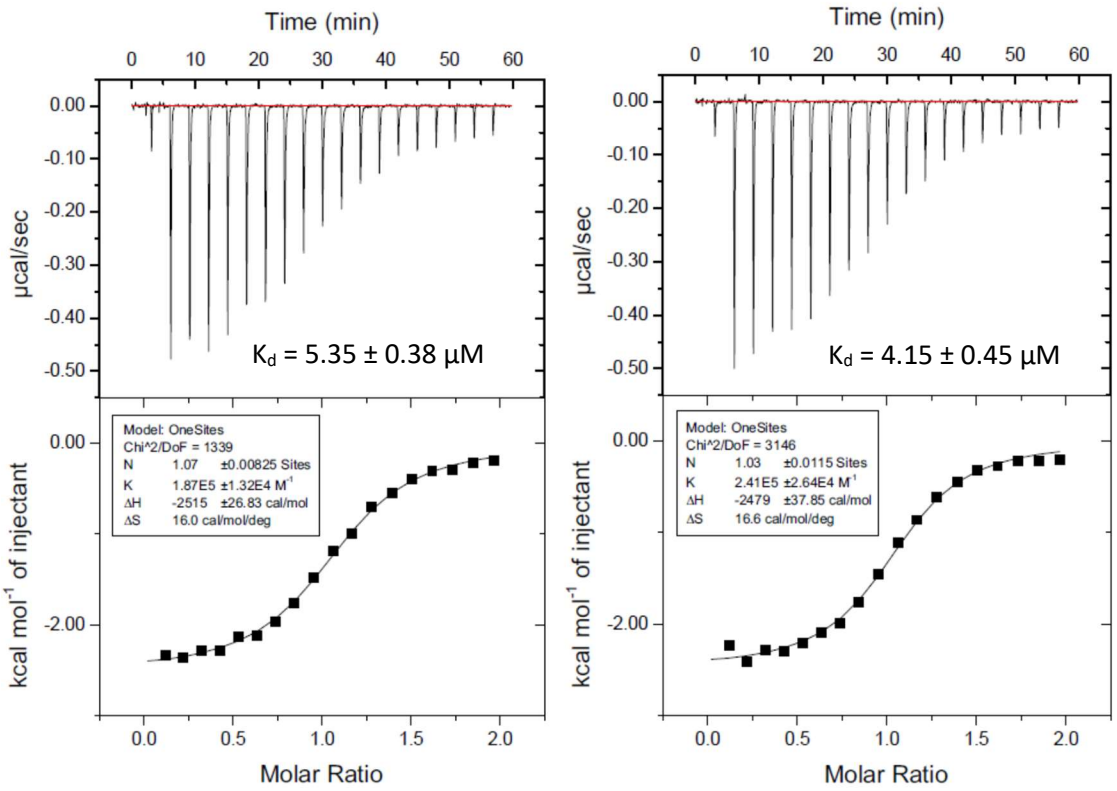

Figure S17. ITC data for tau inhibitor 3.2b.

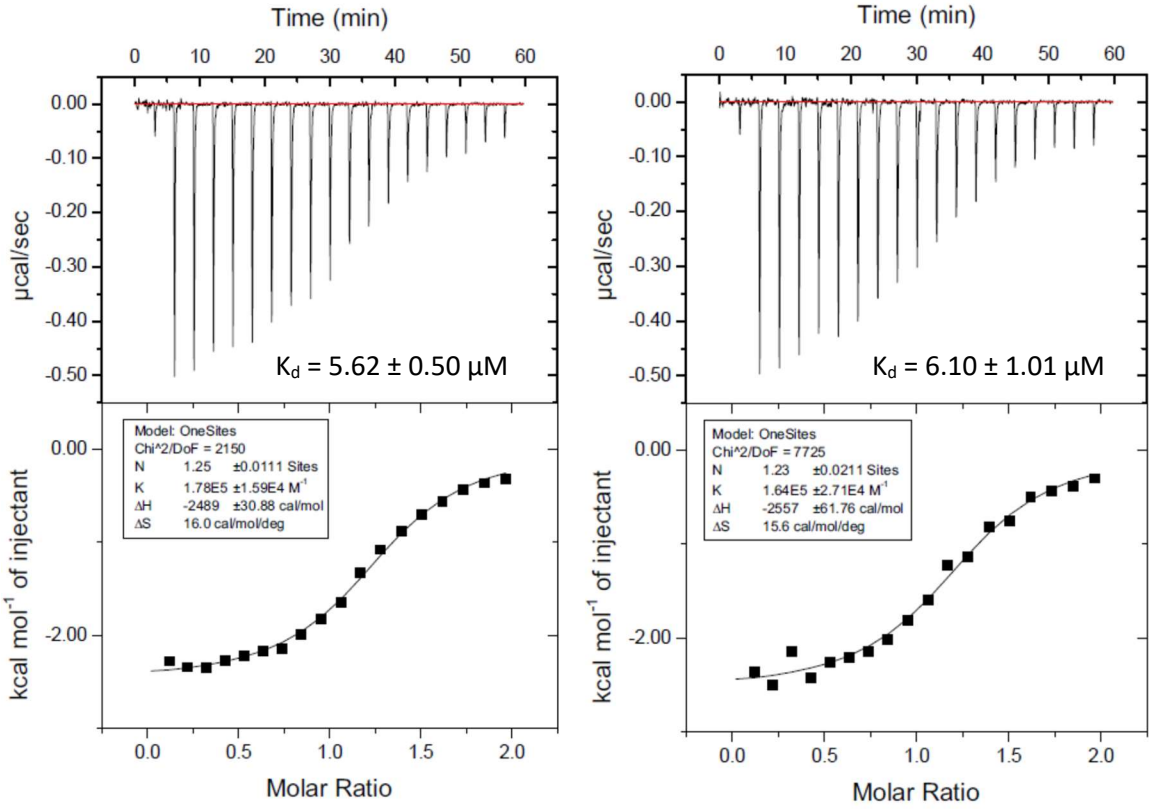

Figure S18. ITC data for tau inhibitor 3.2c.

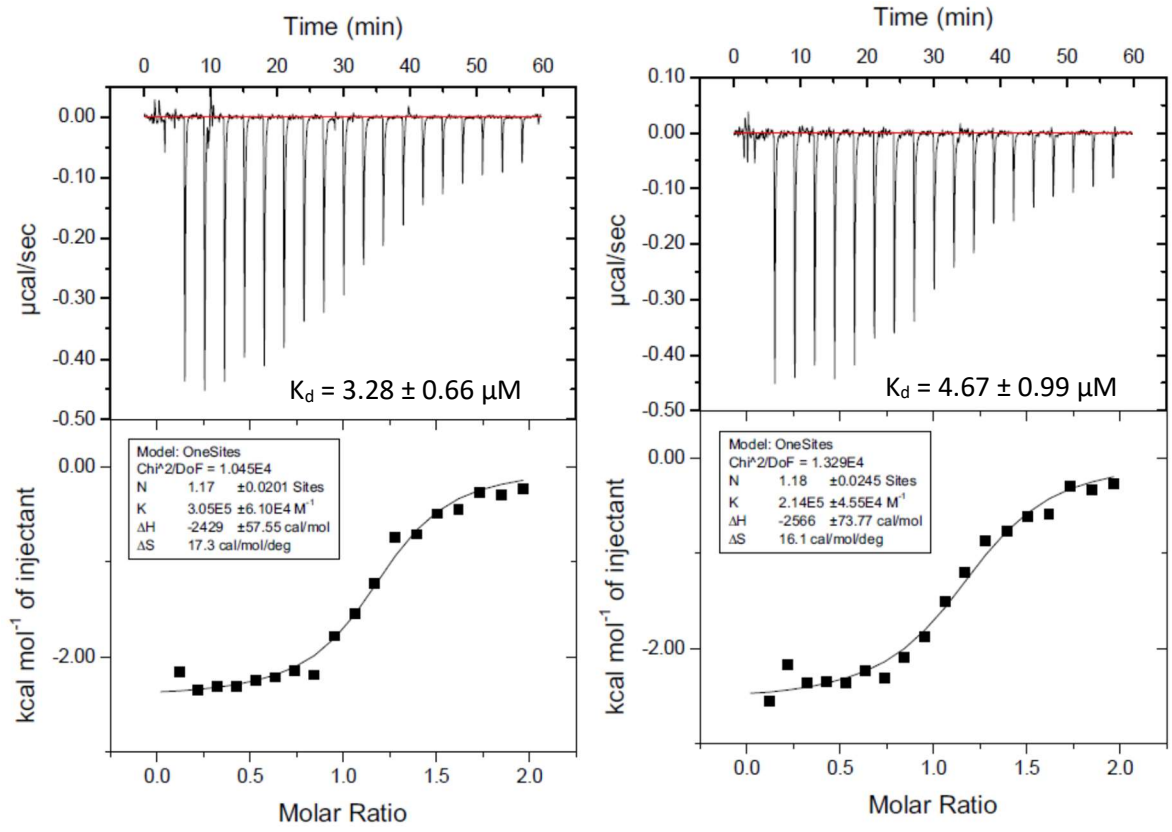

Figure S19. ITC data for tau inhibitor 3.2d.

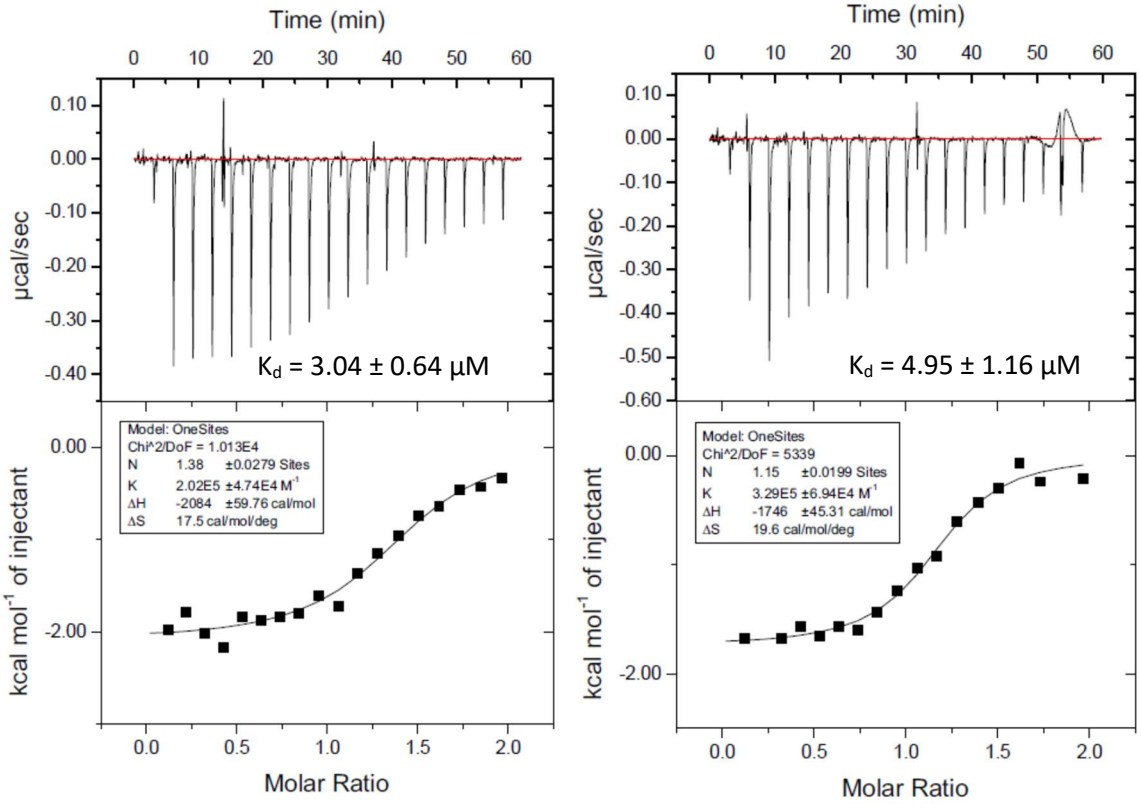

Figure S20. ITC data for Tau inhibitor 3.2e.

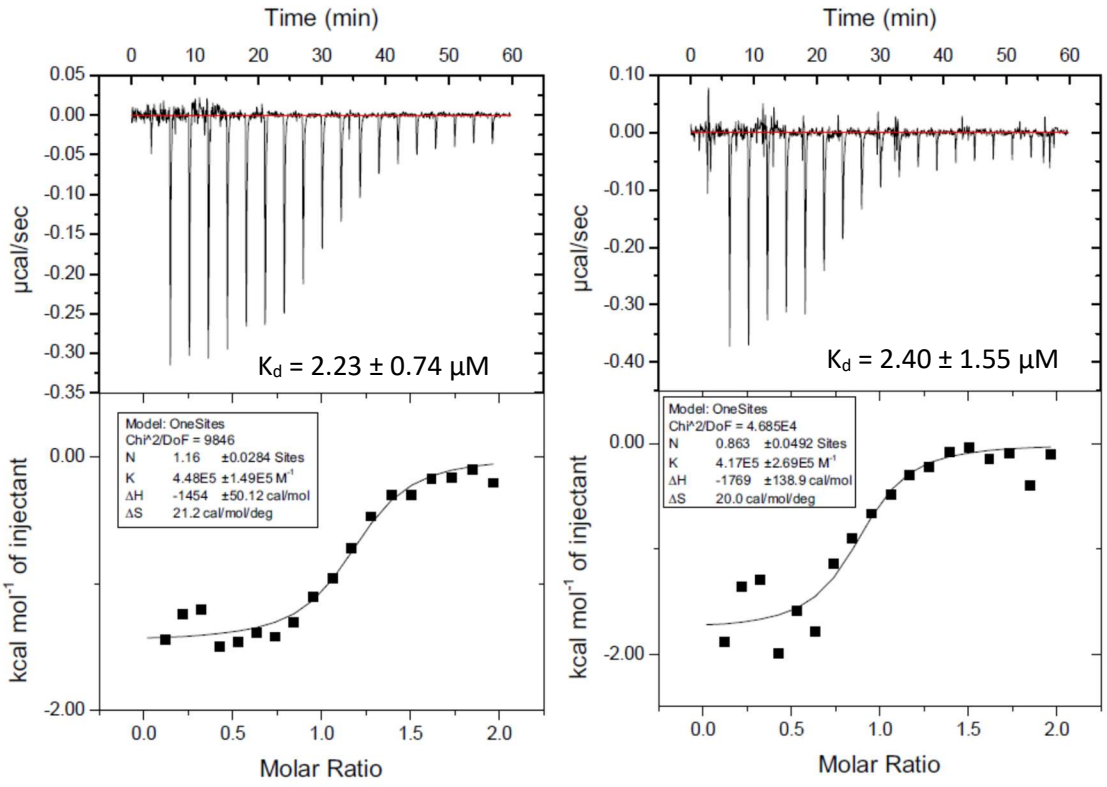

Figure S21. ITC data for tau inhibitor 3.2f.

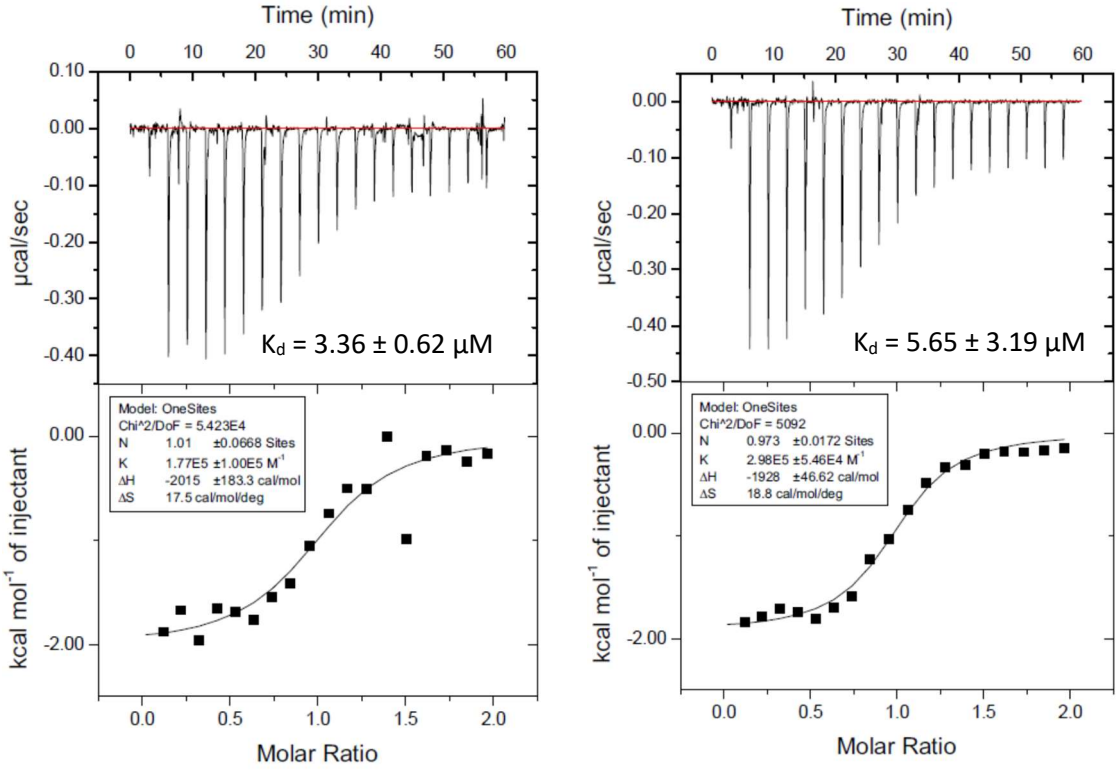

Figure S22. ITC data for tau inhibitor 4.2a.

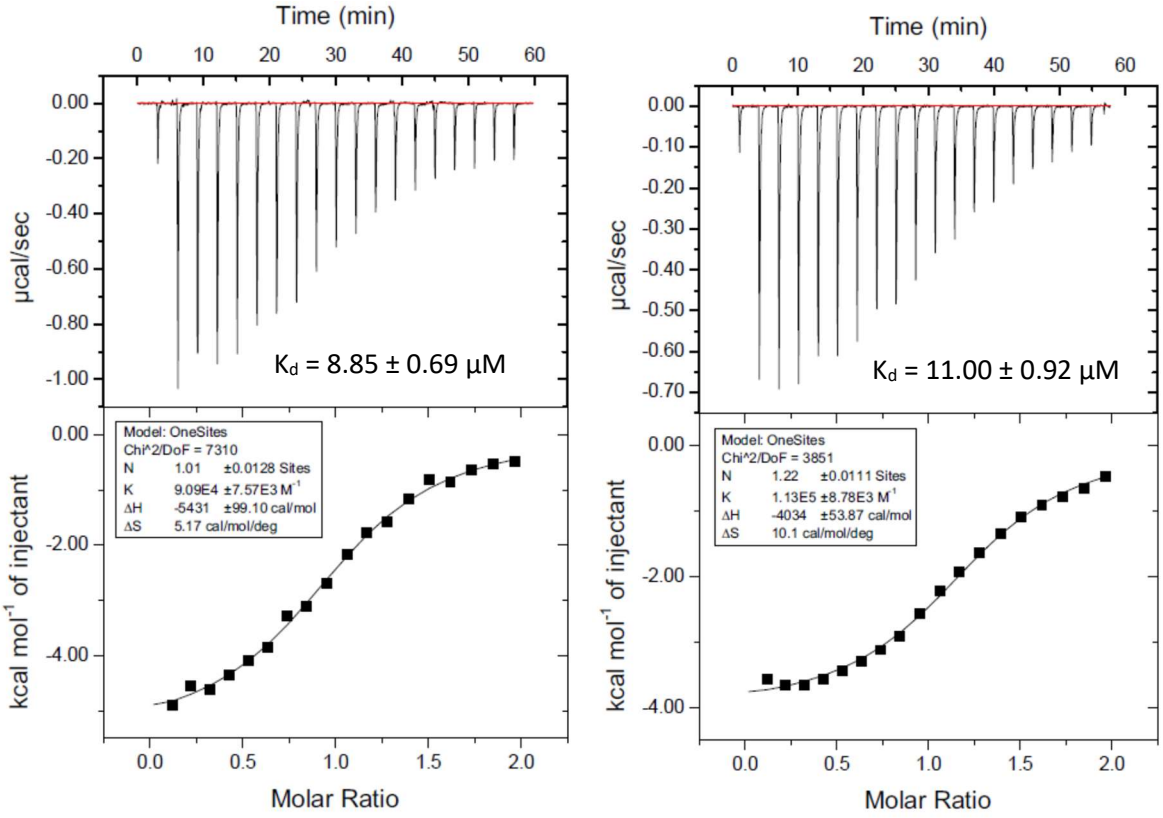

Figure S23. ITC data for tau inhibitor 4.2b.

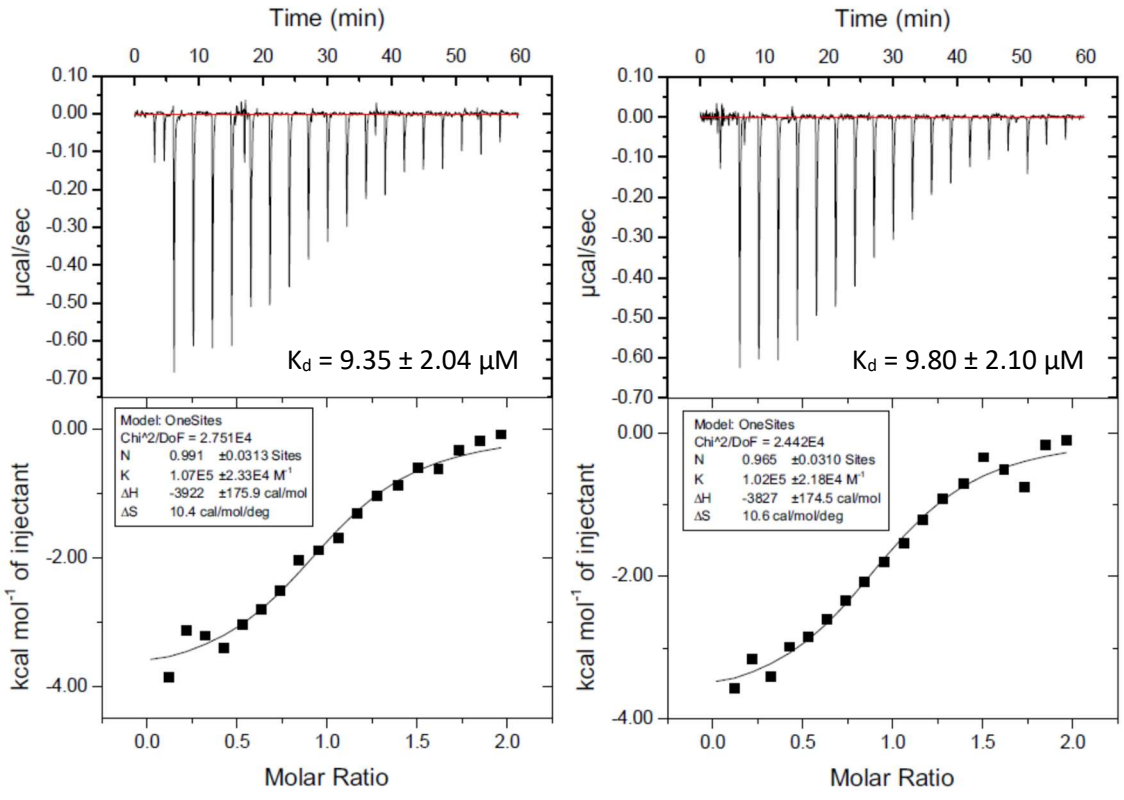

Figure S24. ITC data for tau inhibitor 4.2c-I.

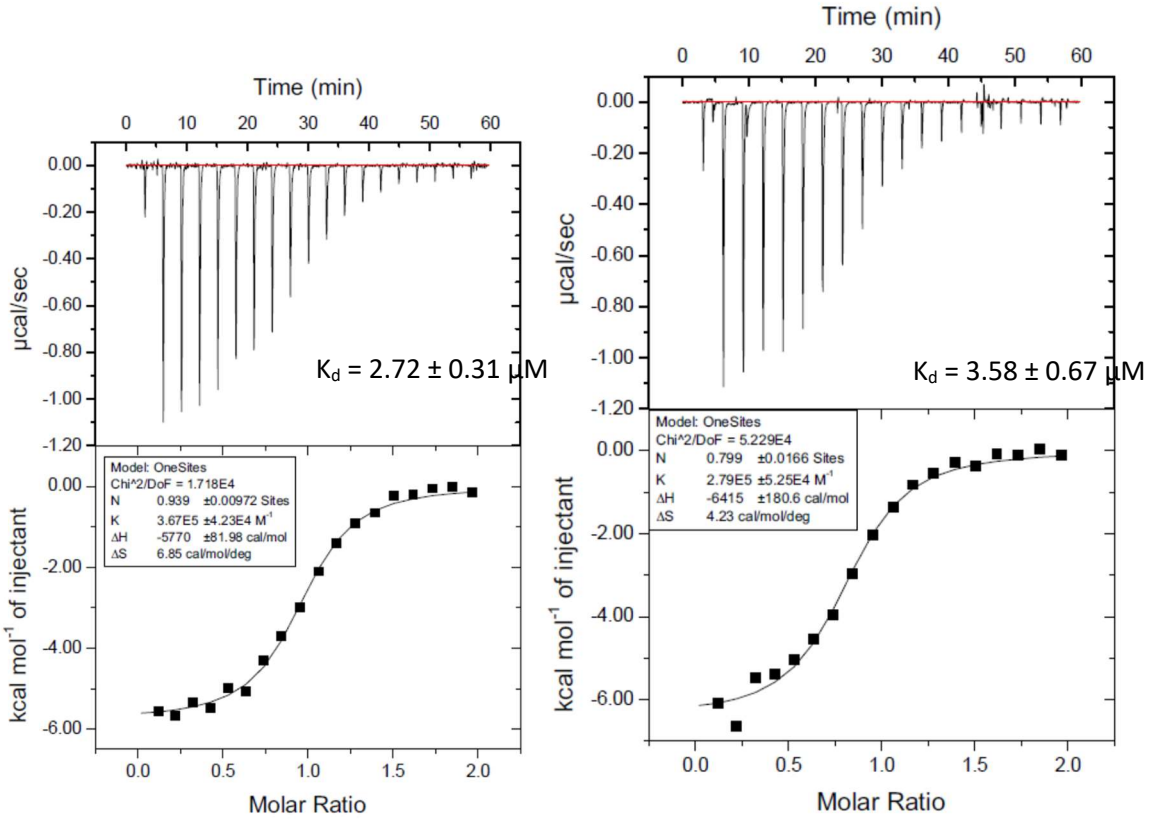

Figure S25. ITC data for tau inhibitor 4.2c-II.

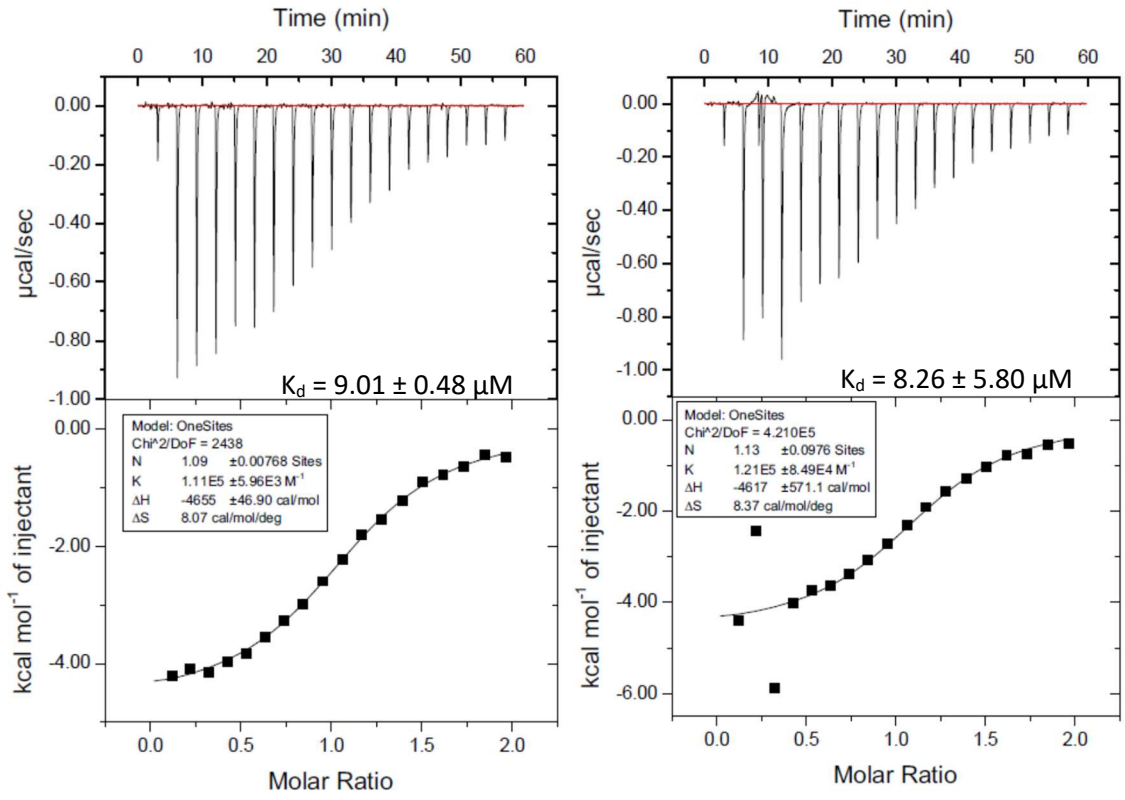

Figure S26. ITC data for tau inhibitor 4.2d-I.

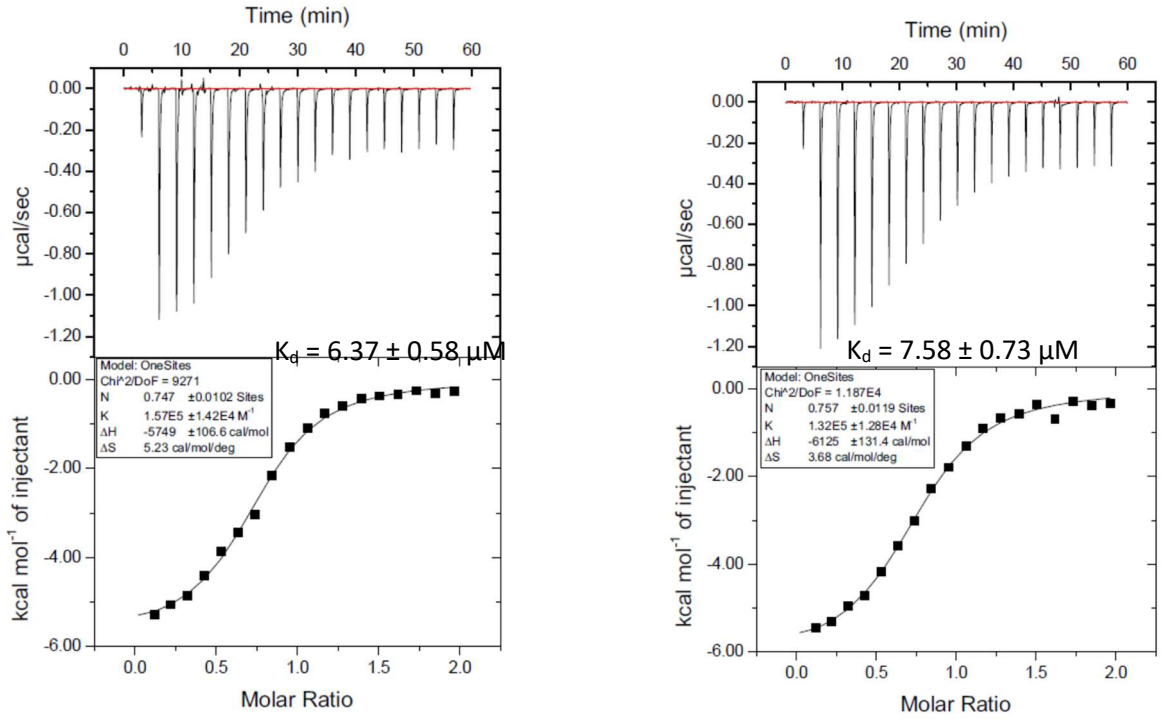

Figure S27. ITC data for tau inhibitor 4.2d-II.

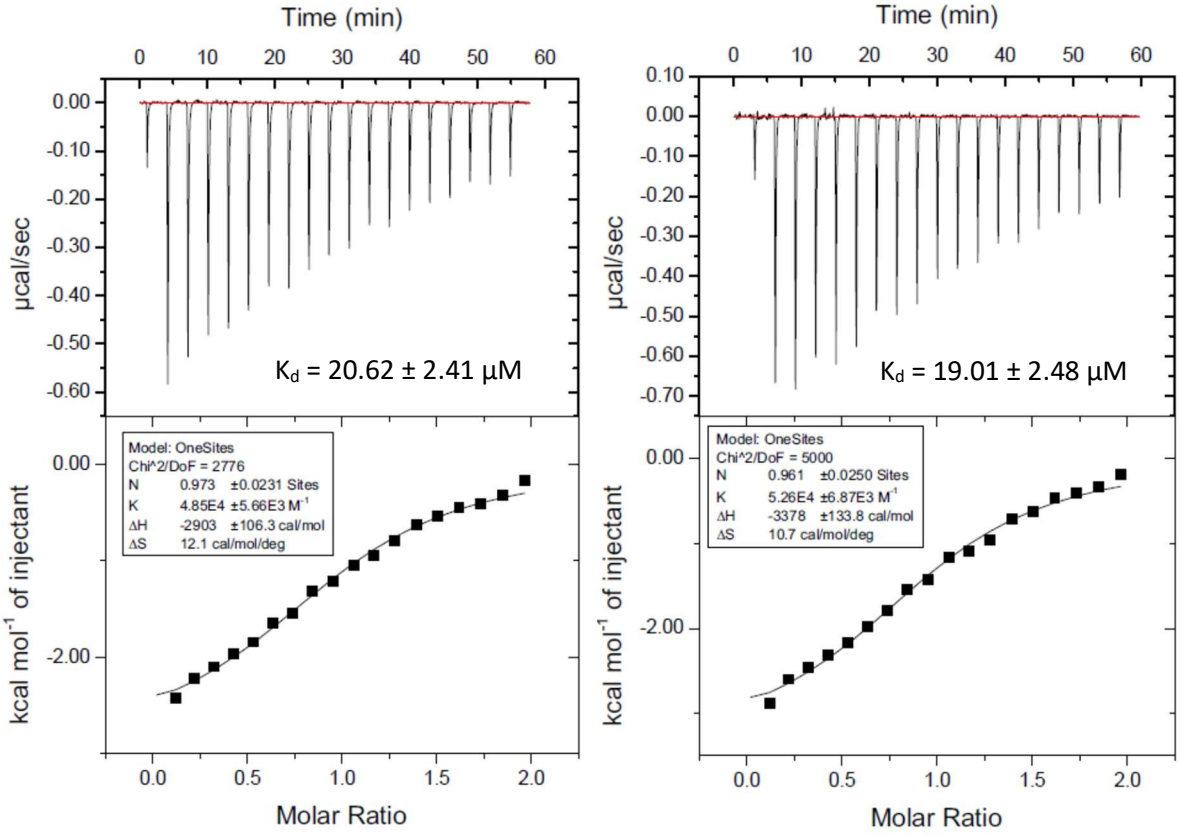

Figure S28. ITC data for tau inhibitor 4.2e-I.

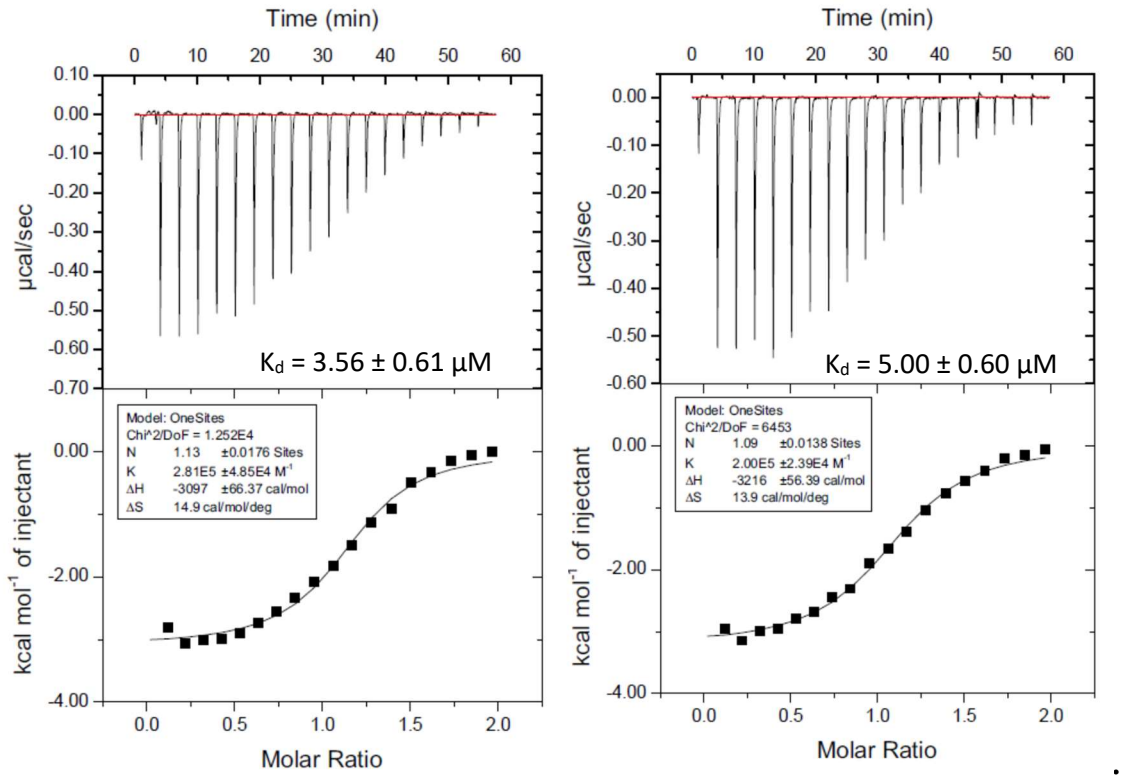

Figure S29. ITC data for tau inhibitor 4.2e-II.

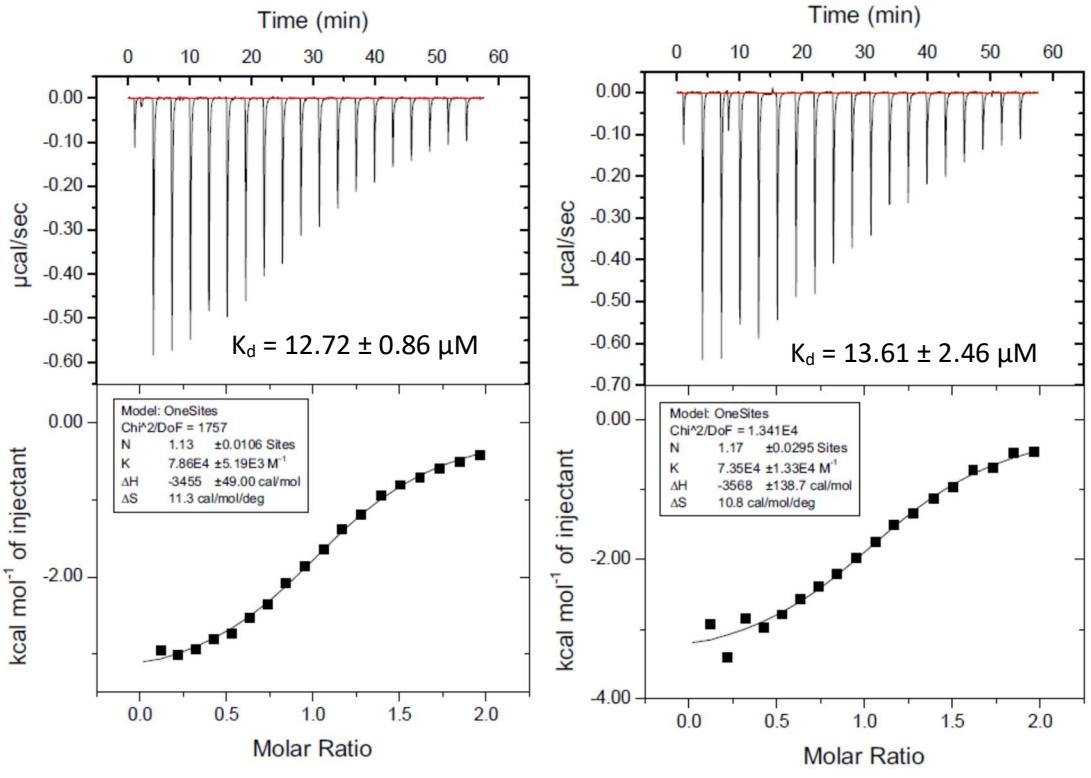

Figure S30. ITC data for tau inhibitor 4.2f-I.

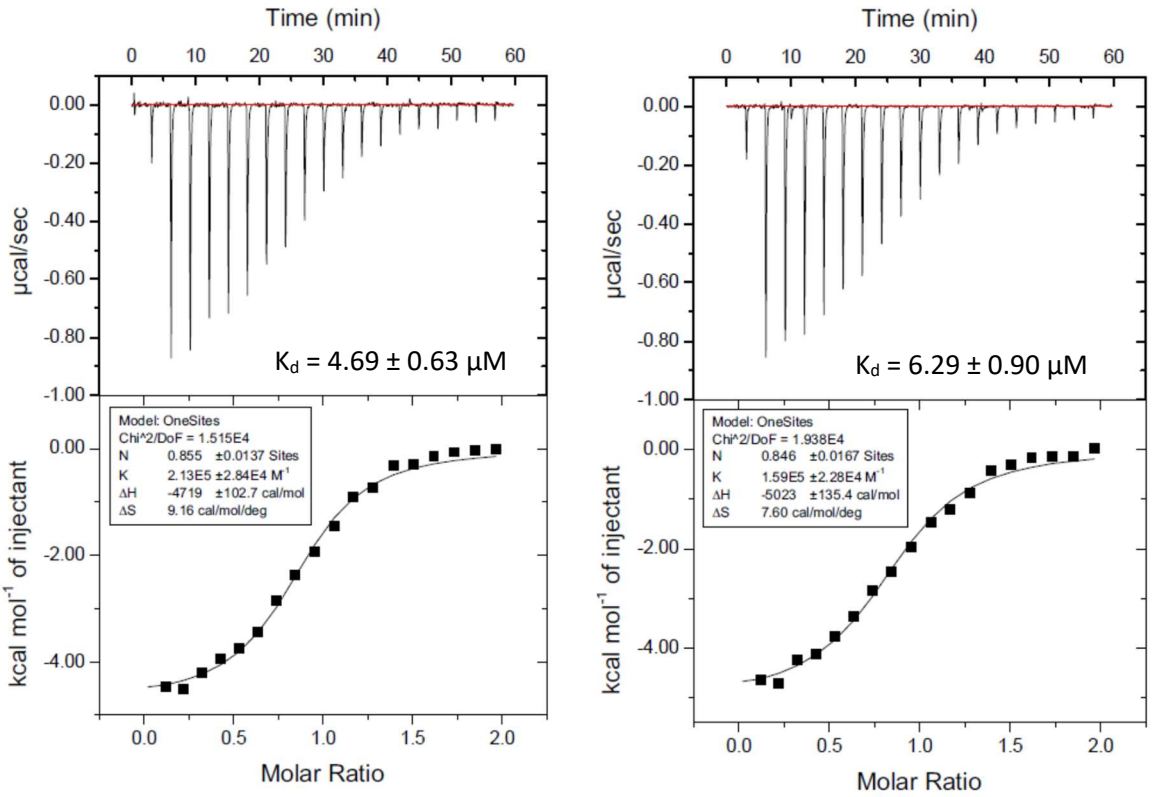

Figure S31. ITC data for tau inhibitor 4.2f-II.

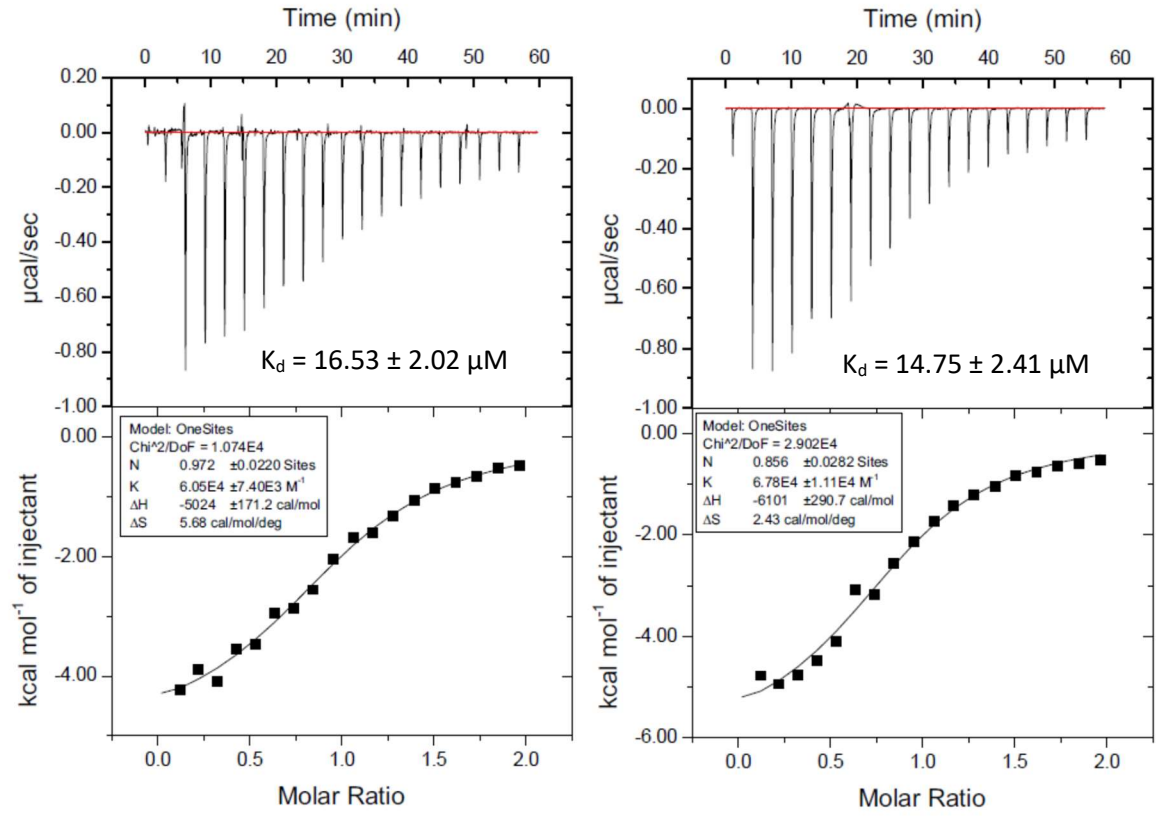

Figure S32. ITC data for tau inhibitor 4.2g.

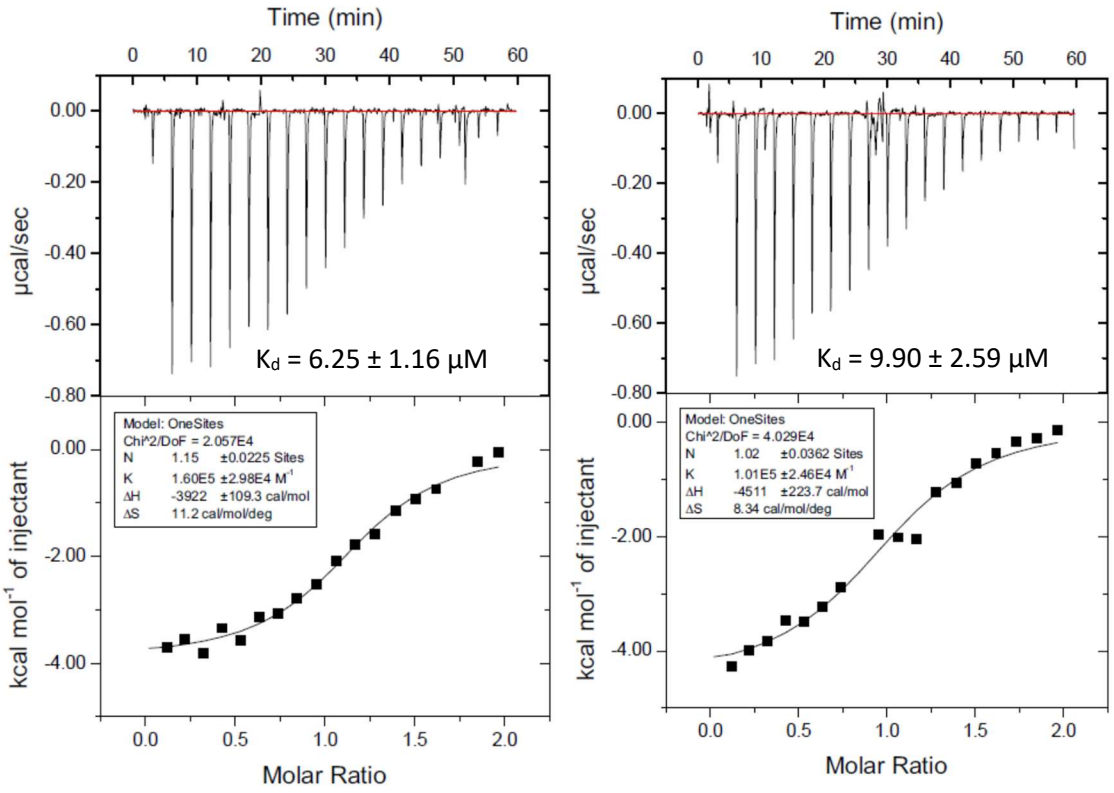

Fluorescence polarization data

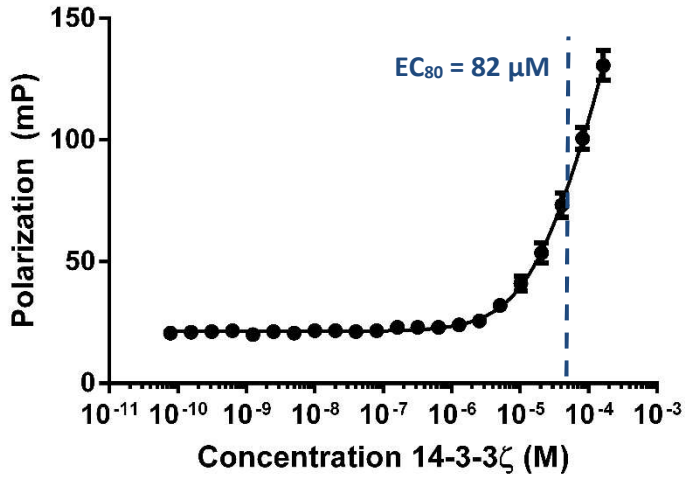

Figure S33. Direct FP assay with a 2-fold dilution series of 14-3-3ζ (from 164 µM) to 10 nM FITC-labeled Slingshot peptide (FITC-LTRSS-pS-SDSIH). The obtained EC_{80} value was used for the 14-3-3 concentration in the Competitive FP assays below.

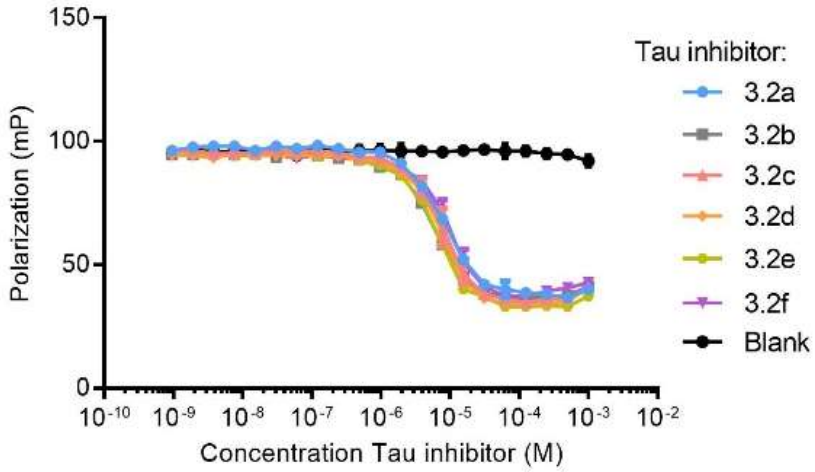

Figure S34. Competitive FP assay with 100 nM FAM-labeled diphosphorylated Tau peptide ((5,6-FAM)-RTP-pS-LPTG(GGS)3GSKCG-pS-LGNIHHK), 10 µM 14-3-3ζ and a 2-fold dilution series of Tau inhibitors **3.2a-f** (from 1 mM). Mean of two experiments.

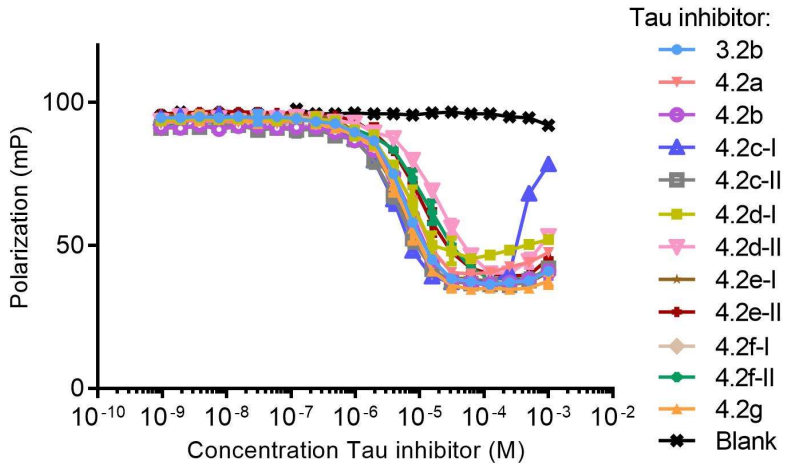

Figure S35: Competitive FP assay with 100 nM FAM-labeled diphosphorylated Tau peptide ((5,6-FAM)-RTP-pS-LPTG(GGS)3GSKCG-pS-LGNIHHK), 10 µM 14-3-3ζ and a 2-fold dilution series of Tau inhibitors **4.2a-g** & **3.2b** as reference compound (from 1 mM). Mean of two experiments.

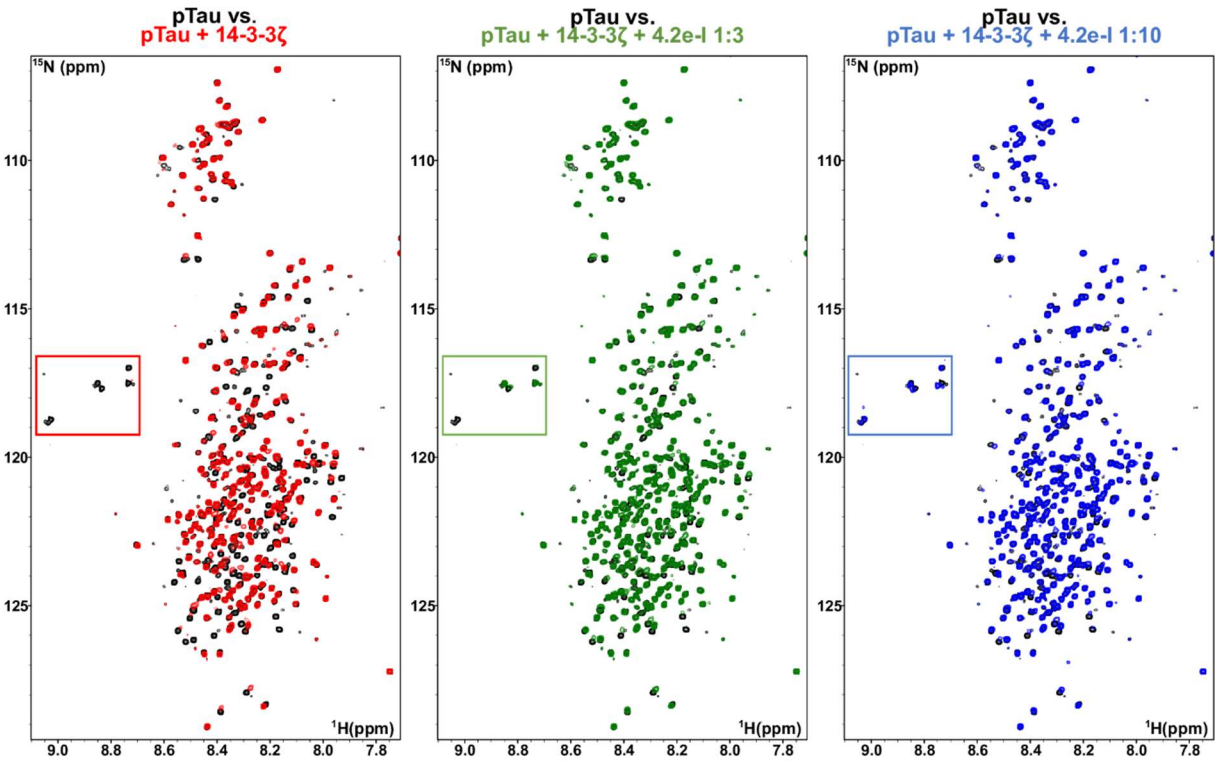

Figure S36. Superimposed ^{15}N-^{1}H HSQC spectra of 60 µM ^{15}N labelled pTau (black spectrum) and 60 µM ^{15}N labelled pTau + 14-3-3ζ 120 µM (overlayed red spectrum); 60 µM ^{15}N labelled pTau + 14-3-3ζ 120 µM + **4.2e-I** 360 µM (overlayed green spectrum) and 60 µM ^{15}N labelled pTau + 14-3-3ζ 120 µM + **4.2e-I** 1200 µM (overlayed blue spectrum). The boxed regions in the spectra are enlarged in Figure 5 of the manuscript.

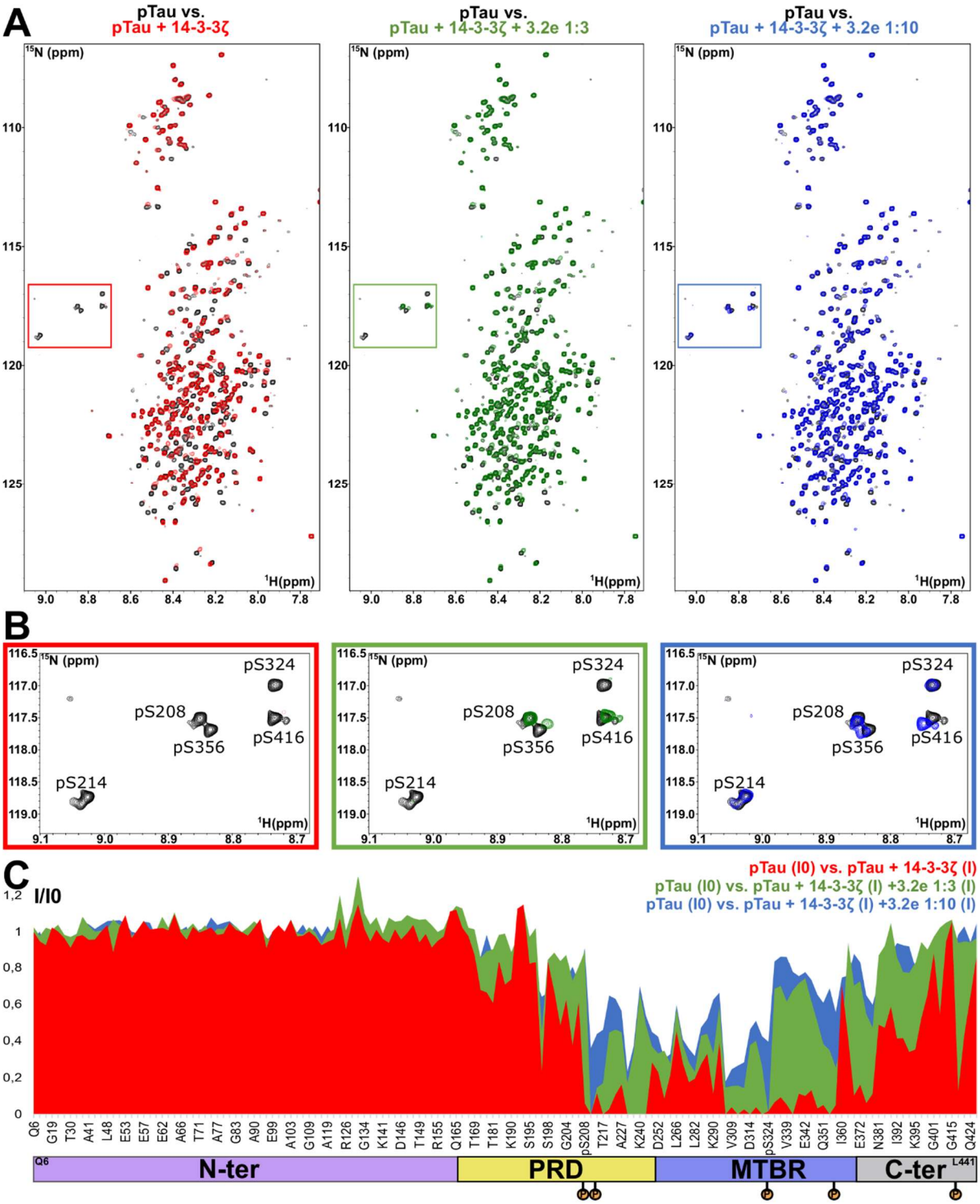

Figure S37. 3.2e inhibits the binding of full-length PKA-phosphorylated Tau (pTau) to 14-3-3ζ in a concentration-dependent manner. A) Superimposed ^{15}N-^{1}H HSQC spectra of 60 µM ^{15}N labelled pTau (black spectrum) and 60 µM ^{15}N labelled pTau + 14-3-3ζ 120 µM (overlayed red

spectrum); 60 μM ^{15}N labelled pTau + 14-3-3ζ 120 μM + **3.2e** 360 μM (overlayed green spectrum) and 60 μM ^{15}N labelled pTau + 14-3-3ζ 120 μM + **3.2e** 1200 μM (overlayed blue spectrum). The boxed regions are enlarged in B), showing the intensity recovery of the correlation peaks correspondent to the amide groups of the PKA-phosphorylated Serines after the addition of **3.2e**. C) Plot of the ratios of the bound (I)/free (I0) ^{1}H-^{15}N correlation peak intensities of full length pTau 60 μM (y axis) versus the amino acid sequence (x axis) in the presence of 14-3-3ζ 120 μM (red plot); 14-3-3ζ 120 μM + **3.2e** 360 μM (green plot) and 14-3-3ζ 120 μM + **3.2e** 1200 μM (blue plot). A total of 155 correlation peak intensities are shown. The x axis is not proportional. The domains of full-length pTau (N-ter for N-terminal; PRD for Proline-Rich Domain; MTBR for Microtubule Binding Region; C-ter for C-terminal) and the phosphorylation sites (S208, S214, S324, S356 and S416) are identified bellow the x axis.

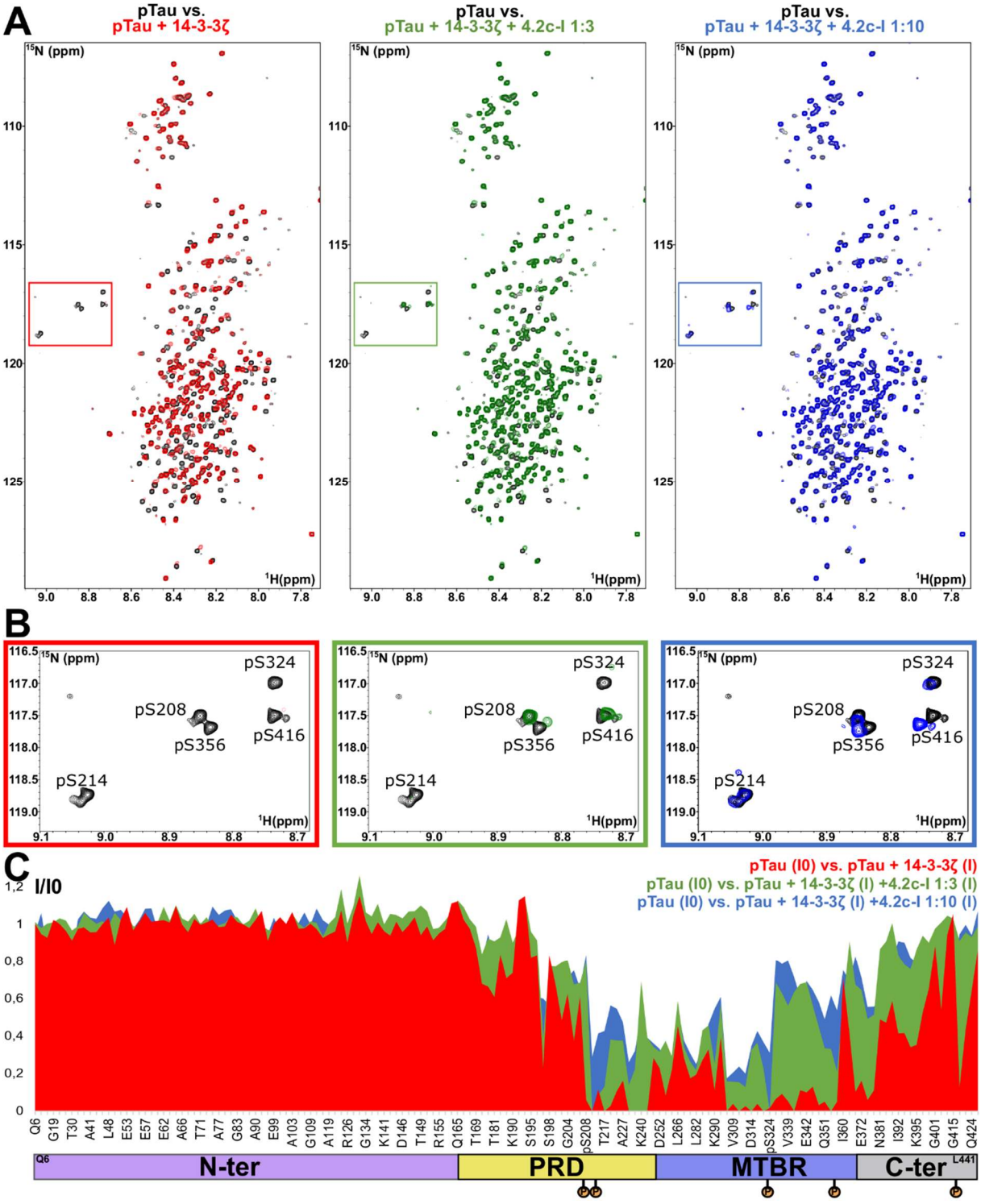

Figure S38. 4.2c-I inhibits the binding of full-length PKA-phosphorylated Tau (pTau) to 14-3-3ζ in a concentration-dependent manner. A) Superimposed ^{15}N-^{1}H HSQC spectra of 60 μM ^{15}N labelled pTau (black spectrum) and 60 μM ^{15}N labelled pTau + 14-3-3ζ 120 μM (overlayed red spectrum); 60 μM ^{15}N labelled pTau + 14-3-3ζ 120 μM + **4.2c-I** 360 μM (overlayed green spectrum) and 60 μM ^{15}N labelled pTau + 14-3-3ζ 120 μM + **4.2c-I** 1200 μM (overlayed blue

spectrum). The boxed regions are enlarged in B), showing the intensity recovery of the correlation peaks correspondent to the amide groups of the PKA-phosphorylated Serines after the addition of **4.2c-I**. C) Plot of the ratios of the bound (I)/free (I0) ^{1}H-^{15}N correlation peak intensities of full length pTau 60 μM (y axis) versus the amino acid sequence (x axis) in the presence of 14-3-3ζ 120 μM (red plot); 14-3-3ζ 120 μM + **4.2c-I** 360 μM (green plot) and 14-3-3ζ 120 μM + **4.2c-I** 1200 μM (blue plot). A total of 155 correlation peak intensities are shown. The x axis is not proportional. The domains of full-length pTau (N-ter for N-terminal; PRD for Proline-Rich Domain; MTBR for Microtubule Binding Region; C-ter for C-terminal) and the phosphorylation sites (S208, S214, S324, S356 and S416) are identified bellow the x axis.

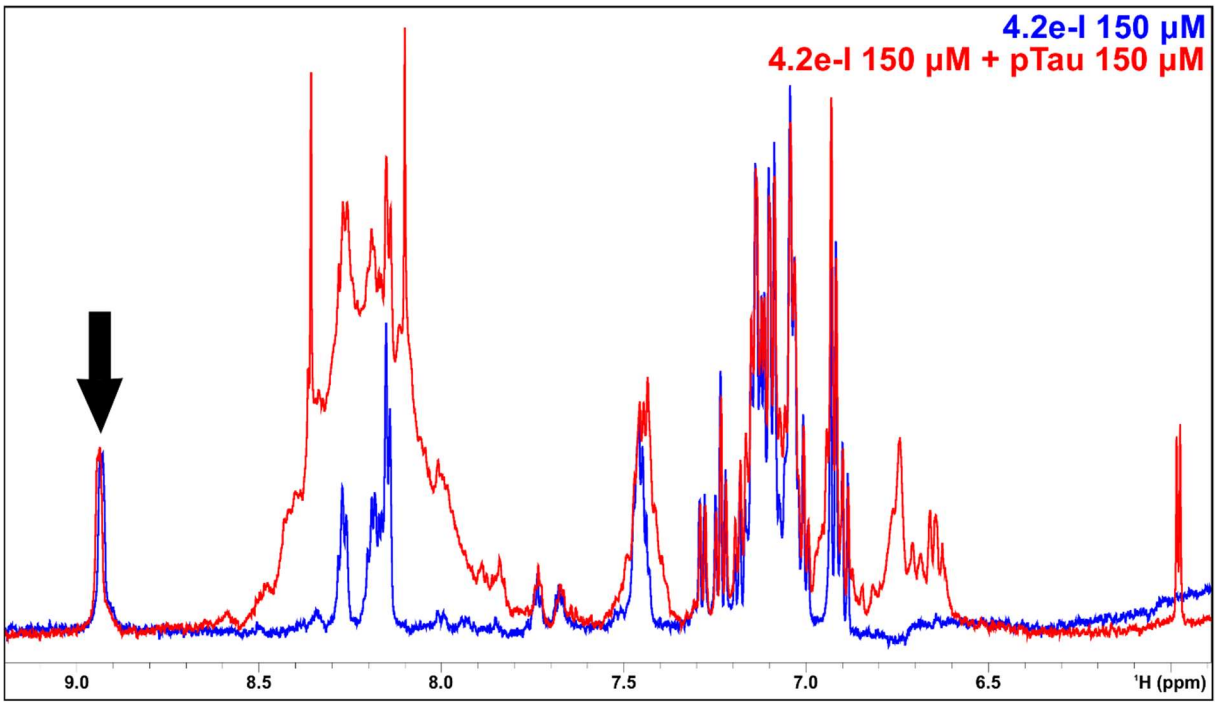

Figure S39 - Section of overlayed 1H spectra of **4.2e-I** 150 µM alone (blue) and in the presence of pTau 150 µM (red). The black arrow points to a well-isolated resonance from **4.2e-I**, which is not affected in the presence of pTau.

Synthesis of 1-bromo-2-(2-methoxyethoxy)benzene and 1-bromo-3-(2-methoxyethoxy)benzene

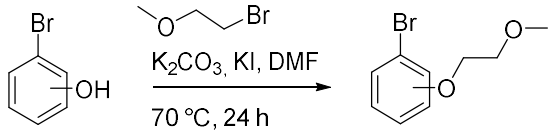

An oven dried 50 mL flask was charged with either 2- or 3-bromophenol (500 mg, 2.9 mmol), and DMF (8 mL). Next, K_2CO_3 (600 mg, 4.3 mmol), a small amount of KI and 1-bromo-2-methoxyethane (603 mg, 4.3 mmol) were added. The reaction mixture was then stirred at 70 °C for 24 h. The resulting mixture was extracted with EtOAc (3 x 30 mL) and the combined organic layers were washed with brine, dried over Na_2SO_4, filtered and concentrated *in vacuo*. The product was purified by silica gel column chromatography, eluting with heptane/EtOAc 90:10 v/v to yield either 1-bromo-2-(2-methoxyethoxy)benzene (617 mg, 2.7 mmol, 93%) or 1-bromo-3-(2-methoxyethoxy)benzene (626 mg, 2.7 mmol, 93%), both as colorless oils.

1-bromo-2-(2-methoxyethoxy)benzene. Silica gel TLC R_f = 0.26 (heptane/EtOAc 90:10 v/v); GC-MS (ESI) *m/z* calc. for $C_9H_{11}BrO_2$: 229.99, most abundant peaks observed: 232, 230, 174, 172, R_t = 5.05 min; ^{1}H NMR (400 MHz, $CDCl_3$): δ (ppm) 7.54 (dd, *J* = 7.9, 1.6 Hz, 1H), 7.25 – 7.21 (m, 1H), 6.93 (dd, *J* = 8.3, 1.4 Hz, 1H), 6.84 (td, *J* = 7.6, 1.4 Hz, 1H), 4.17 (t, J = 4.8 Hz, 2H), 3.81 (t, J = 5.2 Hz, 2H), 3.49 (s, 3H); ^{13}C NMR (100 MHz, $CDCl_3$): δ 155.32, 133.39, 128.42, 122.18, 113.75, 112.46, 70.87, 68.96, 59.50.

1-bromo-3-(2-methoxyethoxy)benzene. Silica gel TLC R_f = 0.24 (Heptane/EtOAc 90:10 v/v); GC-MS (ESI) *m/z* calc. for $C_9H_{11}BrO_2$: 229.99, most abundant peaks observed: 232, 230, 174, 172, R_t = 5.04 min; ^{1}H NMR (400 MHz, $CDCl_3$): δ (ppm) 7.19 – 7.03 (m, 3H), 6.90 – 6.83 (m, 1H), 4.10 (t, J= 4.4 Hz, 2H), 3.74 (t, J =4.8 Hz, 2H), 3.45 (s, 3H); ^{13}C NMR (100 MHz, $CDCl_3$): δ 159.54, 13 0.51, 124.01, 122.74, 117.87, 113.67, 70.84, 67.52, 59.24.

Figure S40. ^{1}H NMR of *tert*-butyl (*S*)-2-benzoylpyrrolidine-1-carboxylate (2.2).

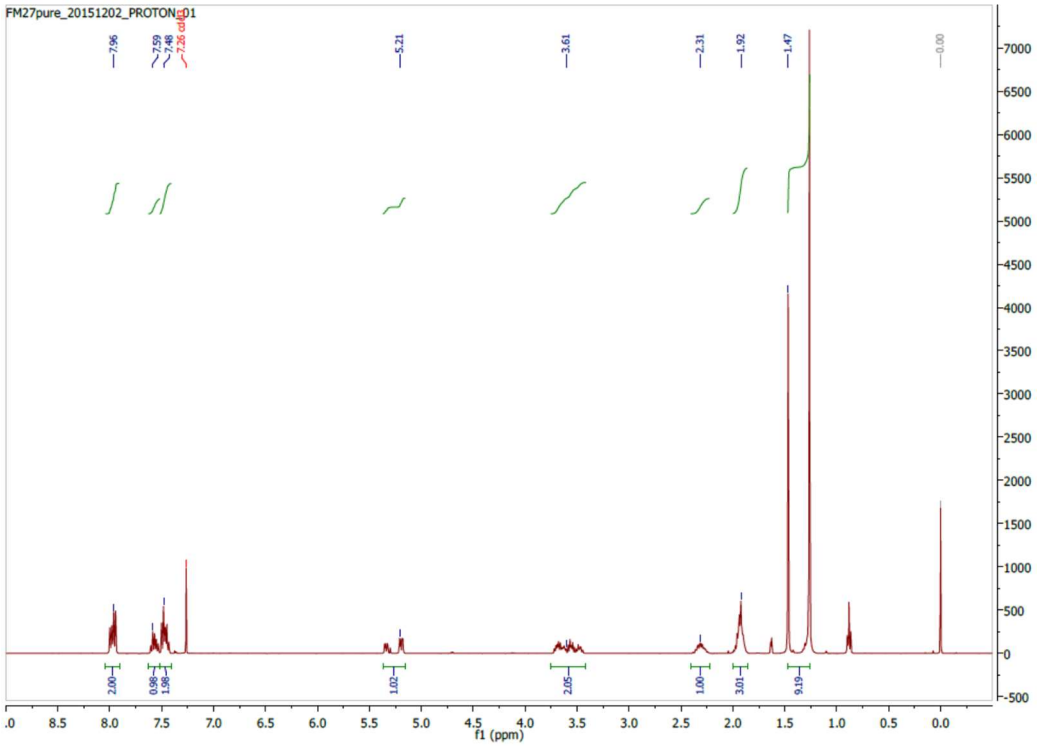

Figure S41. ^{13}C NMR of *tert*-butyl (*S*)-2-benzoylpyrrolidine-1-carboxylate (2.2).

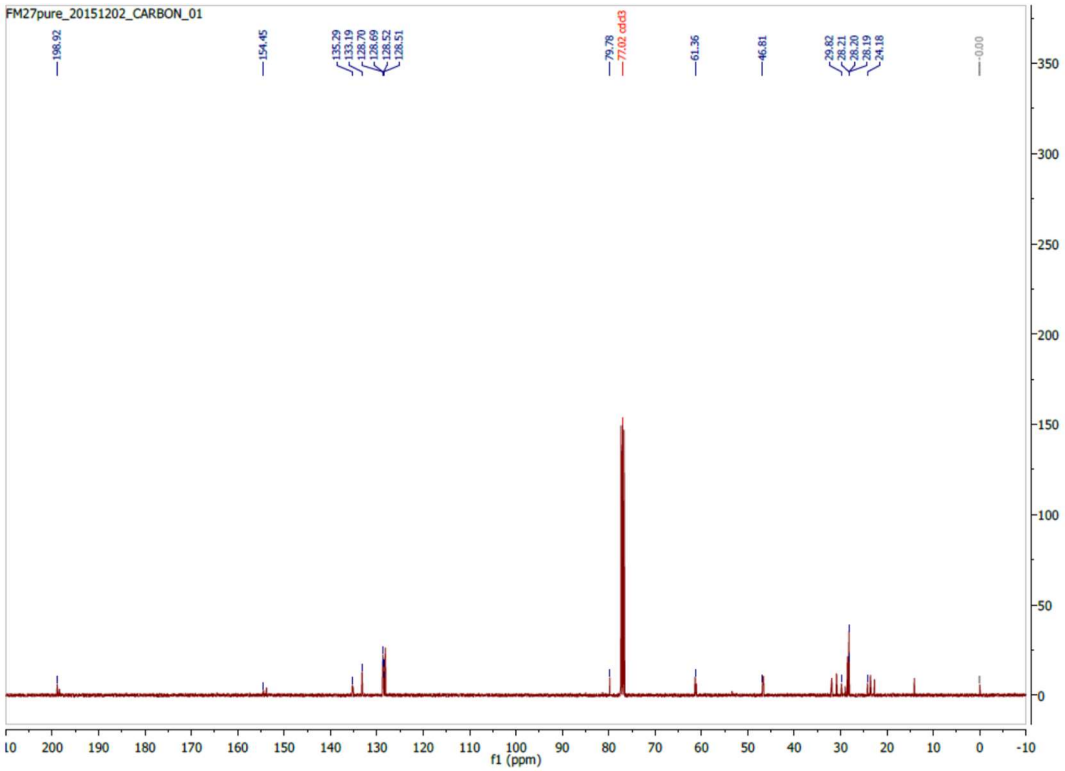

Figure S42. LC-MS of *tert*-butyl (*S*)-2-benzoylpyrrolidine-1-carboxylate (2.2).

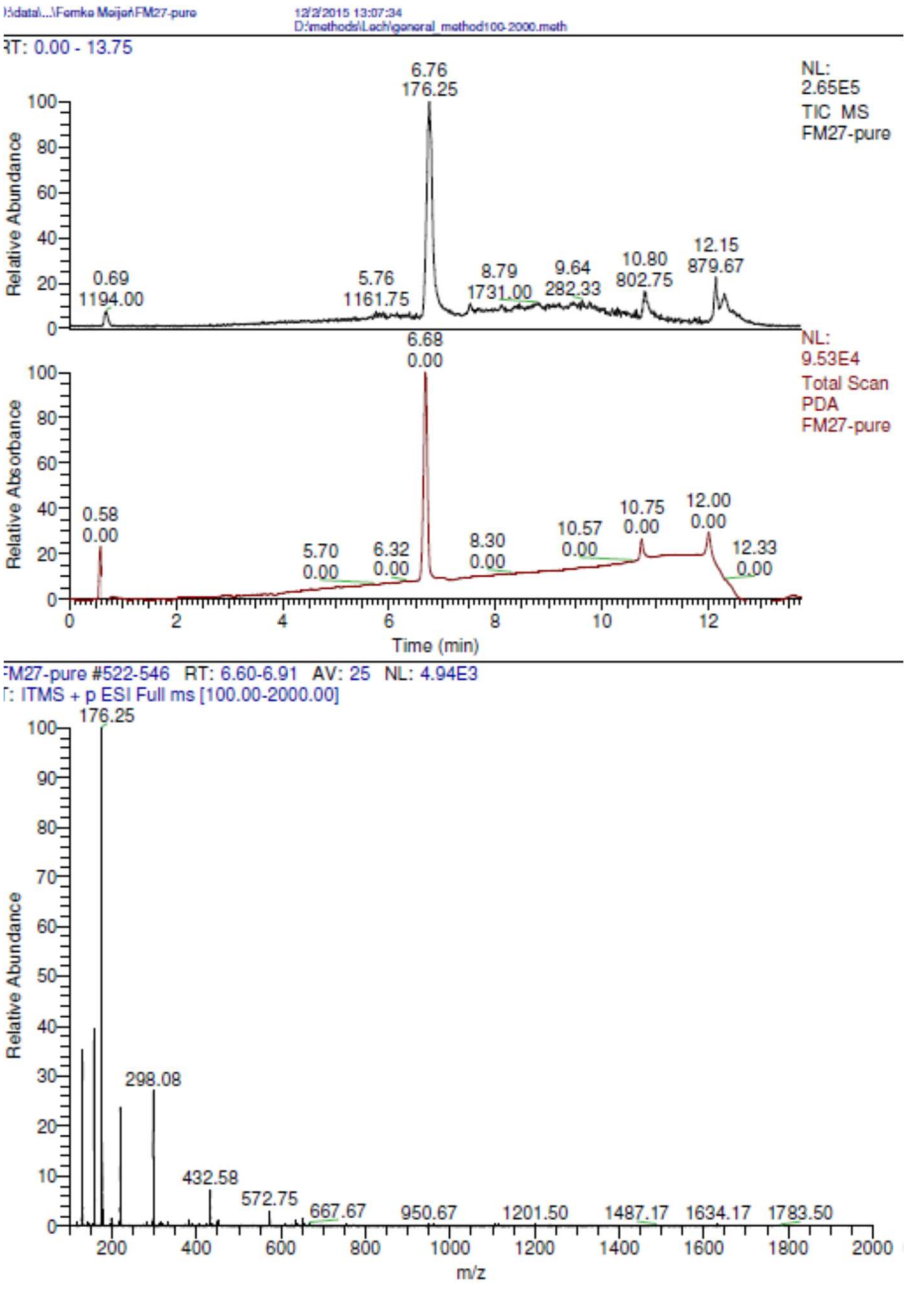

Figure S43. ^{1}H NMR of (*S*)-phenyl(pyrrolidin-2-yl)methanone (2.3).

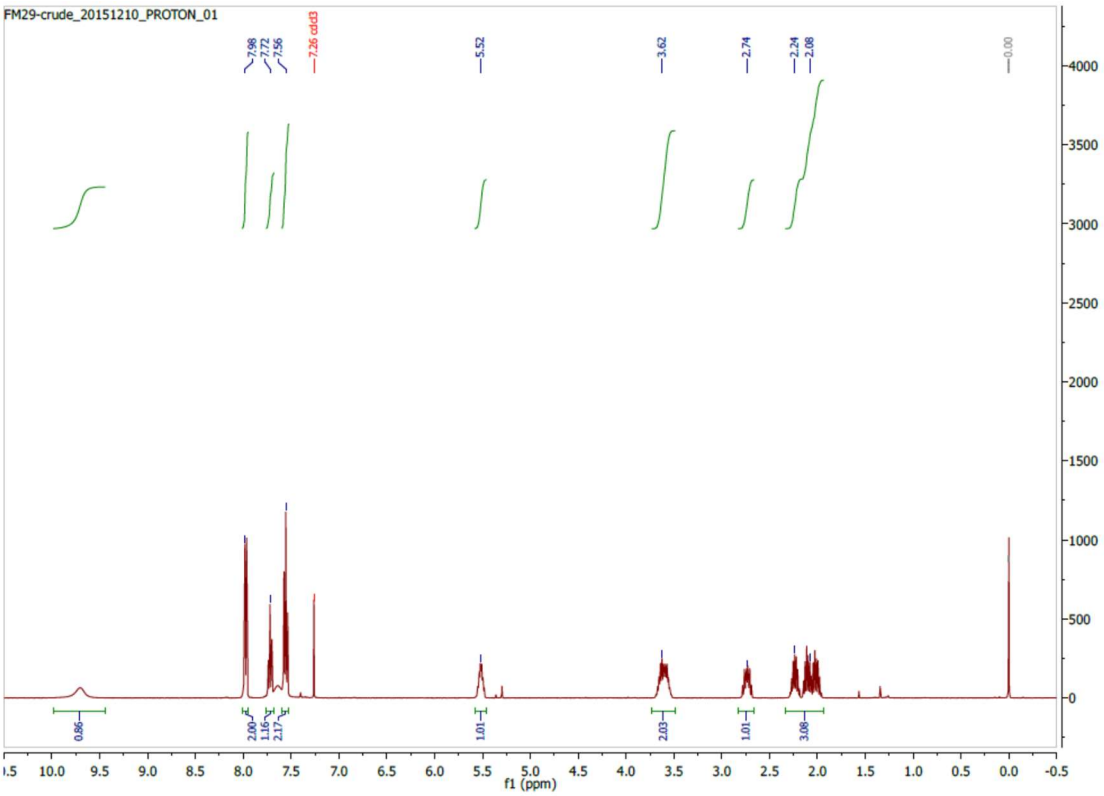

Figure S44. ^{13}C NMR of (*S*)-phenyl(pyrrolidin-2-yl)methanone (2.3).

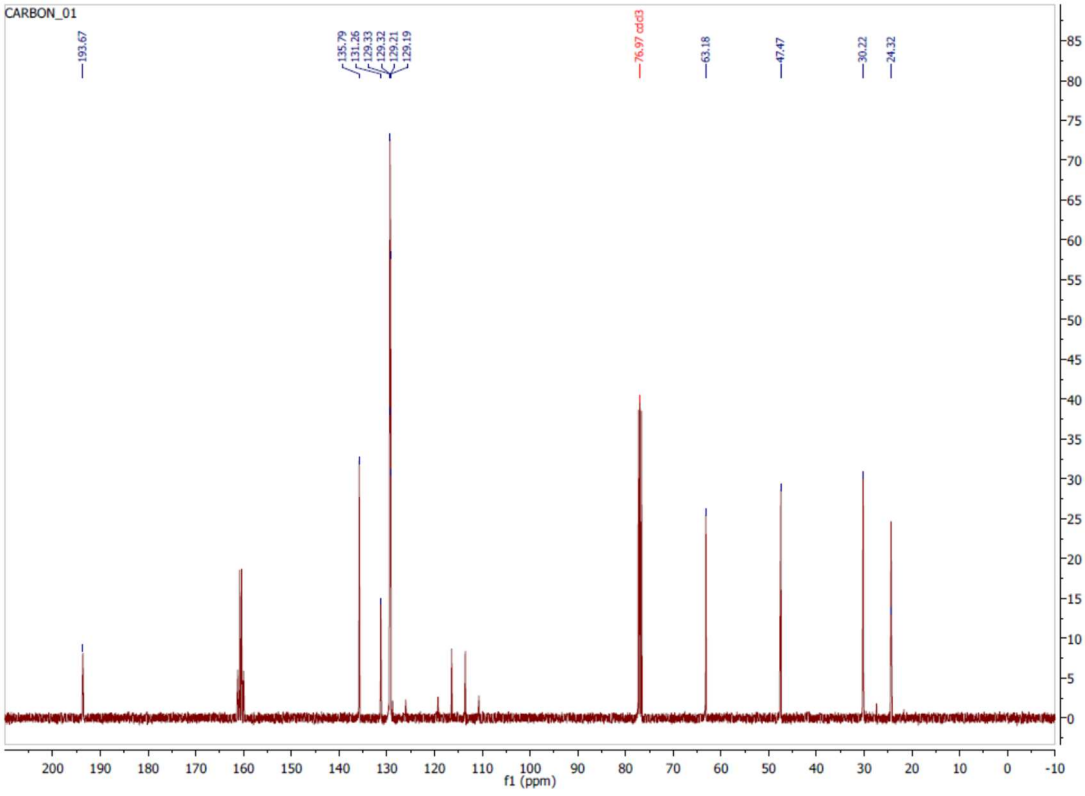

Figure S45. LC-MS of (*S*)-phenyl(pyrrolidin-2-yl)methanone (2.3).

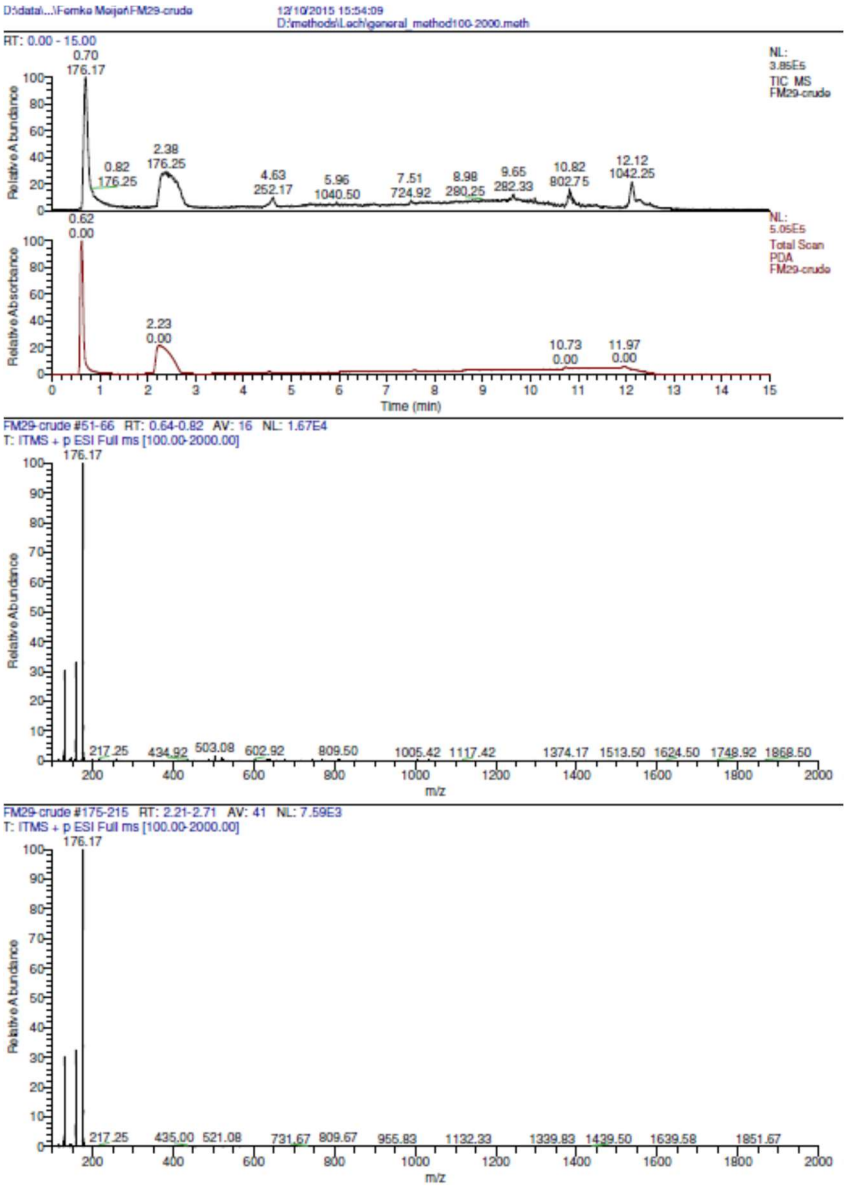

Figure S46. ^{1}H NMR of ethyl (*S*)-2-benzoylpyrrolidine-1-carboxylate (2.4).

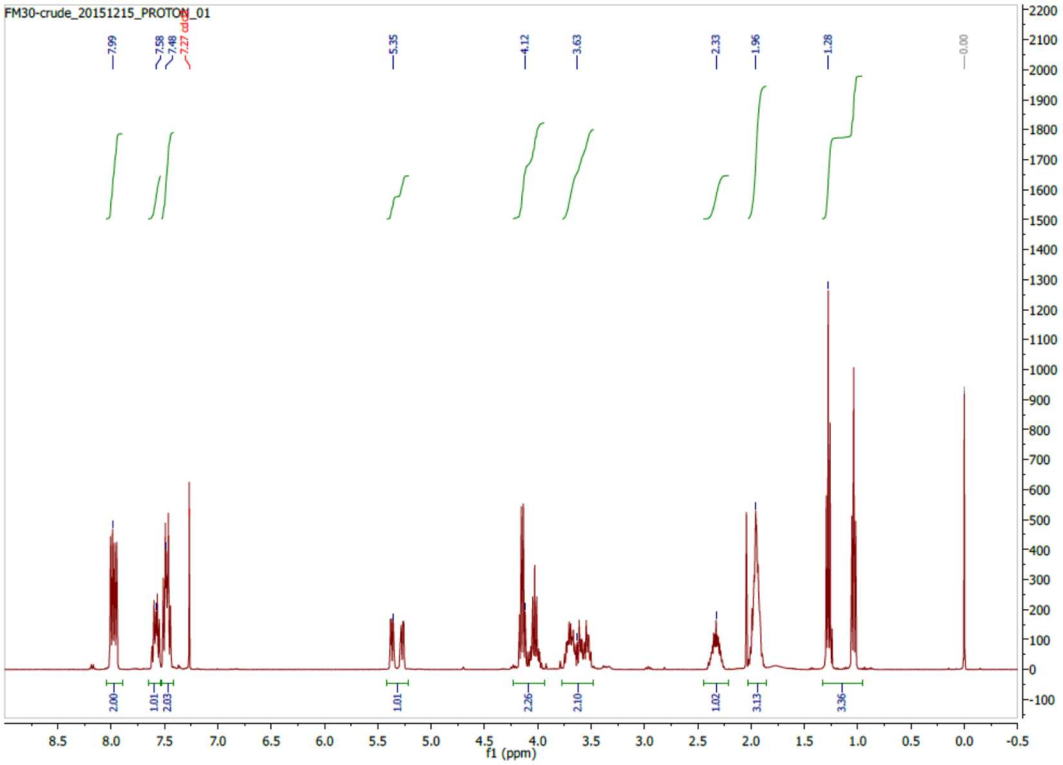

Figure S47. ^{13}C NMR of ethyl (*S*)-2-benzoylpyrrolidine-1-carboxylate (2.4).

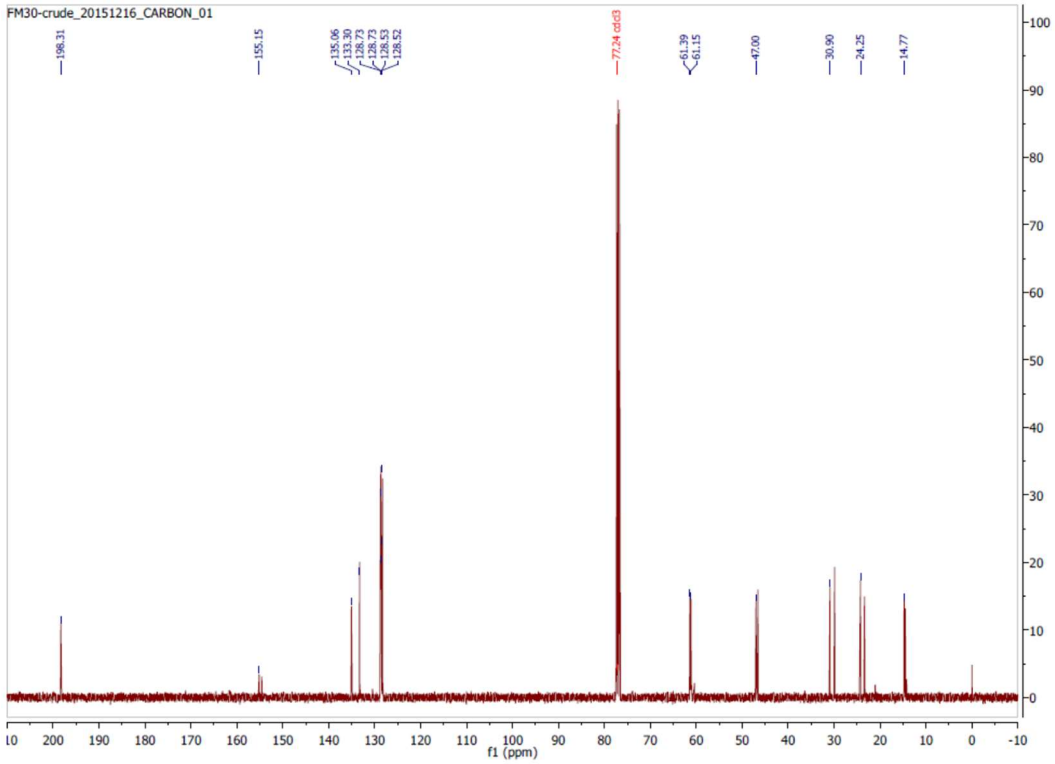

Figure S48. LC-MS of ethyl (*S*)-2-benzoylpyrrolidine-1-carboxylate (2.4).

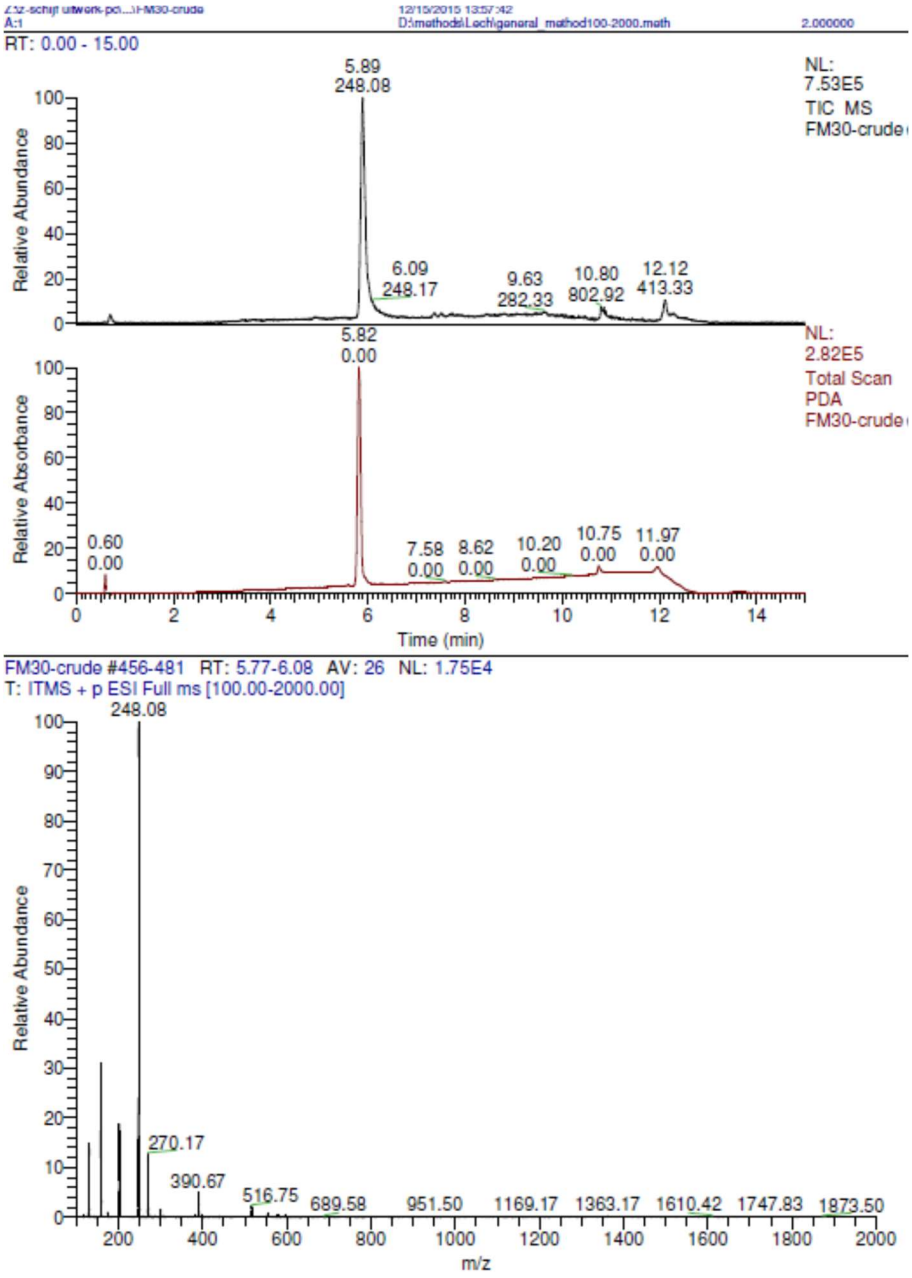

Figure S49. ^{1}H NMR of 1-bromo-2-(2-methoxyethoxy)benzene.

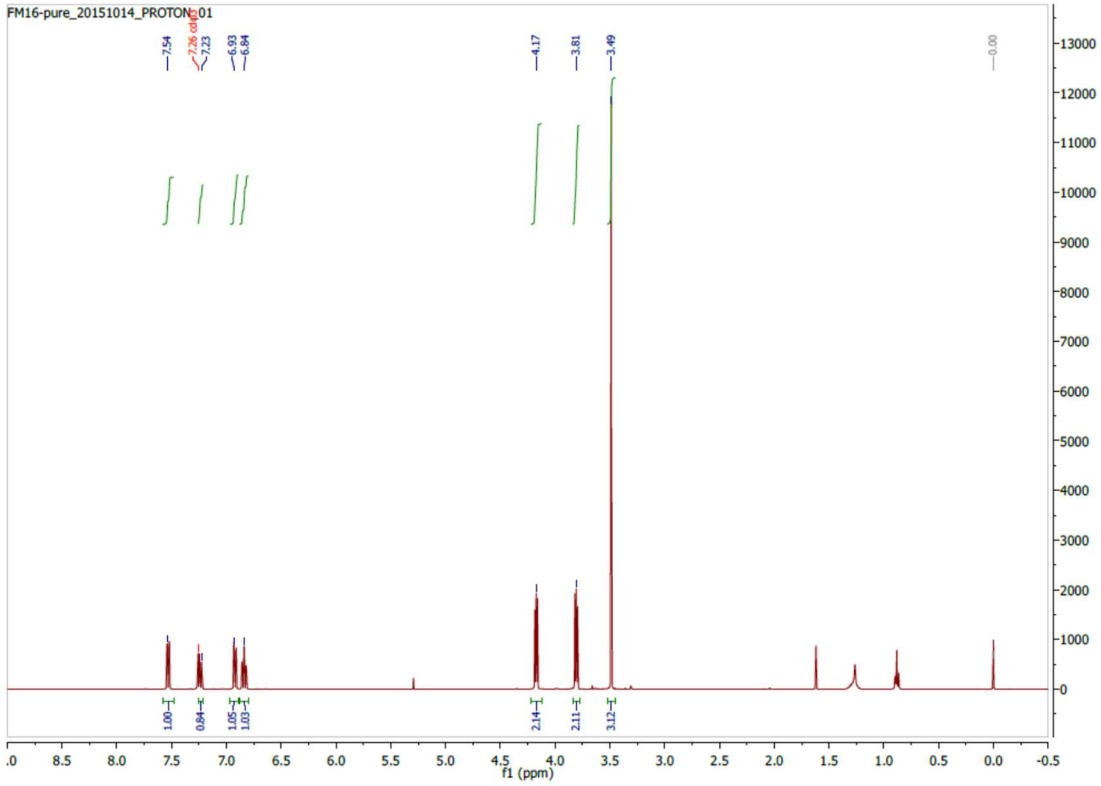

Figure S50. ^{13}C NMR of 1-bromo-2-(2-methoxyethoxy)benzene.

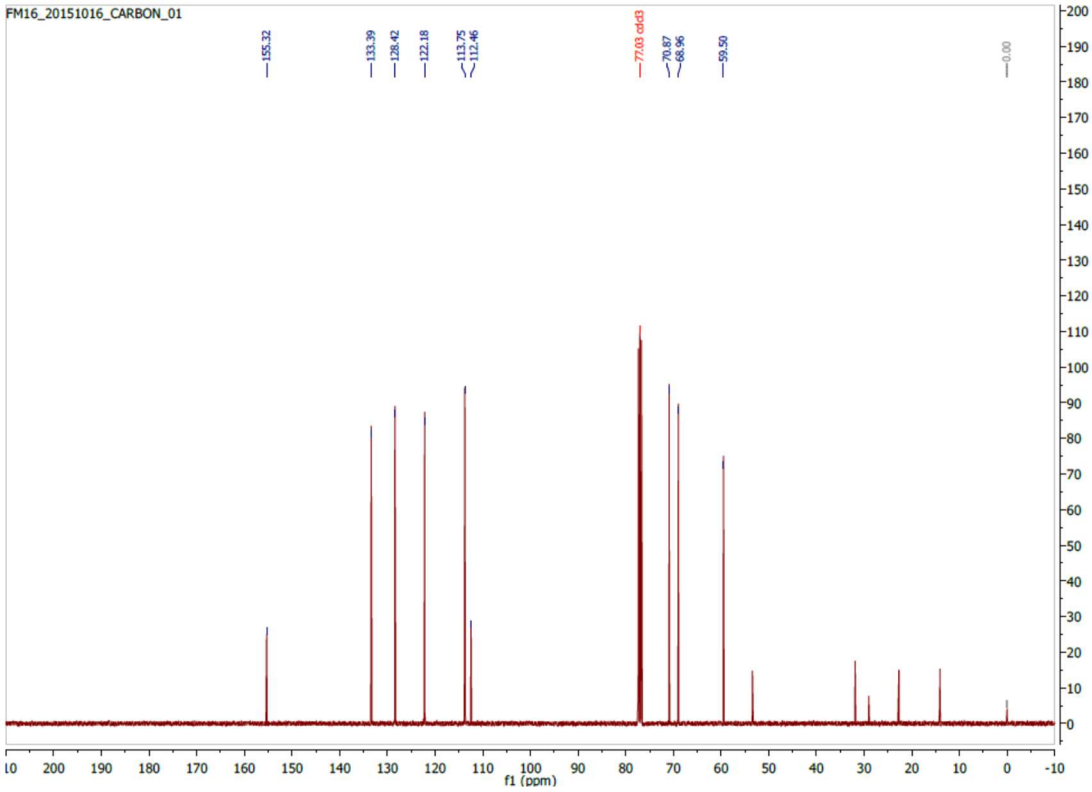

Figure S51. GC-MS of 1-bromo-2-(2-methoxyethoxy)benzene.

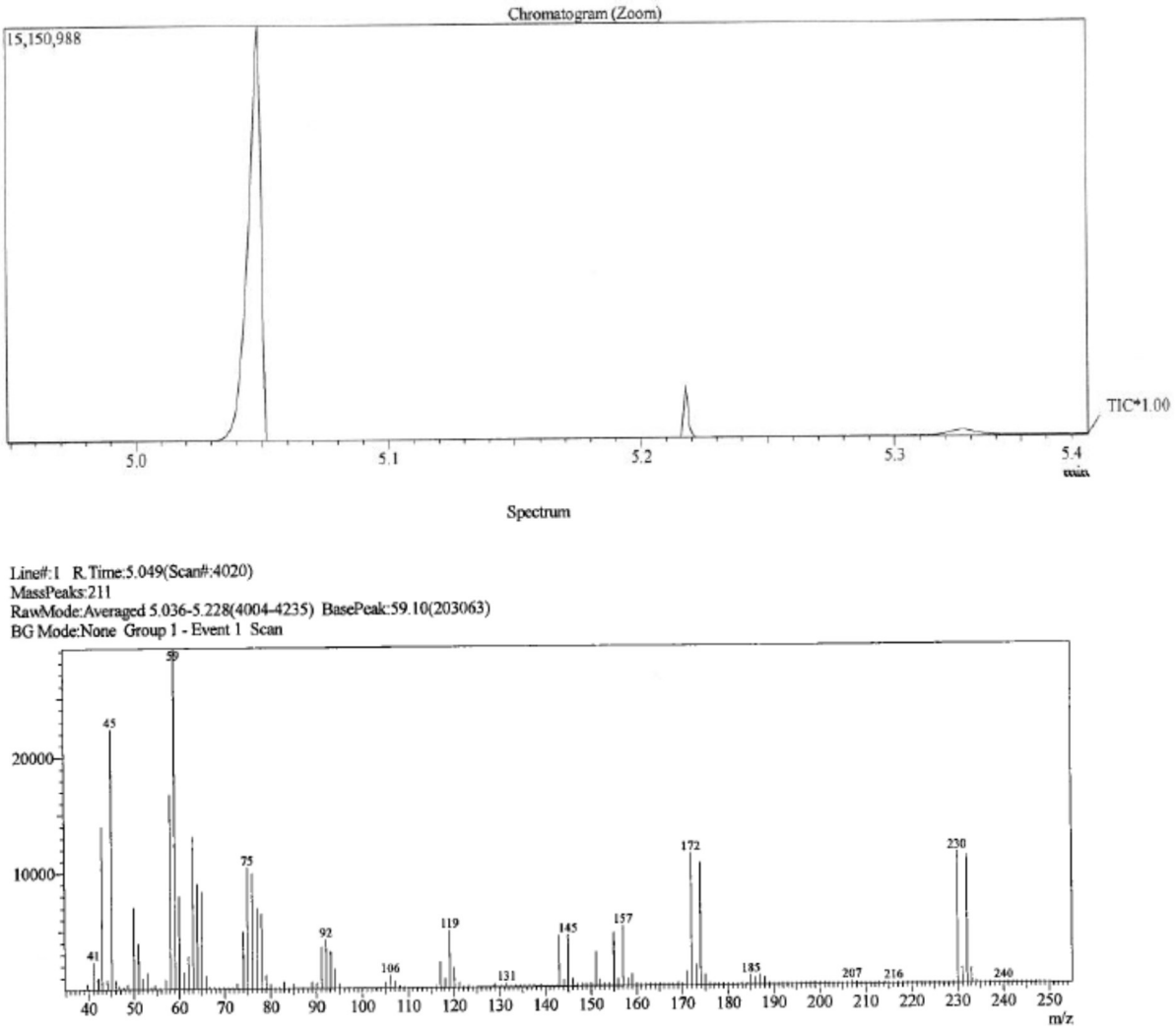

-

Figure S52. ^{1}H NMR of 1-bromo-3-(2-methoxyethoxy)benzene.

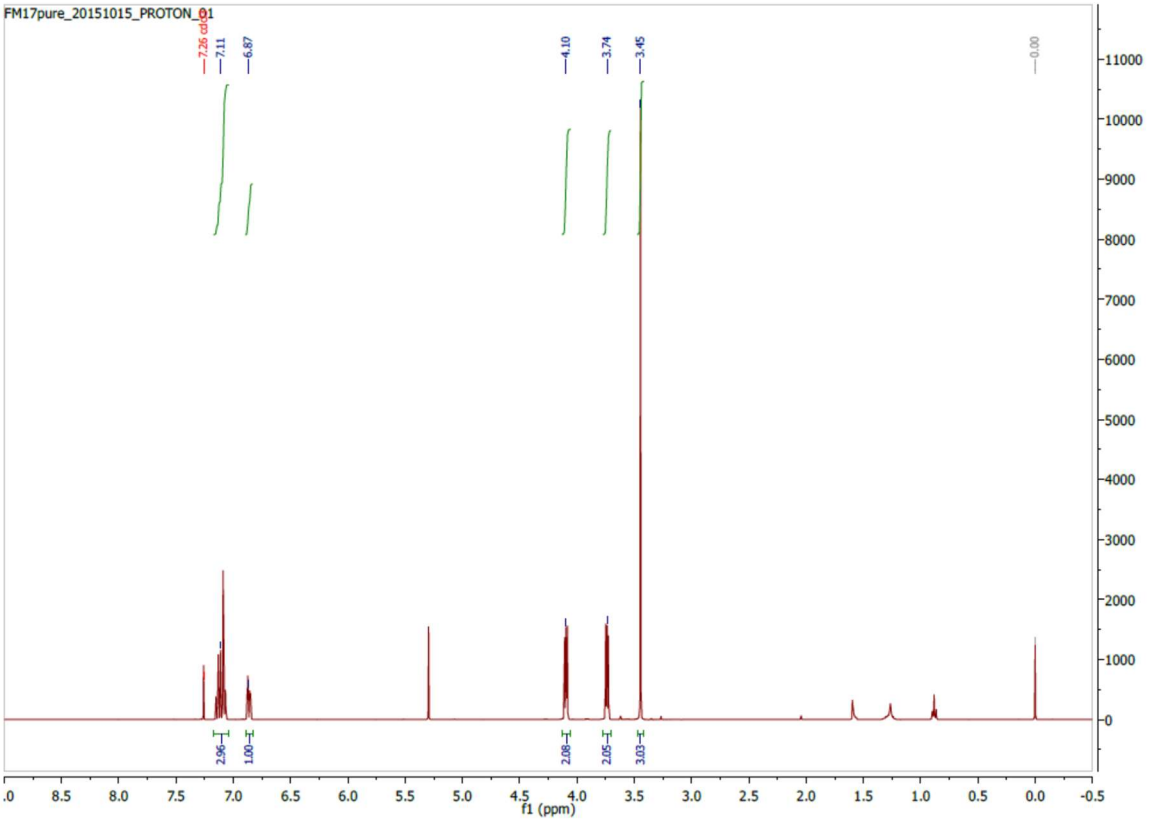

Figure S53. ^{13}C NMR of 1-bromo-3-(2-methoxyethoxy)benzene.

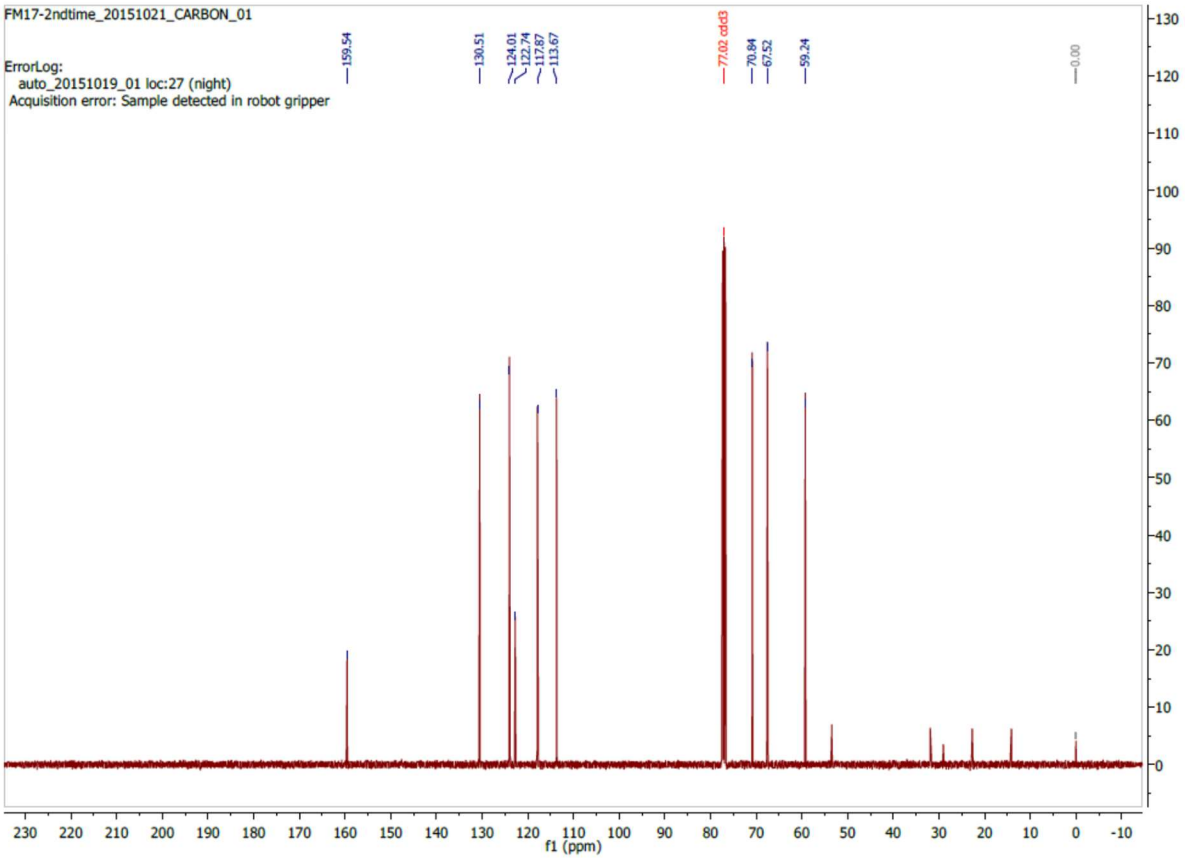

Figure S54. GC-MS of 1-bromo-3-(2-methoxyethoxy)benzene.

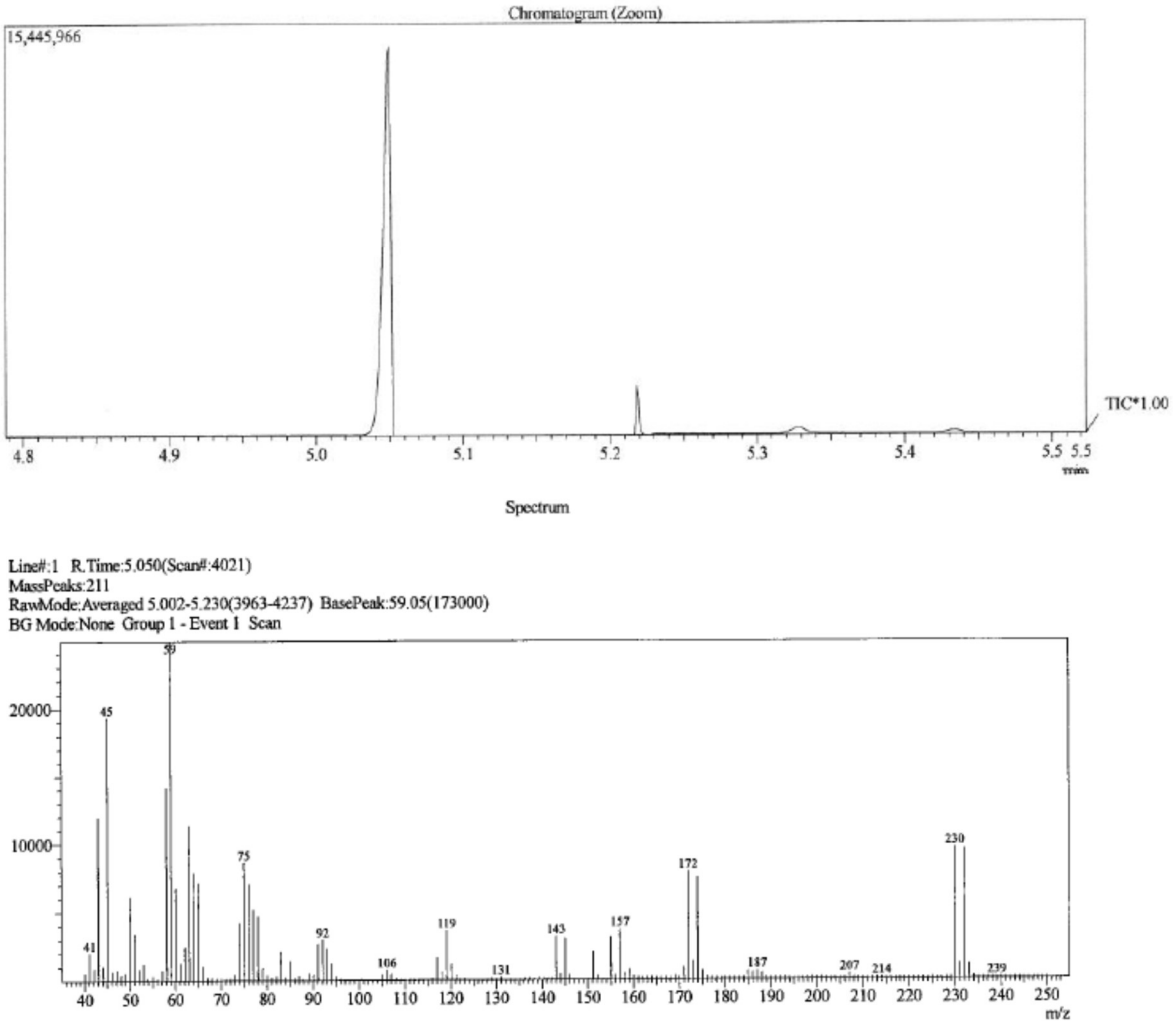

Figure S55. ^{1}H NMR of pyrrolooxazolone 2.5a.

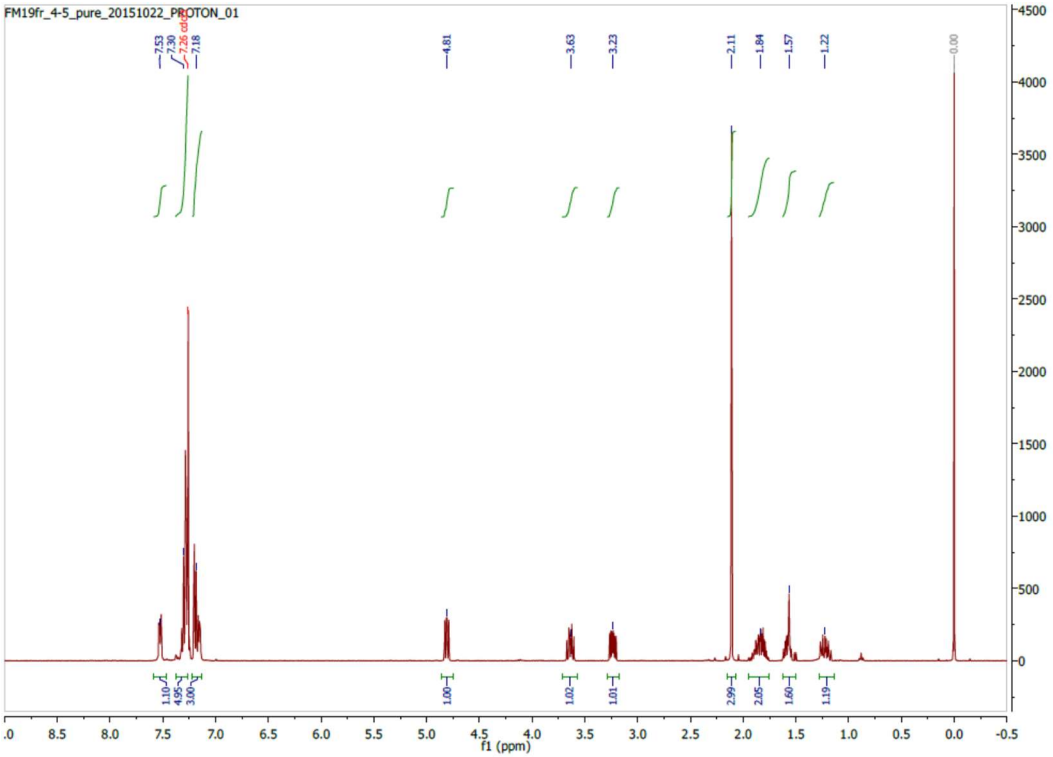

Figure S56. ^{13}C NMR of pyrrolooxazolone 2.5a.

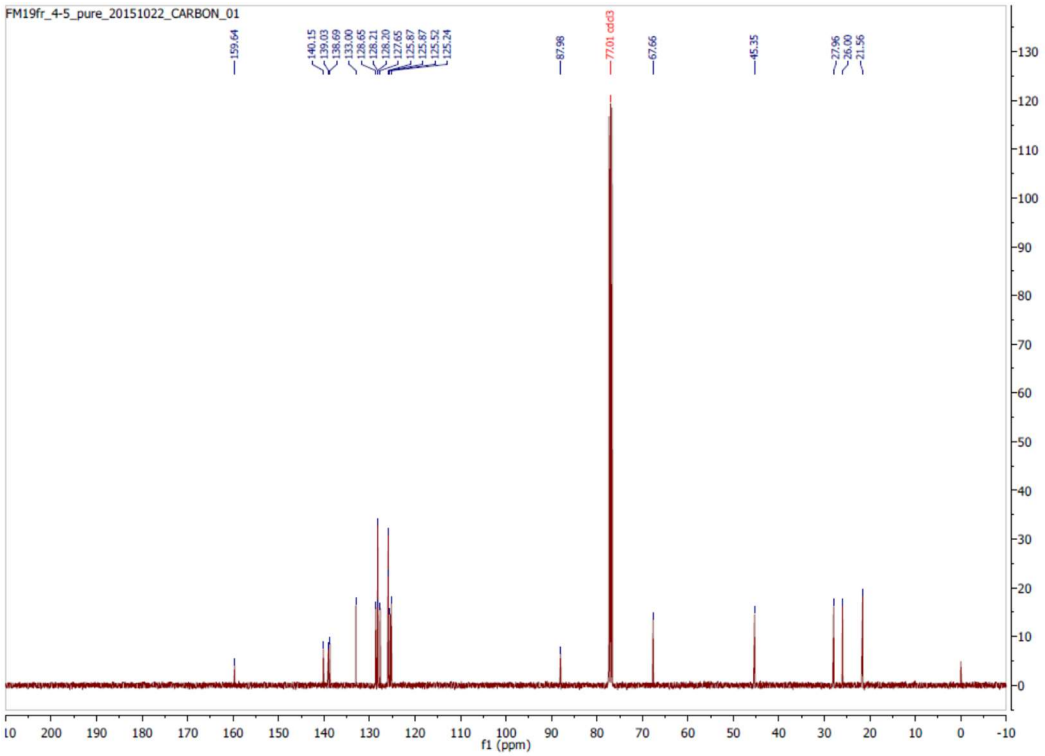

Figure S57. LC-MS of pyrrolooxazolone 2.5a.

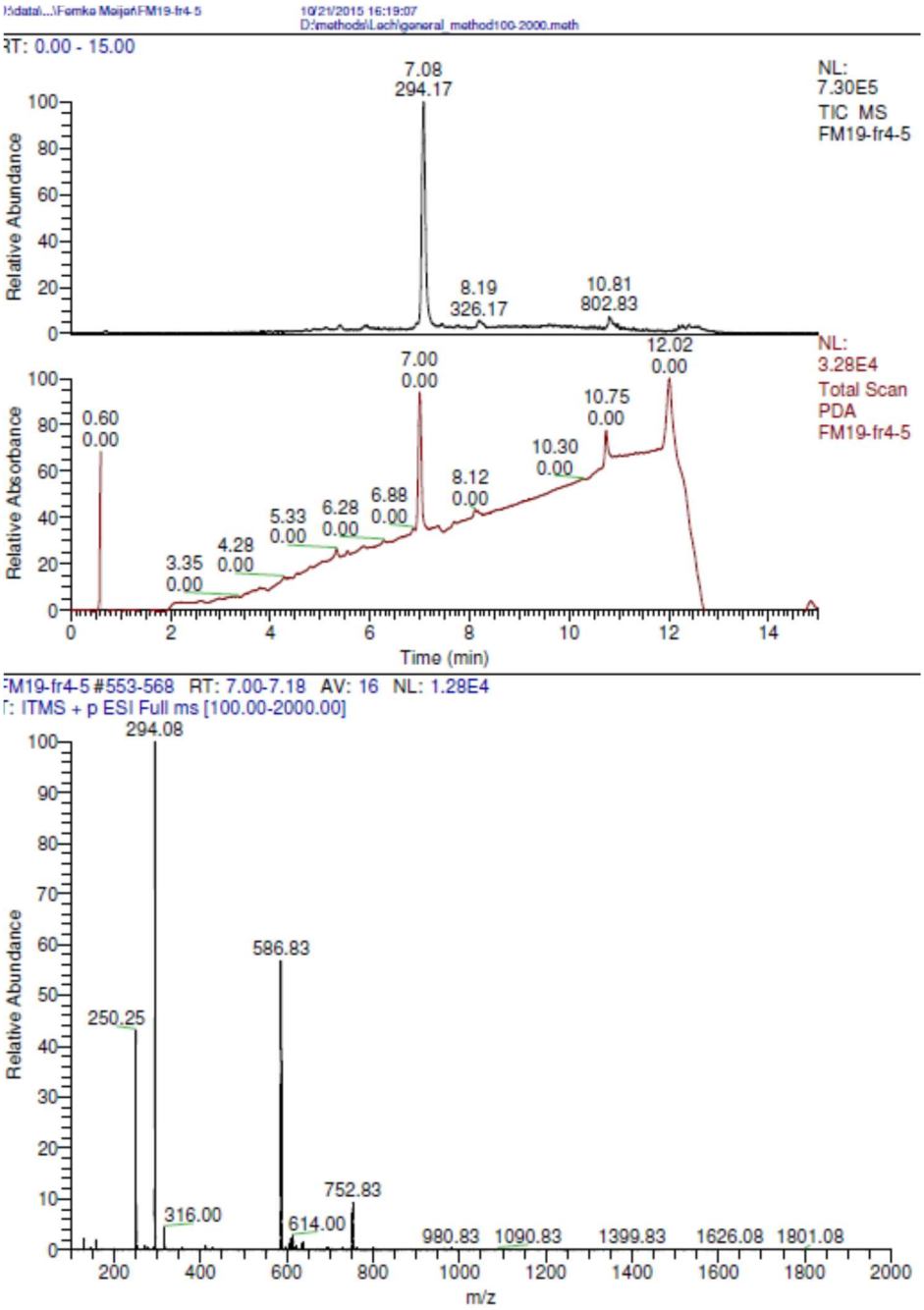

Figure S58. ^{1}H NMR of pyrrolooxazolone 2.5b.

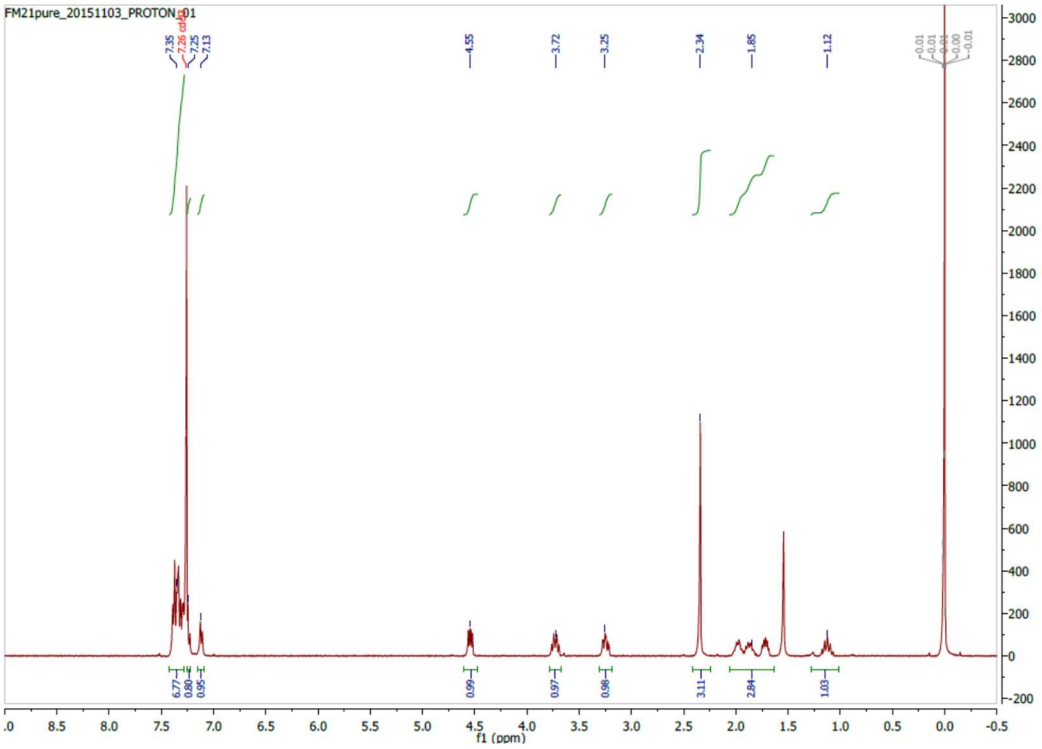

Figure S59. ^{13}C NMR of pyrrolooxazolone 2.5b.

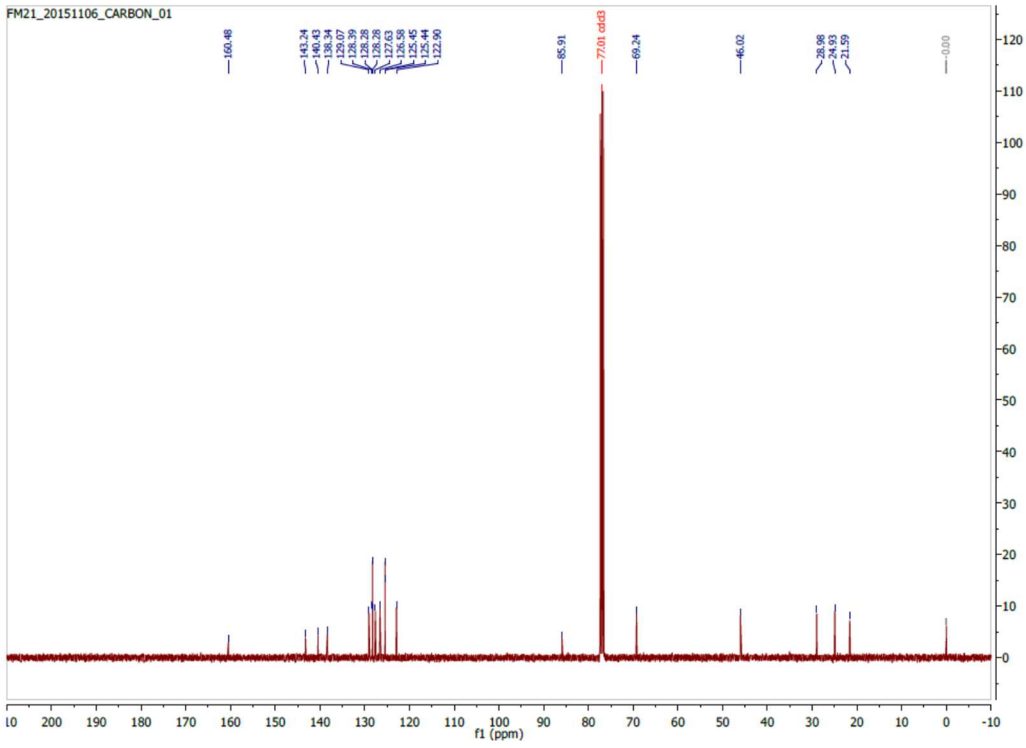

Figure S60. LC-MS of pyrrolooxazolone 2.5b.

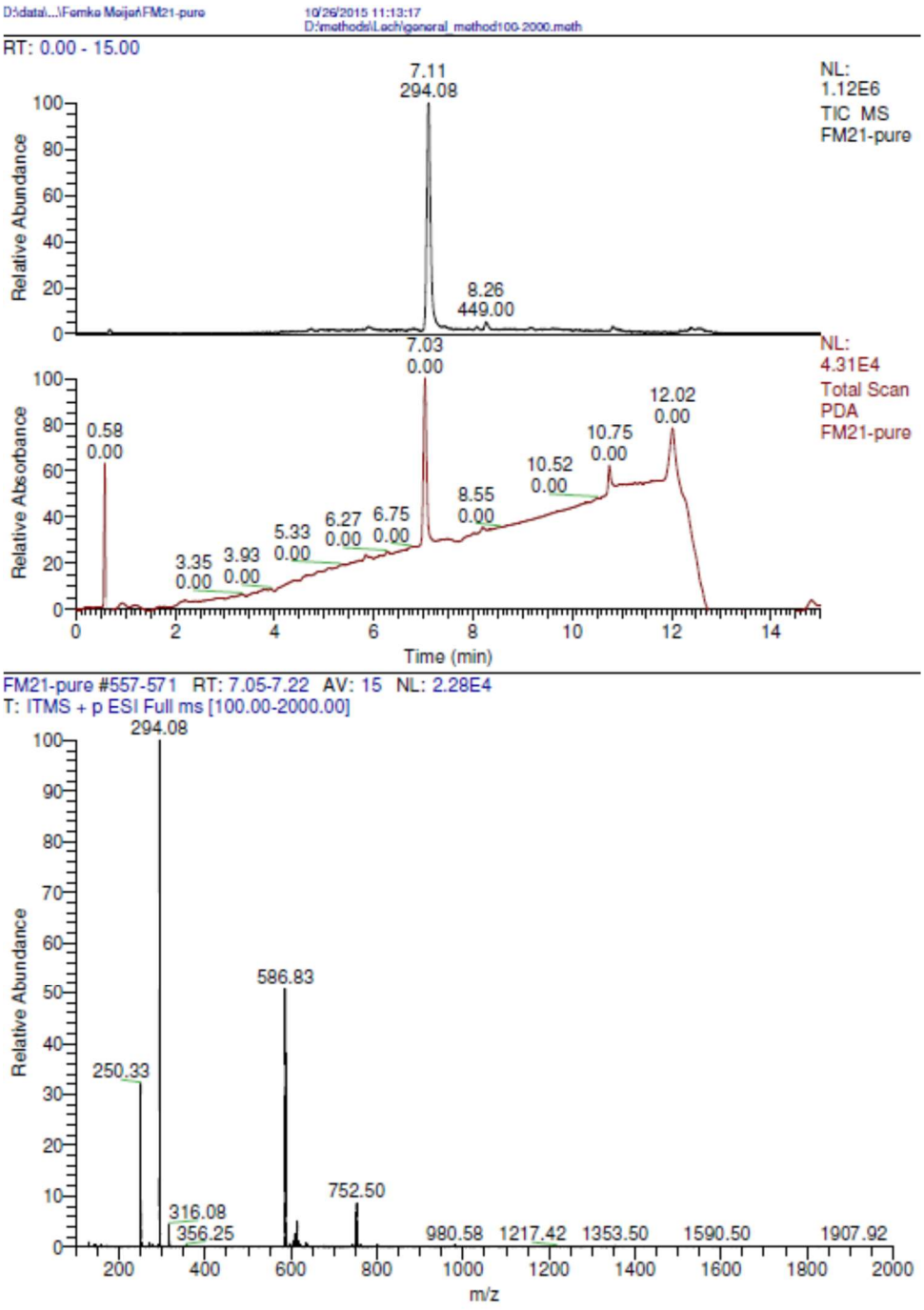

Figure S61. ^{1}H NMR of pyrrolooxazolone 2.5c.

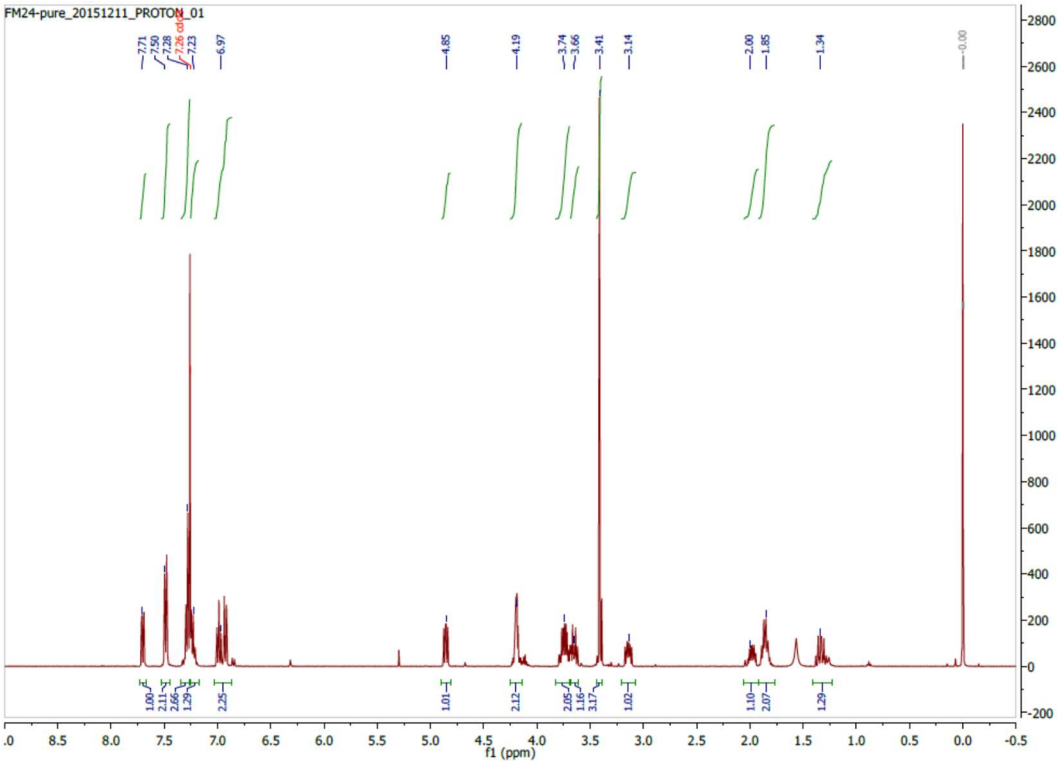

Figure S62. ^{13}C NMR of pyrrolooxazolone 2.5c.

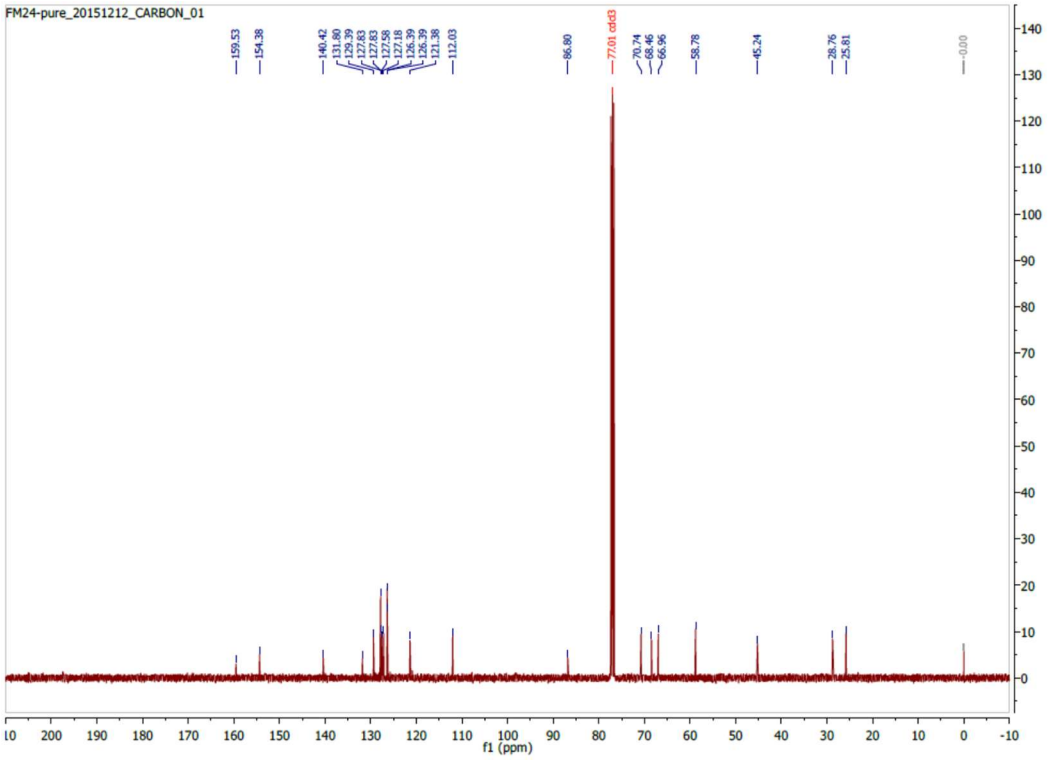

Figure S63. LC-MS of pyrrolooxazolone 2.5c.

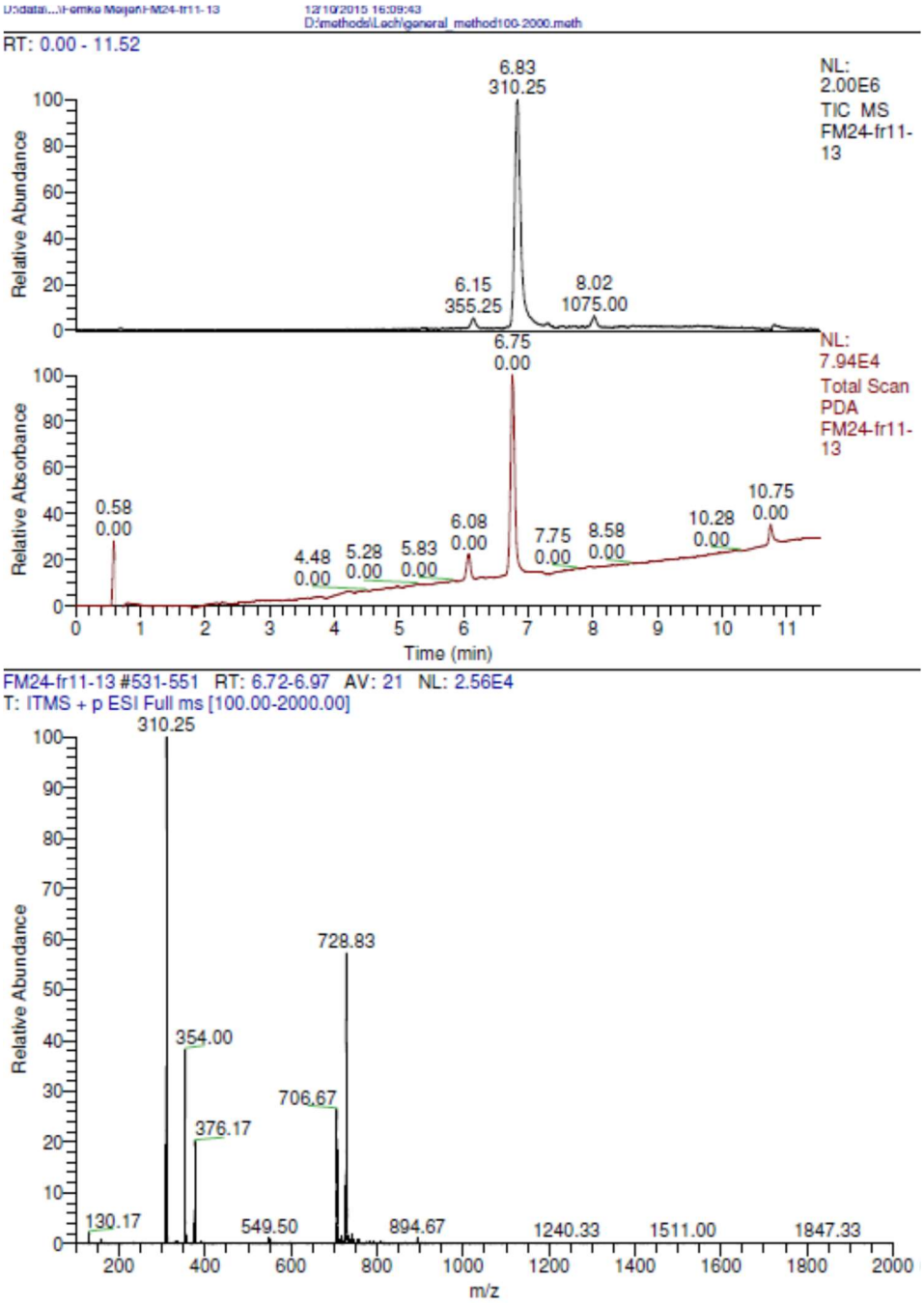

Figure S64. ^{1}H NMR of pyrrolooxazolone 2.5d.

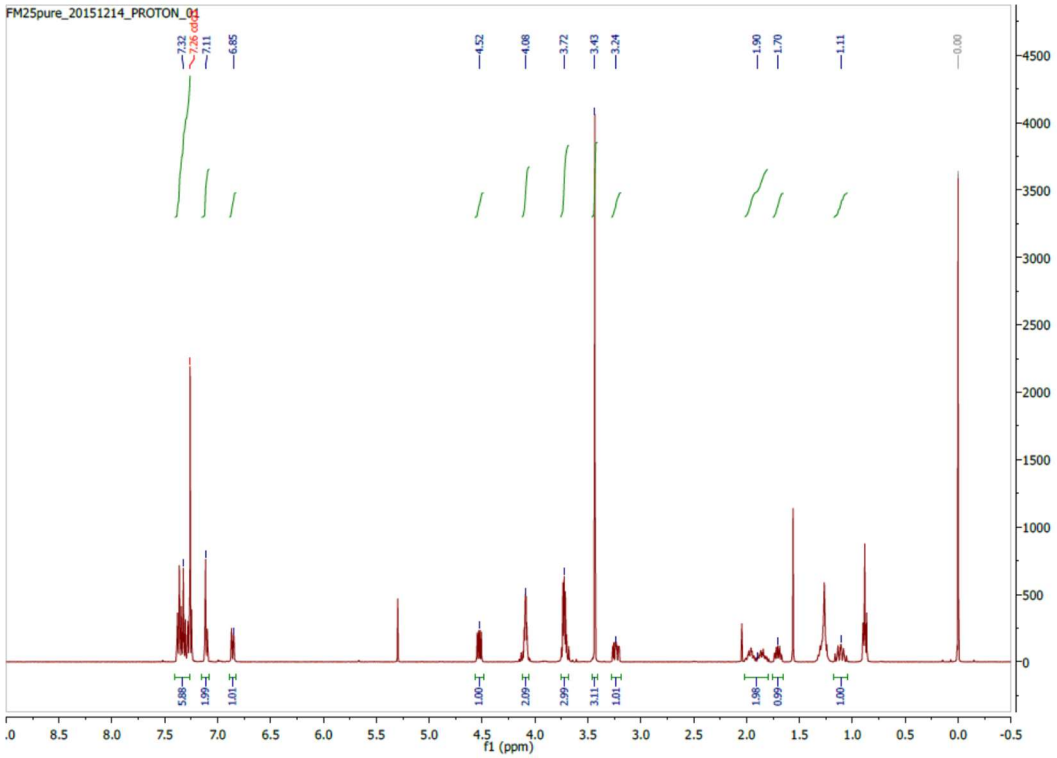

Figure S65. ^{13}C NMR of pyrrolooxazolone 2.5d.

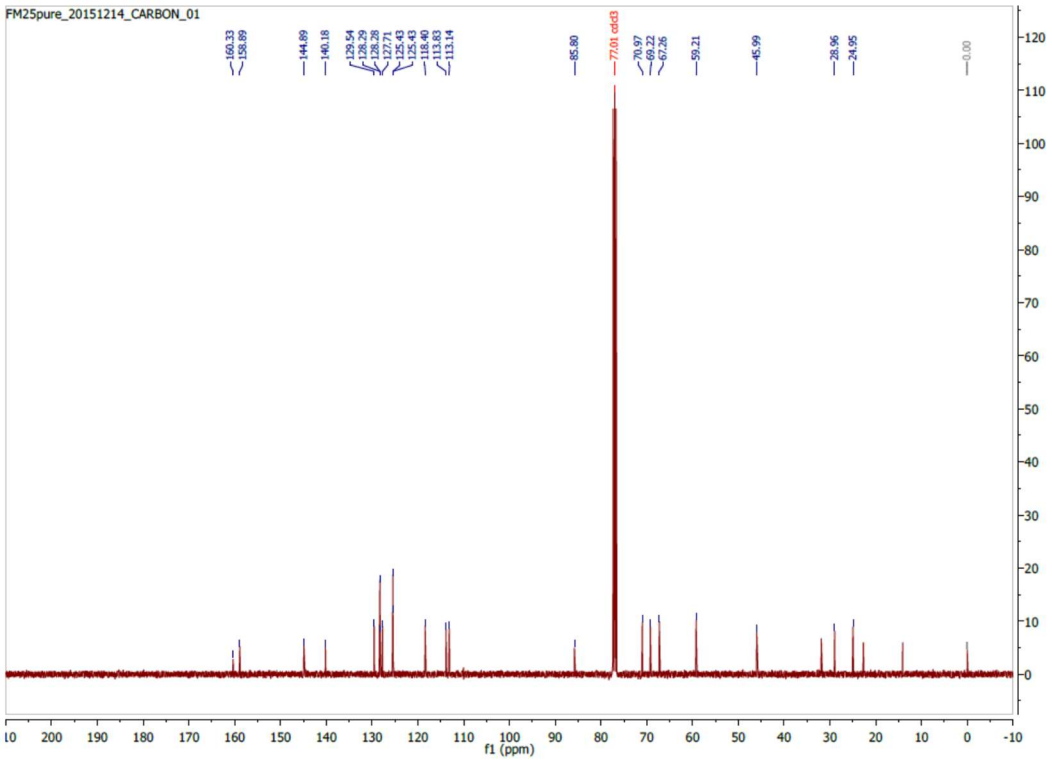

Figure S66. LC-MS of pyrrolooxazolone 2.5d.

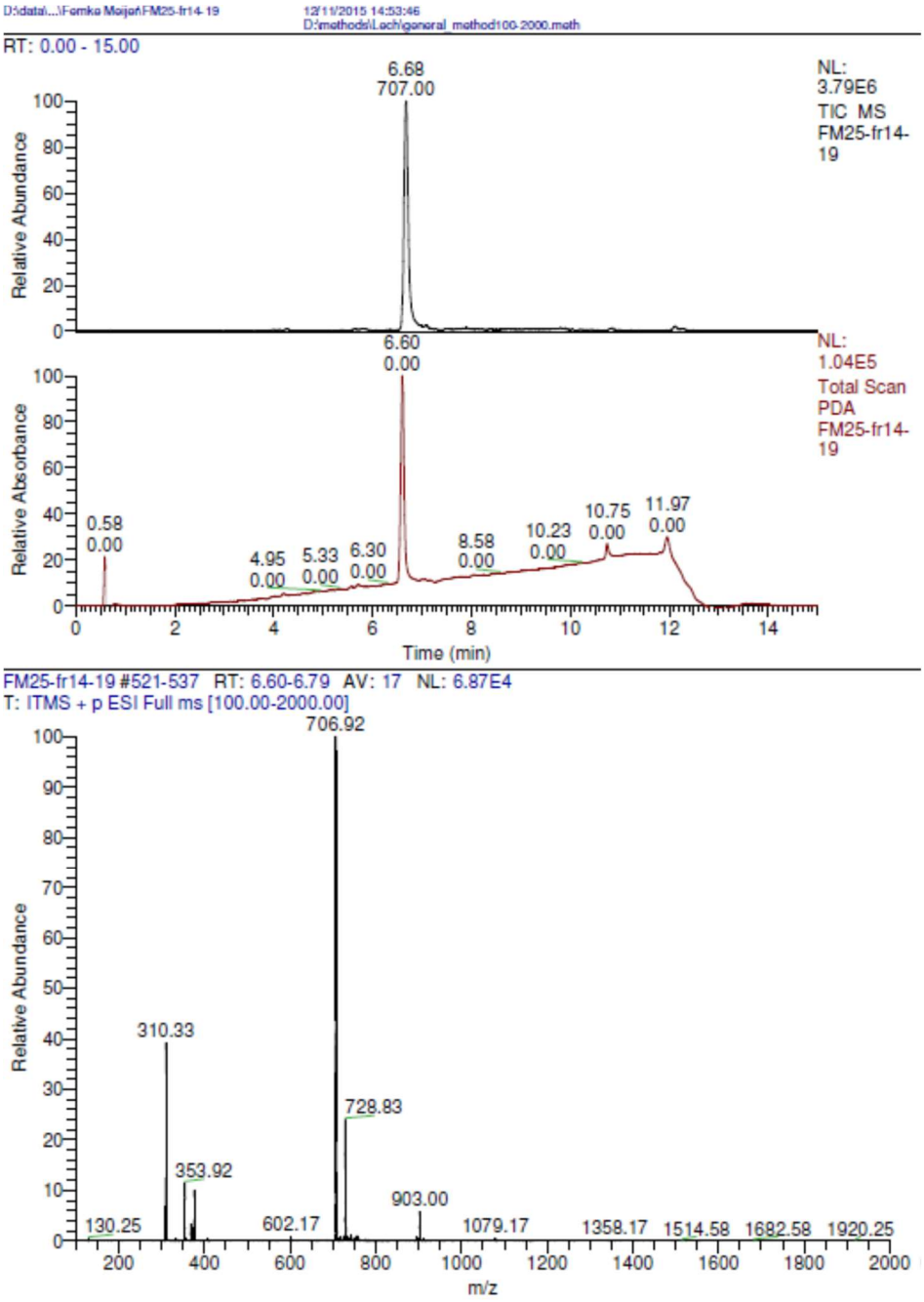

Figure S67. ^{1}H NMR of pyrrolooxazolone 2.5e.

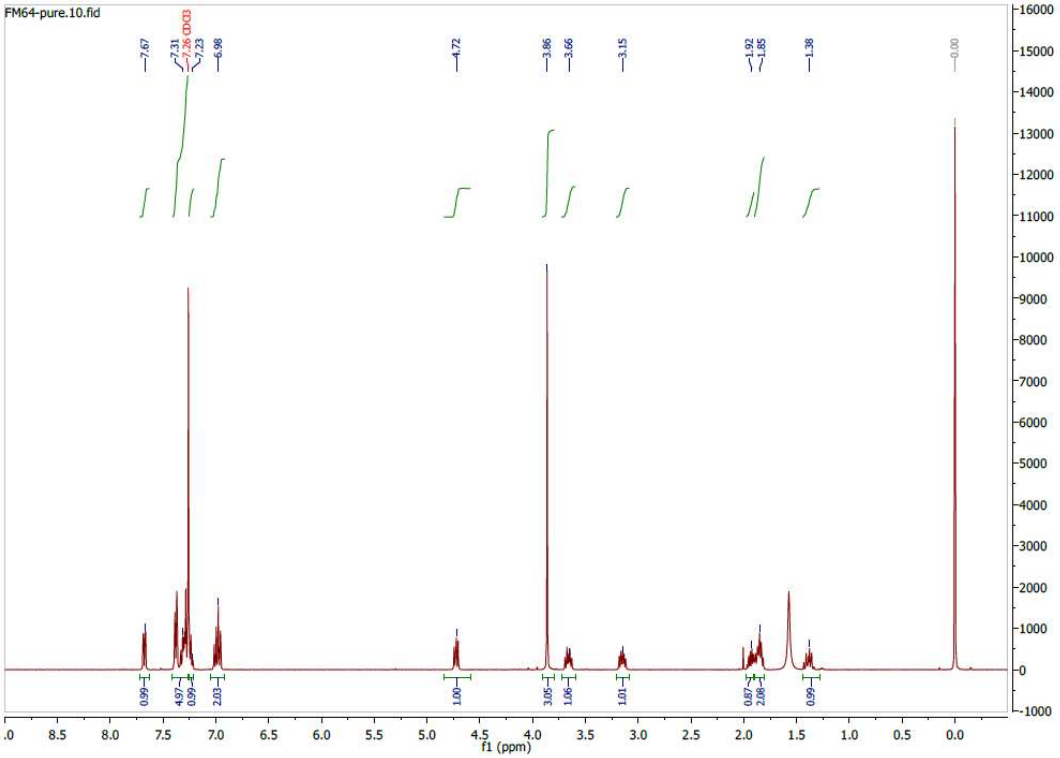

Figure S68. ^{13}C NMR of pyrrolooxazolone 2.5e.

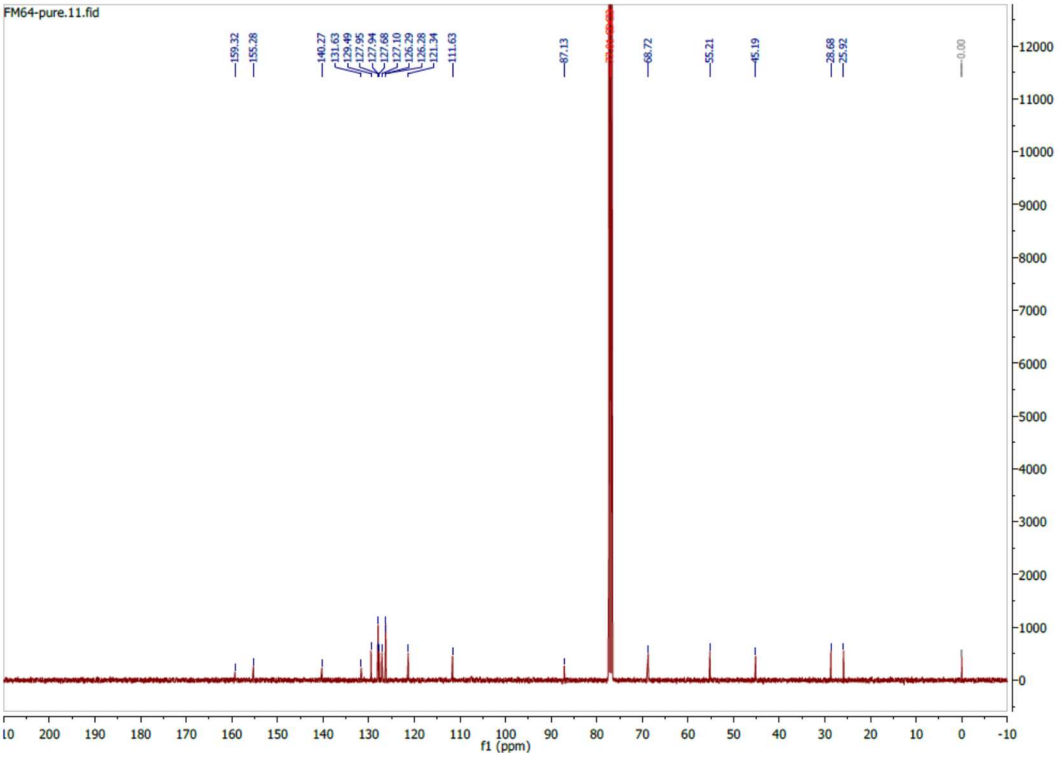

Figure S69. LC-MS of pyrrolooxazolone 2.5e.

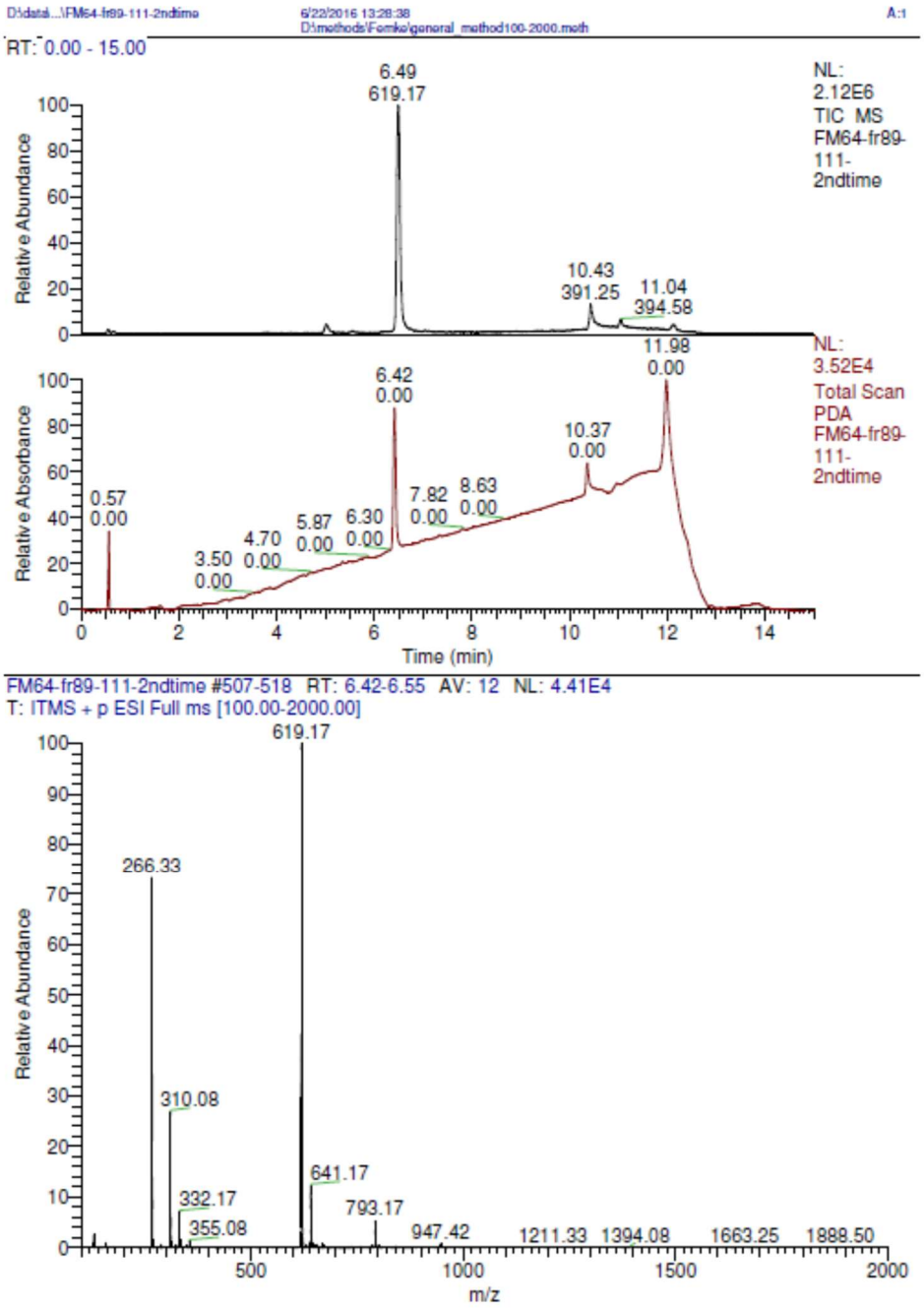

Figure S70. ^{1}H NMR of pyrrolooxazolone 2.5f.

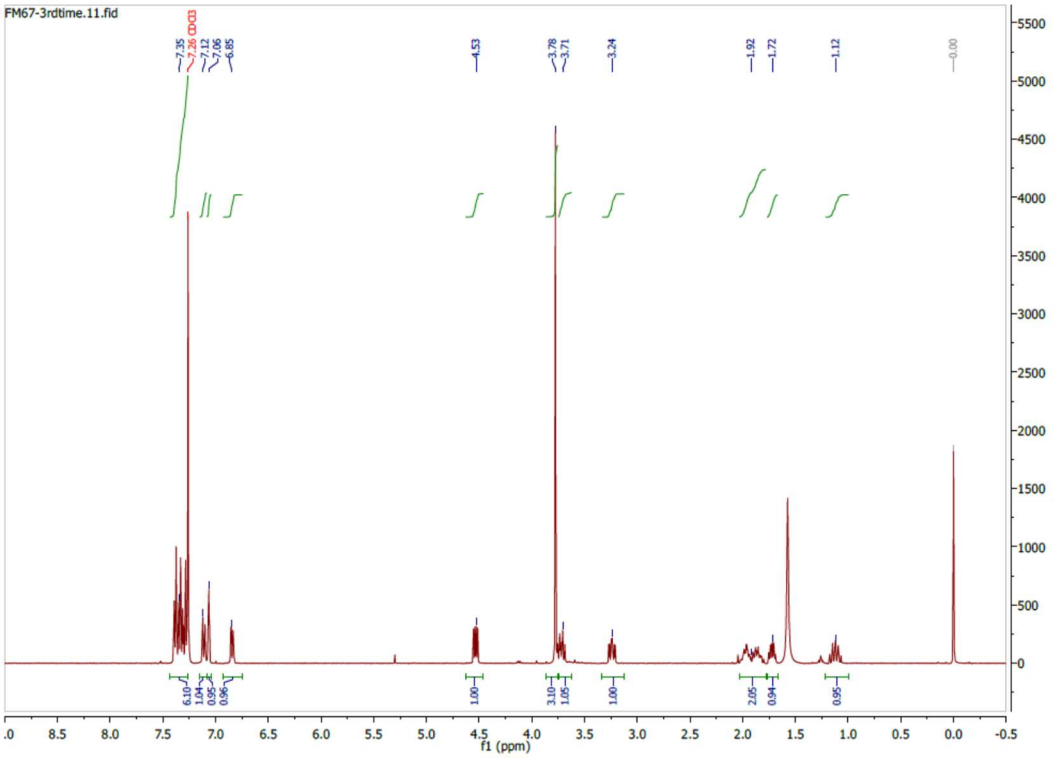

Figure S71. ^{13}C NMR of pyrrolooxazolone 2.5f.

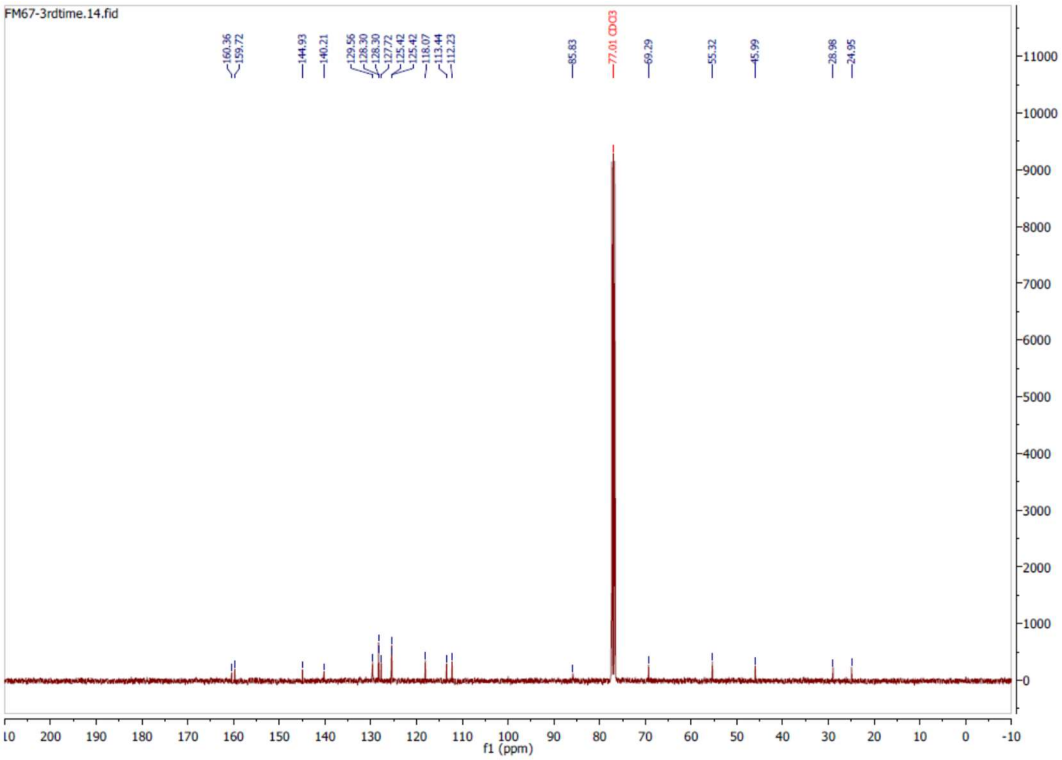

Figure S72. LC-MS of pyrrolooxazolone 2.5f.

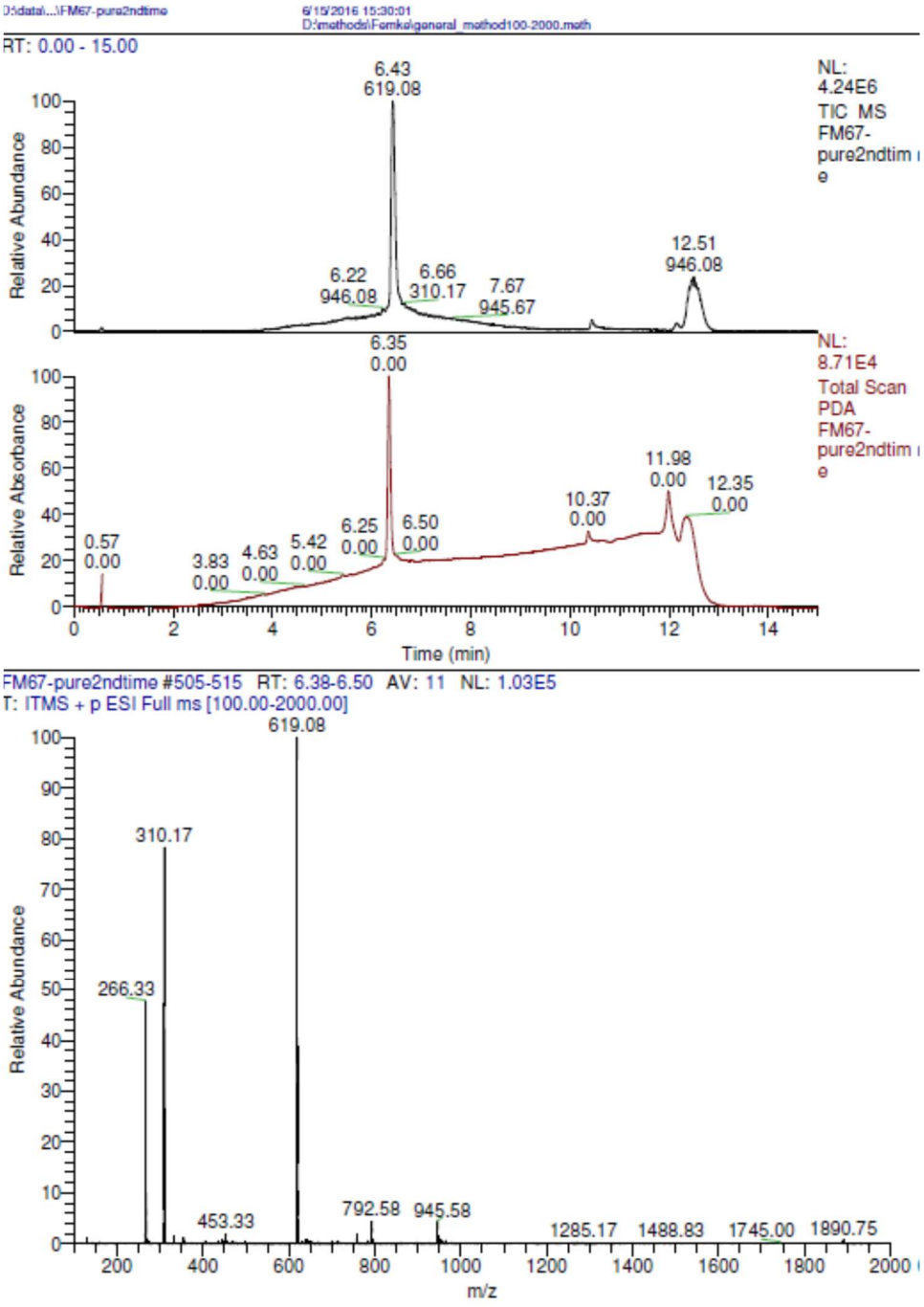

Figure S73. ^{1}H NMR of pyrrolooxazolone 2.5g.

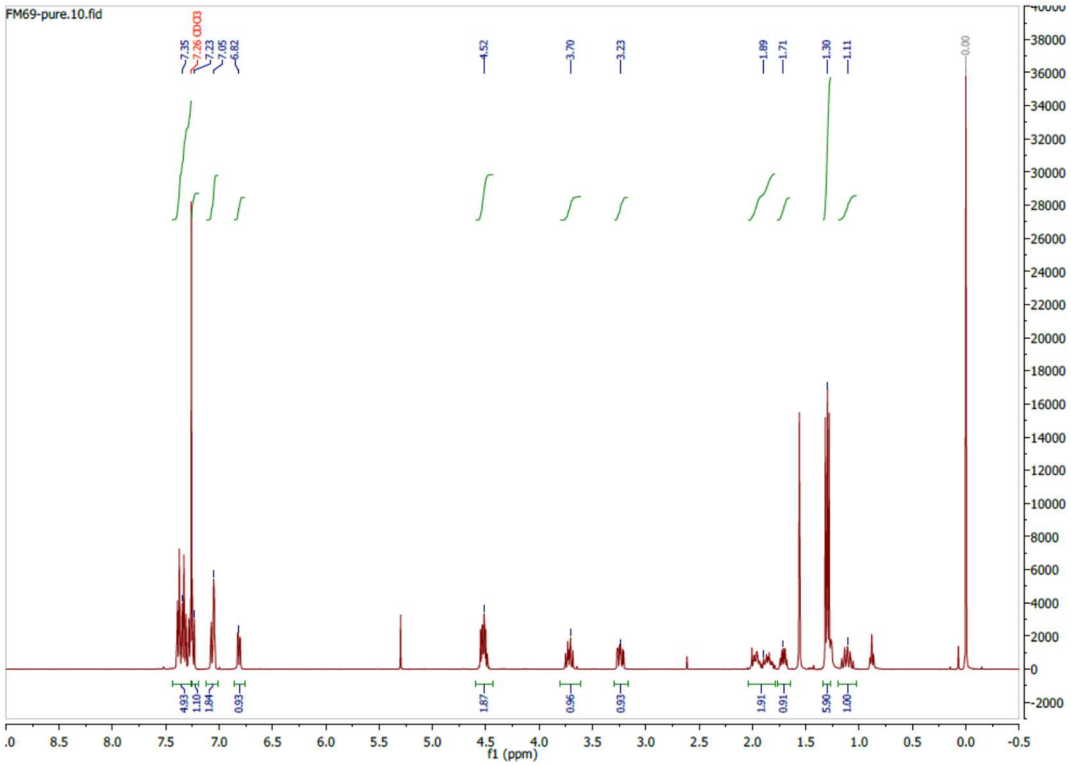

Figure S74. ^{13}C NMR of pyrrolooxazolone 2.5g.

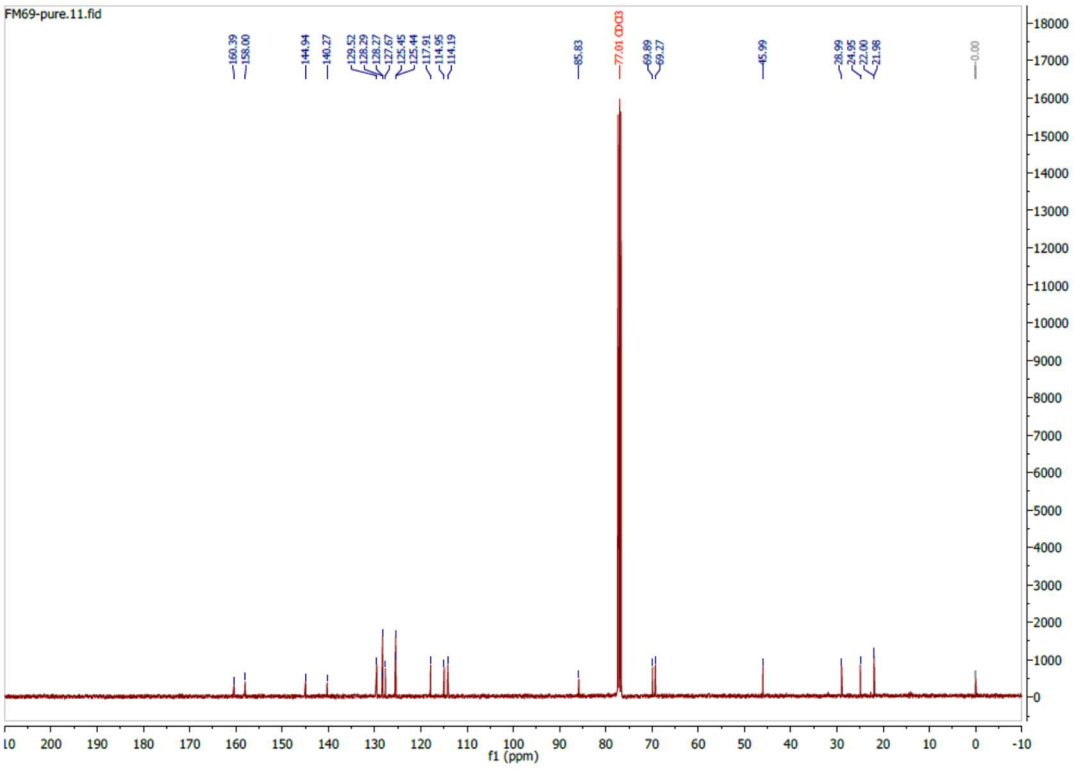

Figure S75. LC-MS of pyrrolooxazolone 2.5g.

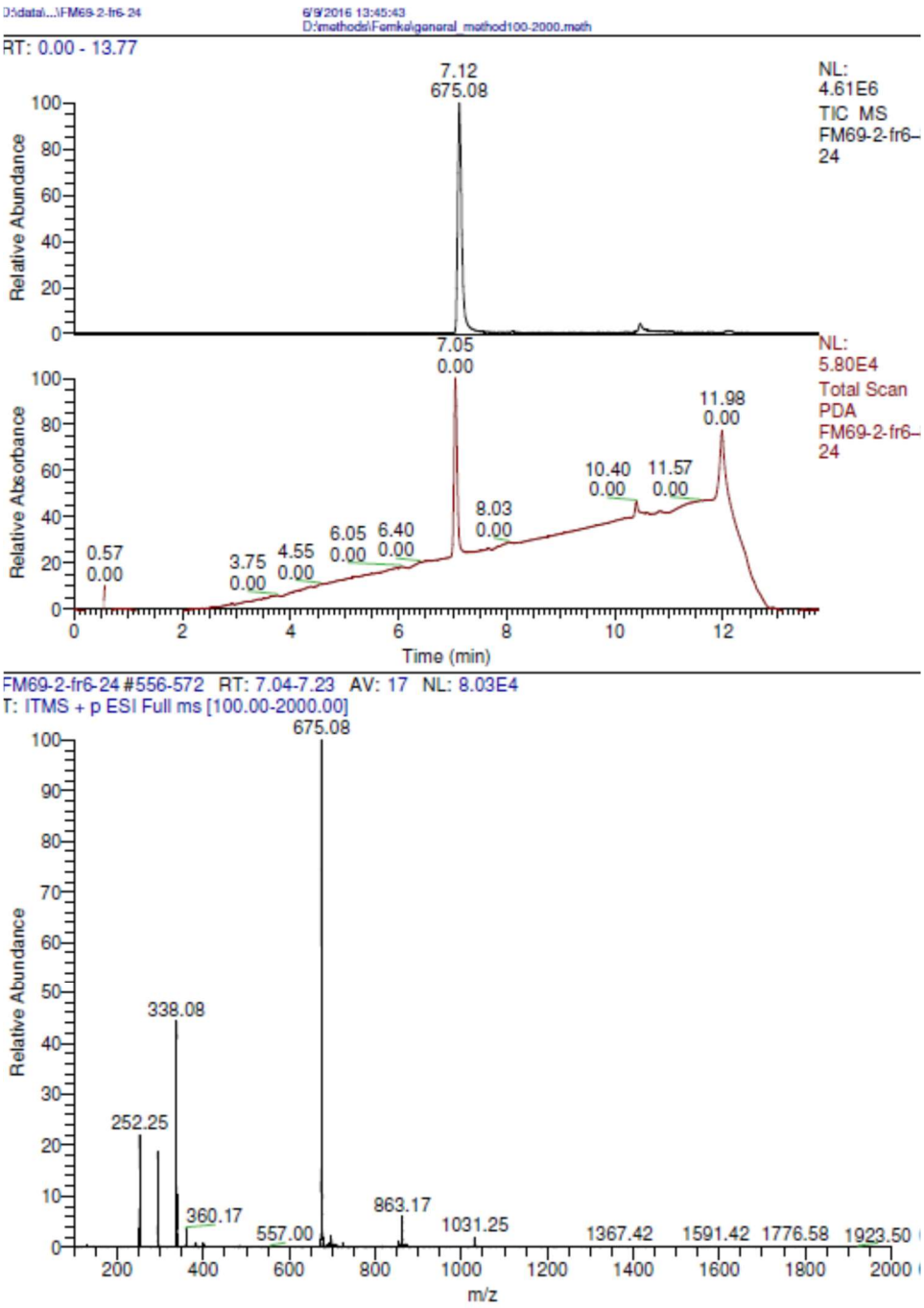

Figure S76. ^{1}H NMR of benzhydryl pyrrolidine derivative 2.6a.

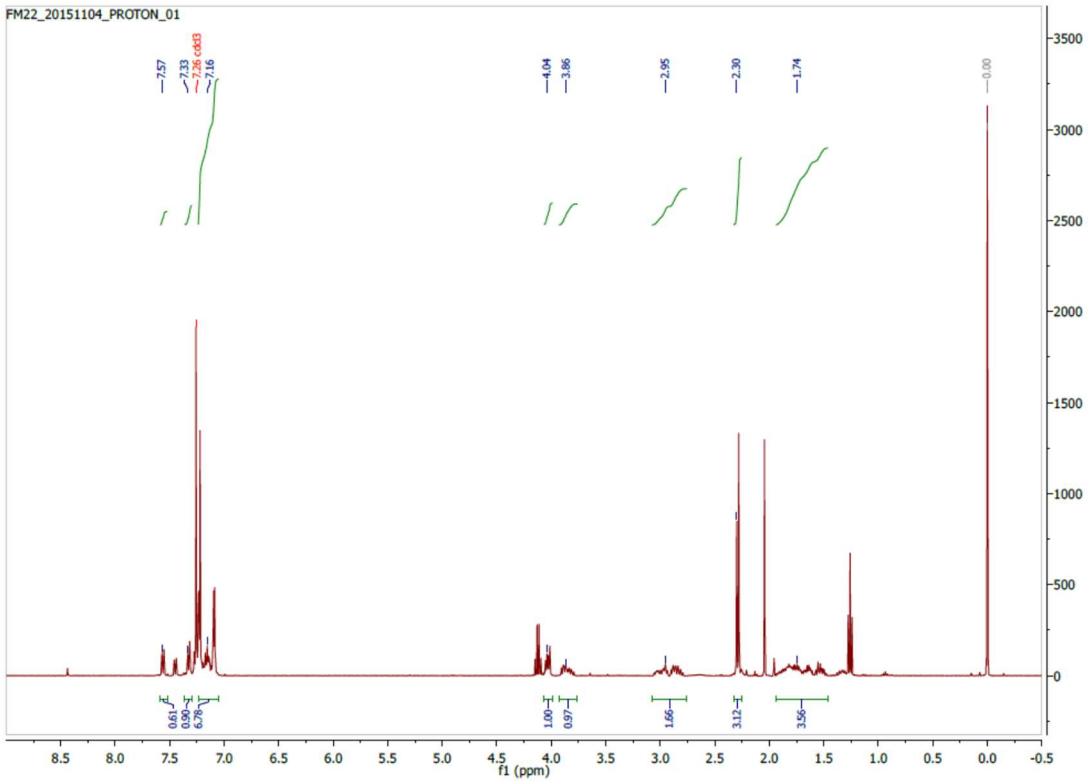

Figure S77. ^{13}C NMR of of benzhydryl pyrrolidine derivative 2.6a.

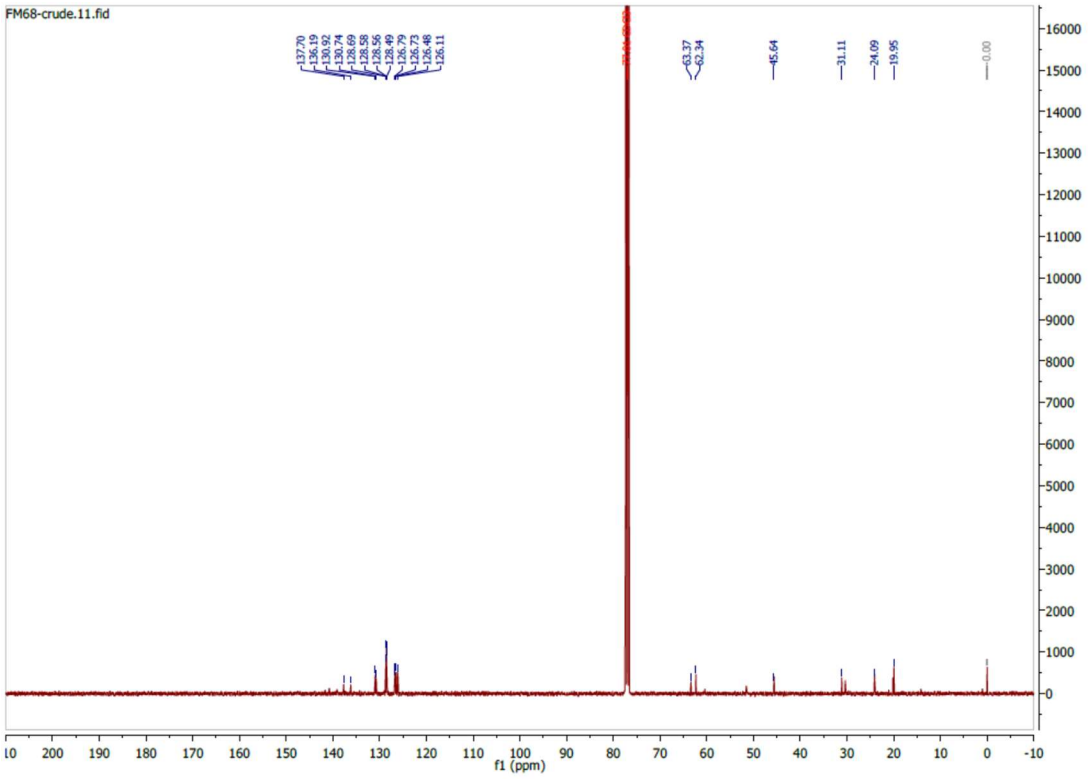

Figure S78. LC-MS of of benzhydryl pyrrolidine derivative 2.6a.

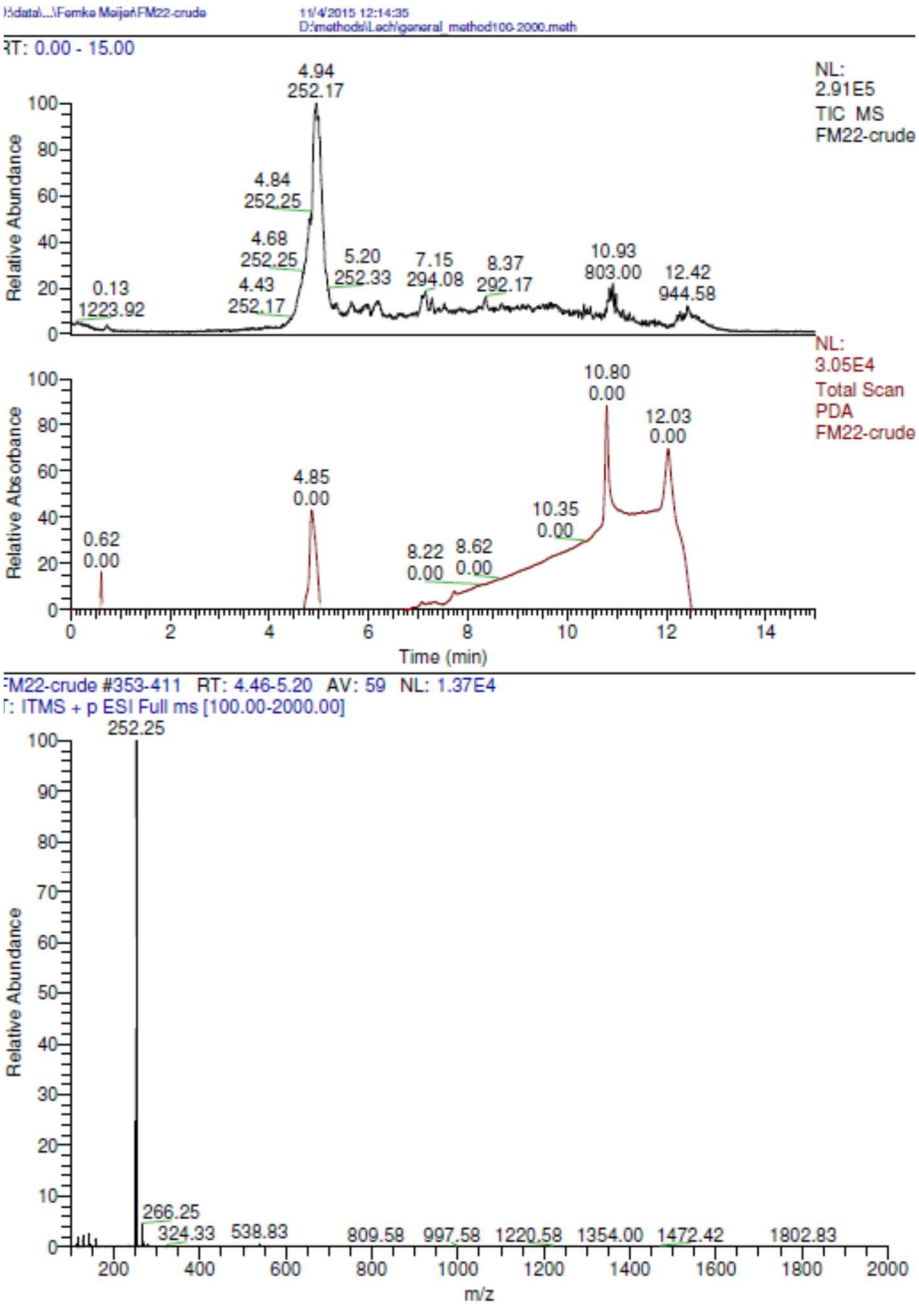

Figure S79. ^{1}H NMR of of benzhydryl pyrrolidine derivative 2.6b.

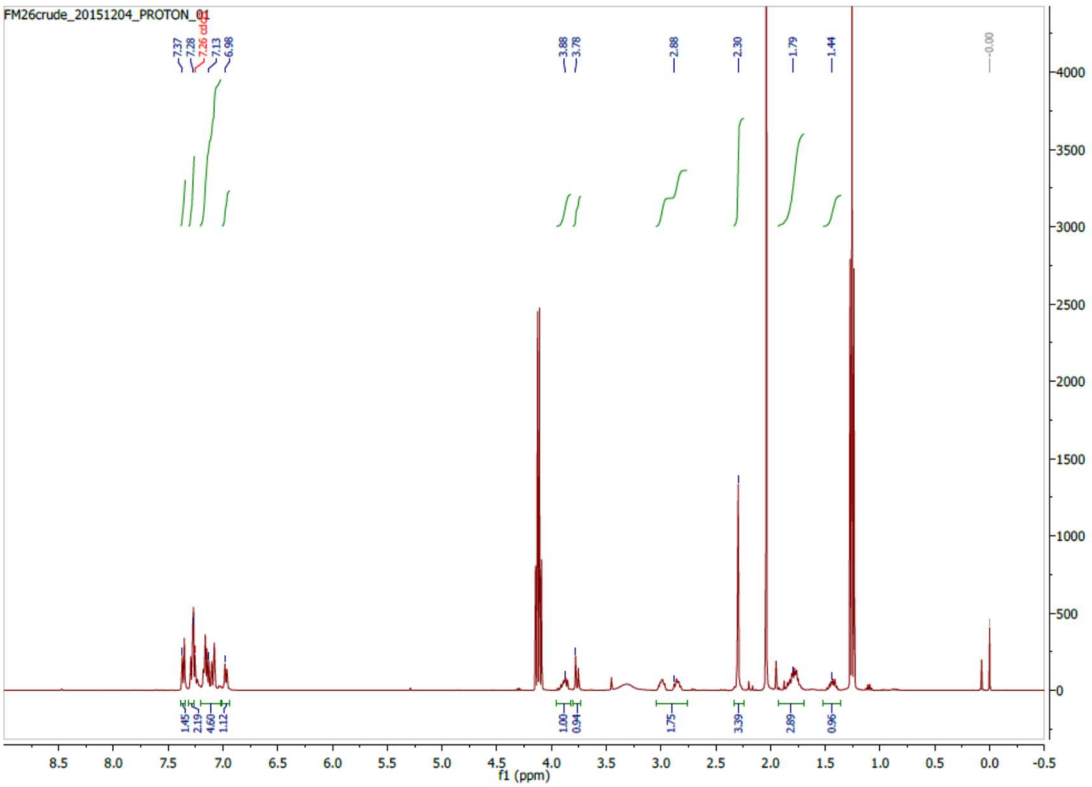

Figure S80. ^{13}C NMR of of benzhydryl pyrrolidine derivative 2.6b.

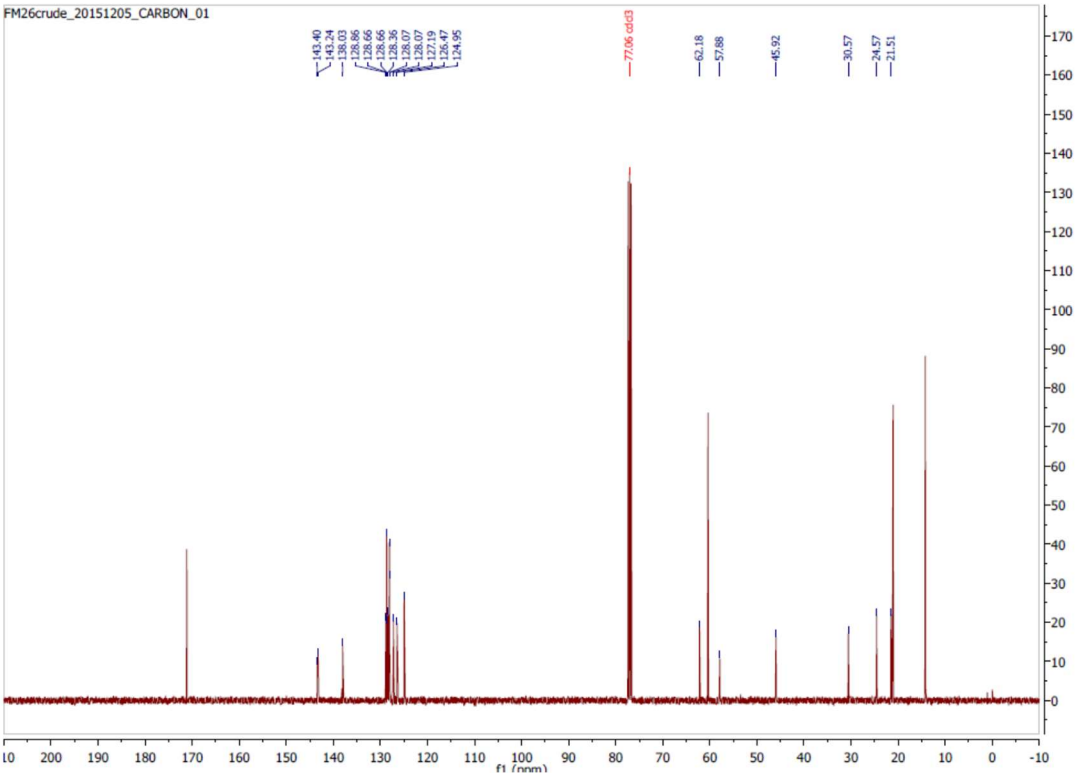

Figure S81. LC-MS of of benzhydryl pyrrolidine derivative 2.6b.

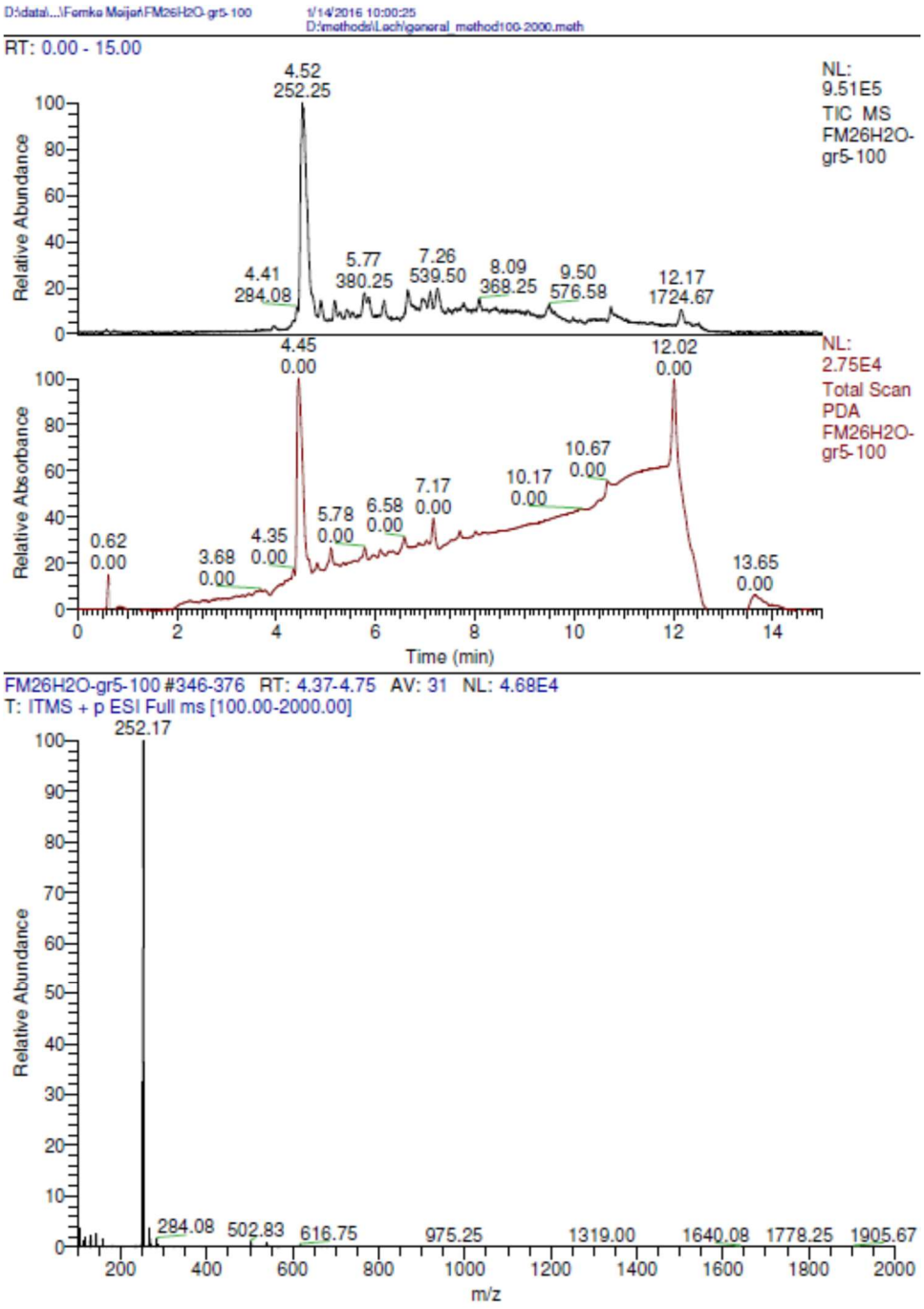

Figure S82. ^{1}H NMR of benzhydryl pyrrolidine derivative 2.6c-I.

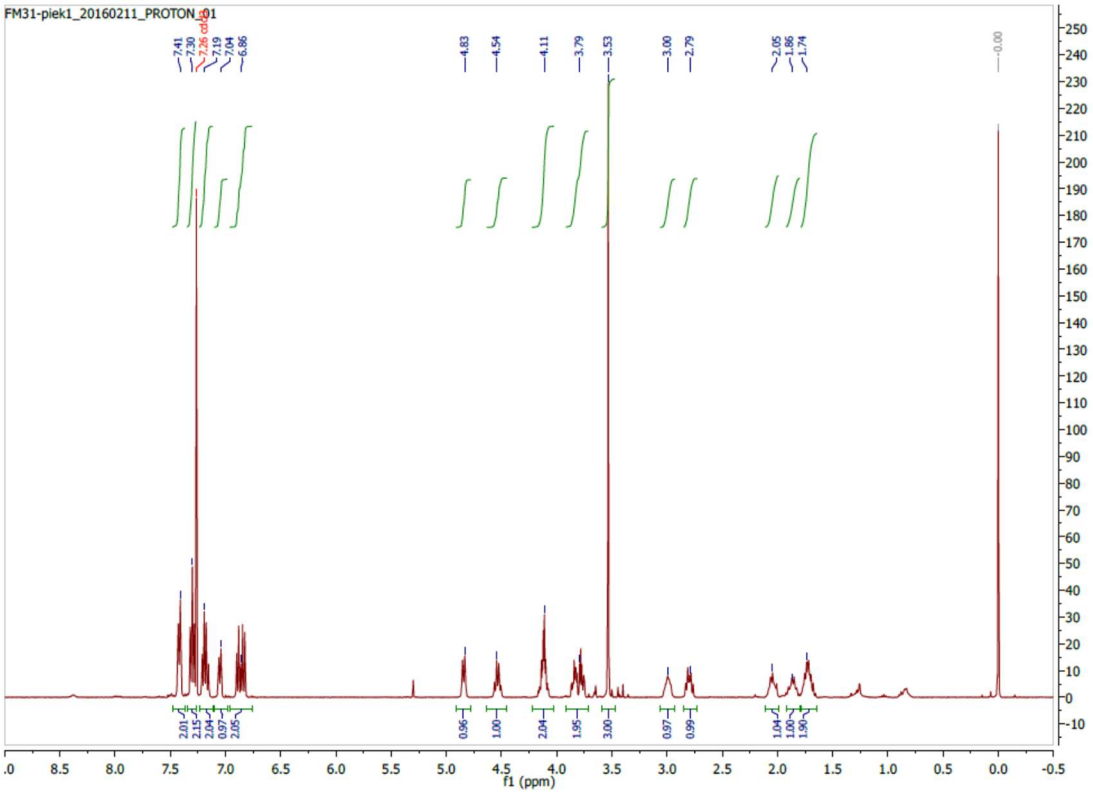

Figure S83. ^{13}C NMR of of benzhydryl pyrrolidine derivative 2.6c-I.

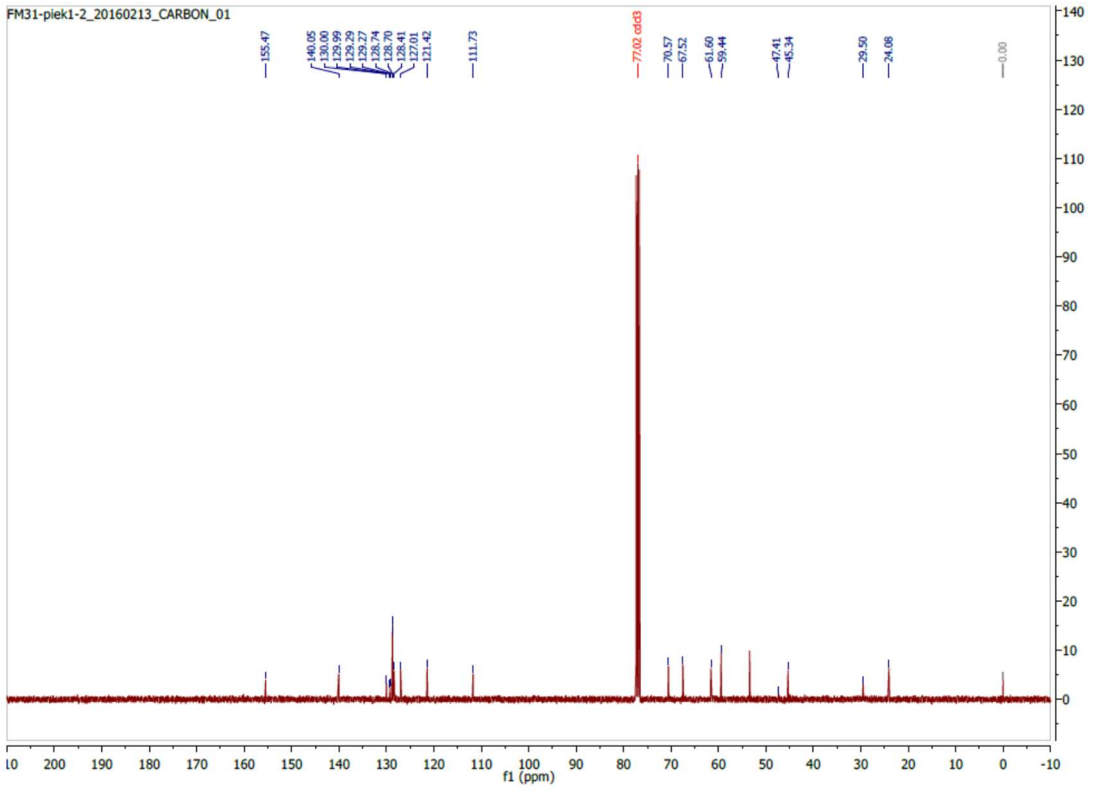

Figure S84. LC-MS of of benzhydryl pyrrolidine derivative 2.6c-I.

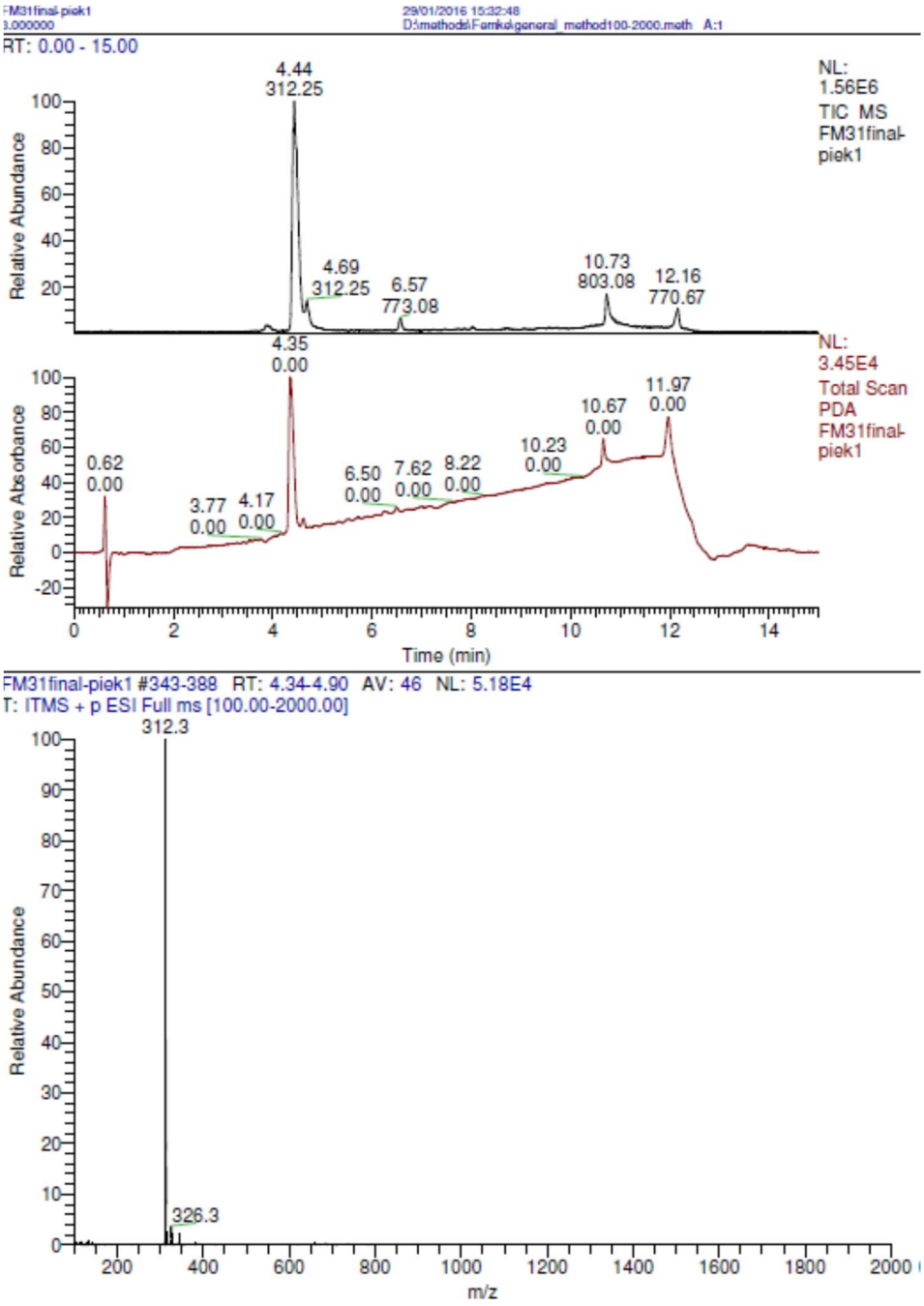

Figure S85. ^{1}H NMR of benzhydryl pyrrolidine derivative 2.6c-II.

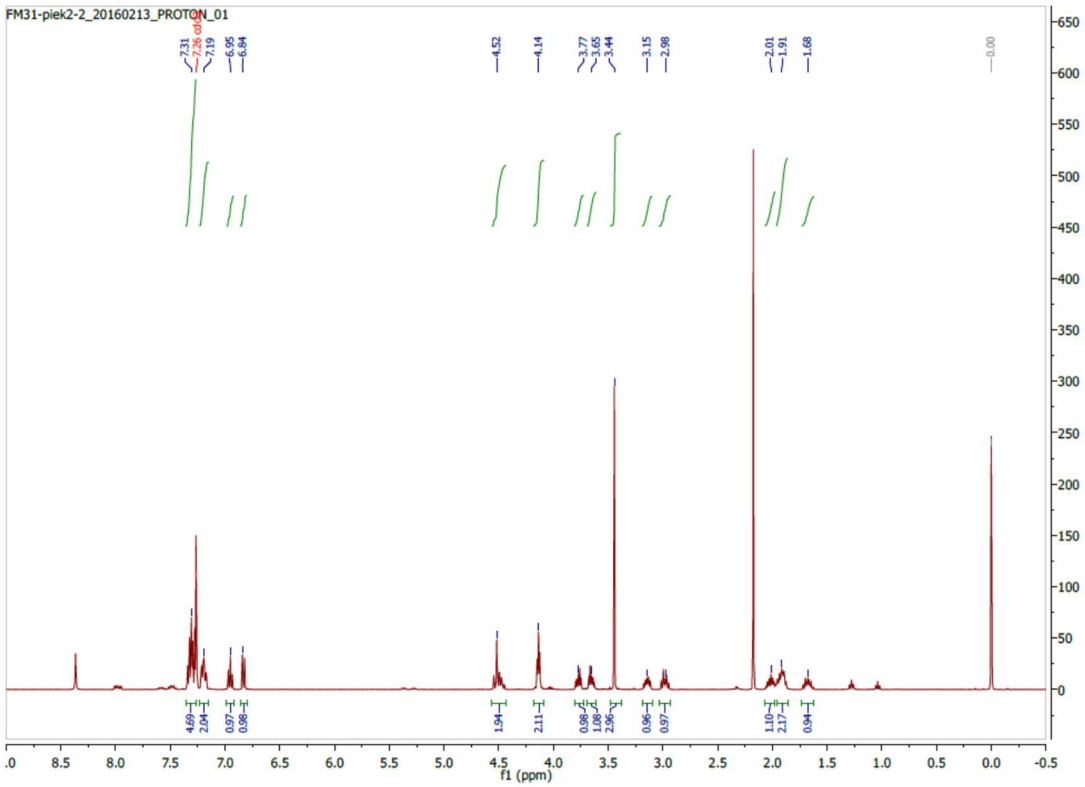

Figure S86. ^{13}C NMR of benzhydryl pyrrolidine derivative 2.6c-II.

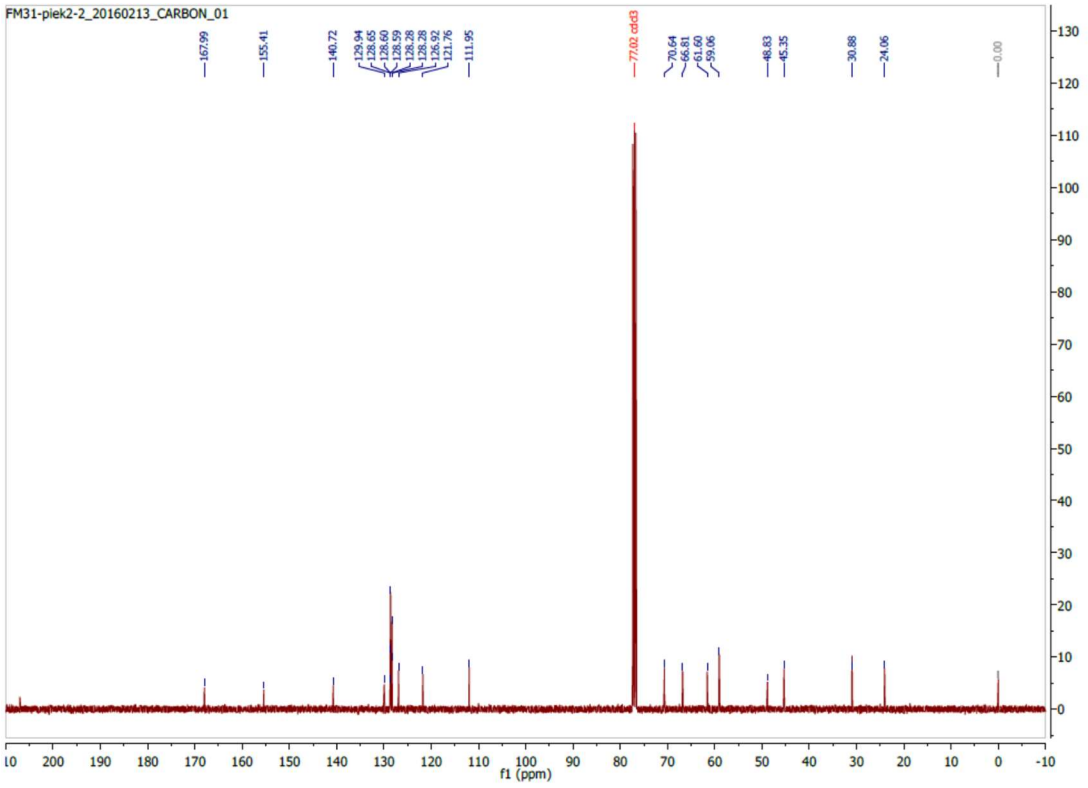

Figure S87. LC-MS benzhydryl pyrrolidine derivative 2.6c-II.

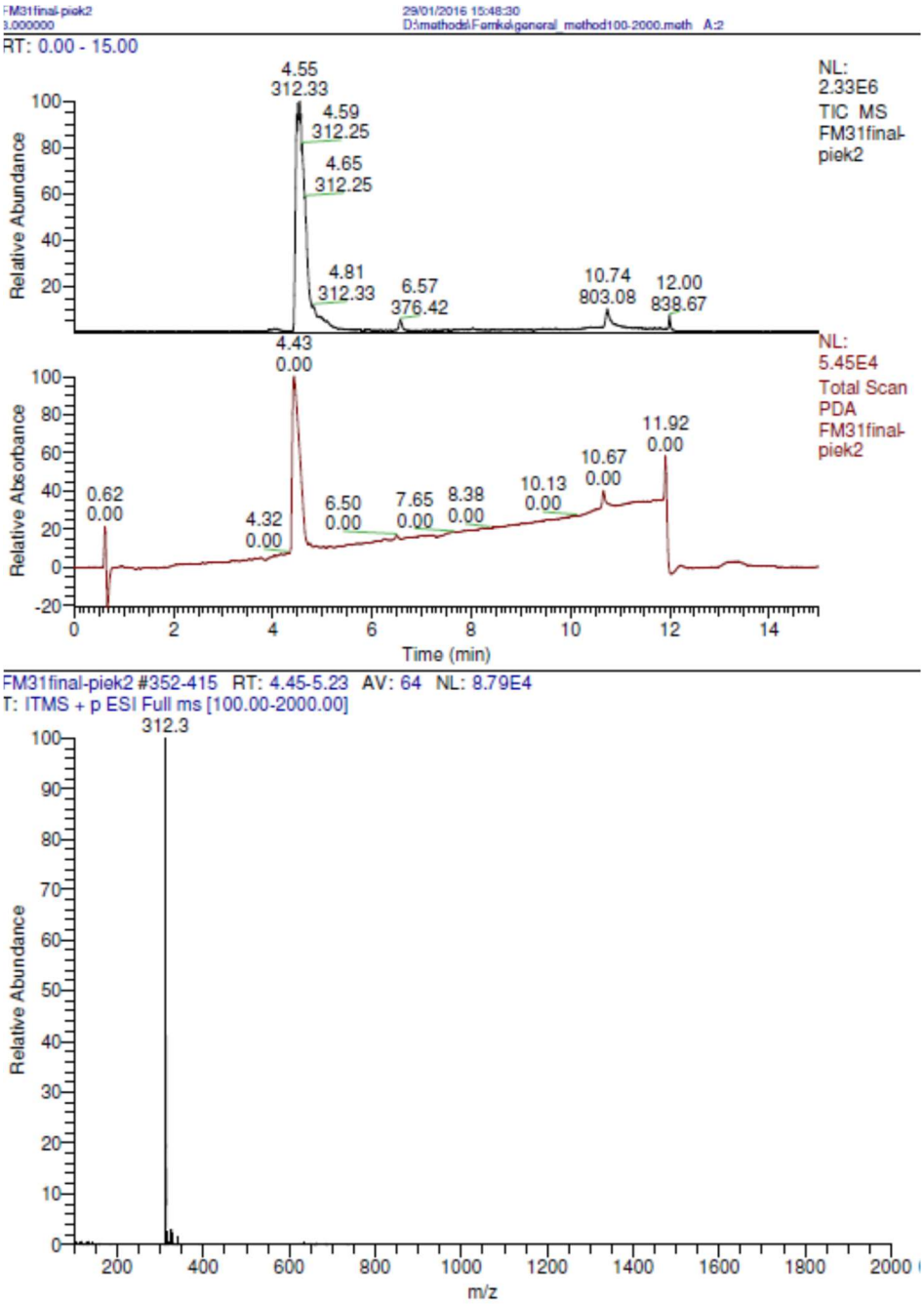

Figure S88. ^{1}H NMR of benzhydryl pyrrolidine derivative 2.6d-I.

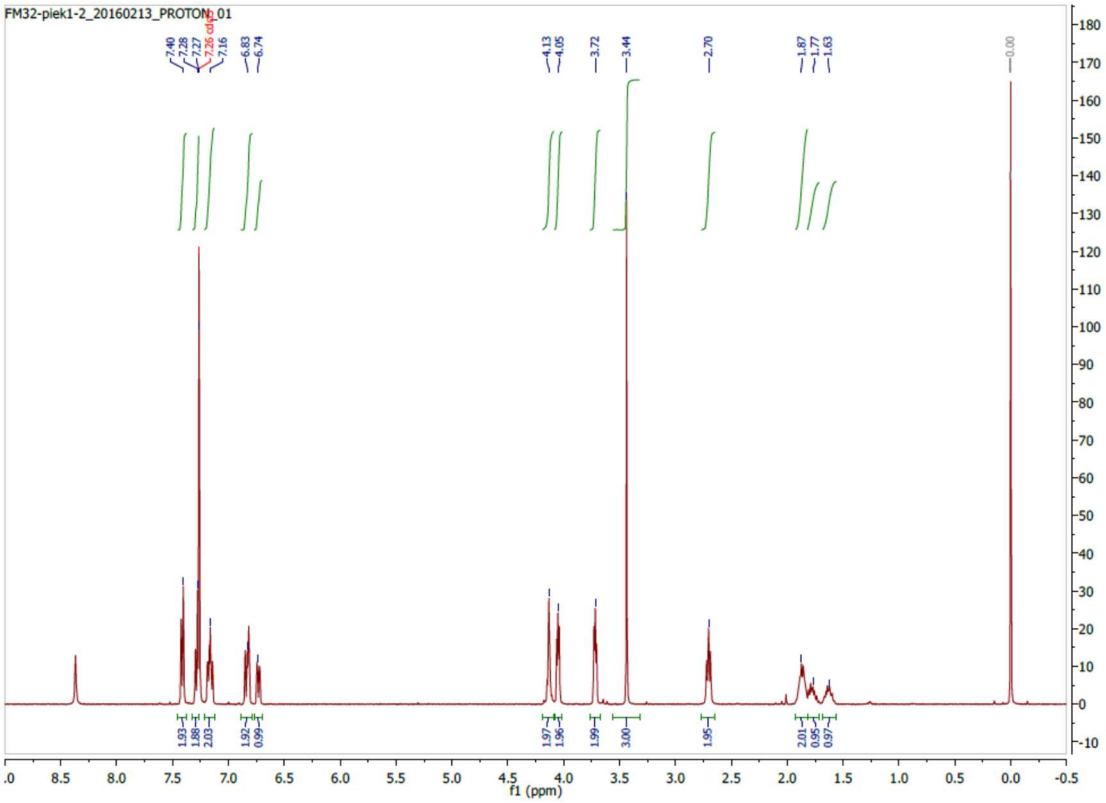

Figure S89. ^{13}C NMR of benzhydryl pyrrolidine derivative 2.6d-I.

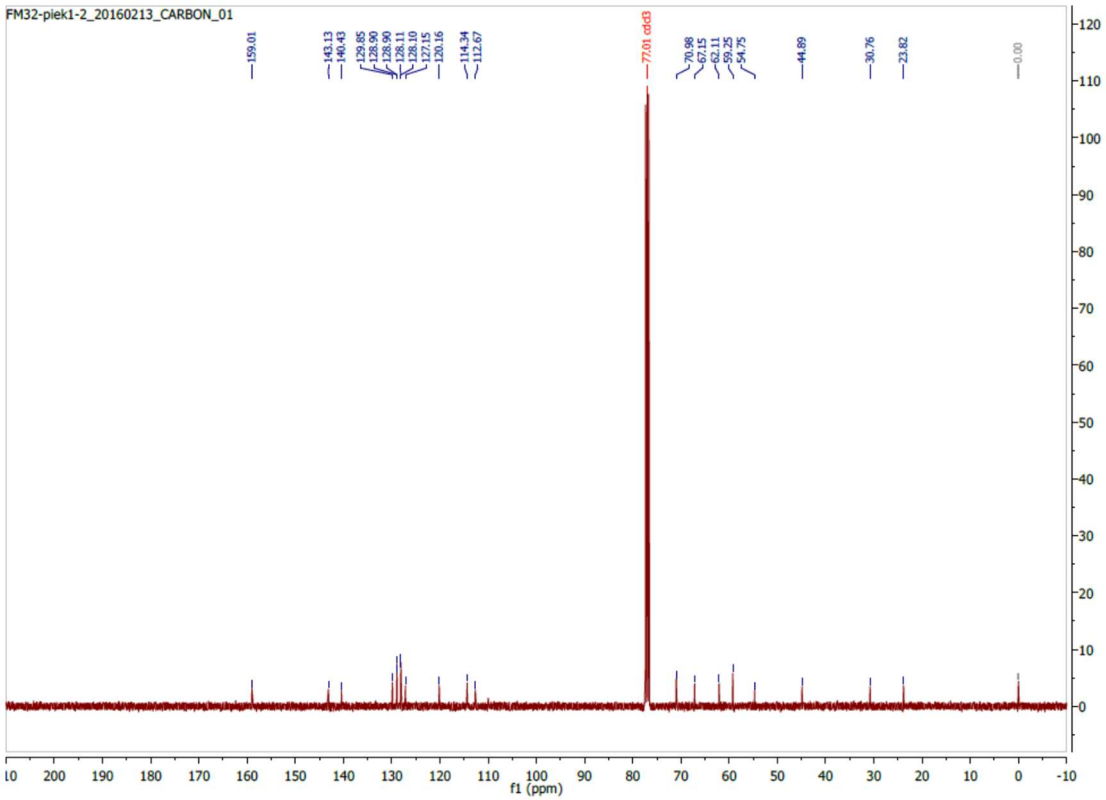

Figure S90. LC-MS of benzhydryl pyrrolidine derivative 2.6d-I.

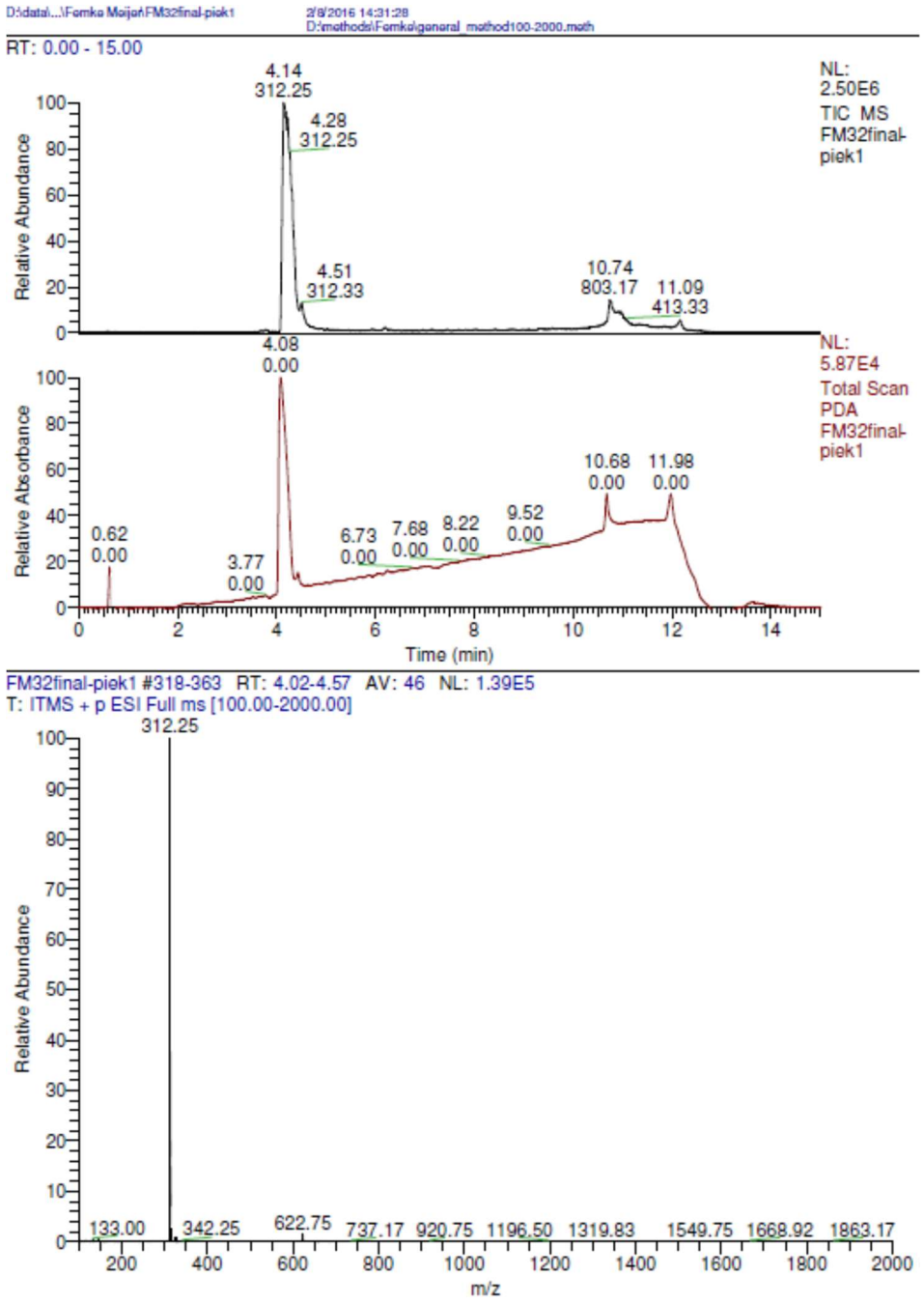

Figure S91. ^{1}H NMR of benzhydryl pyrrolidine derivative 2.6d-II.

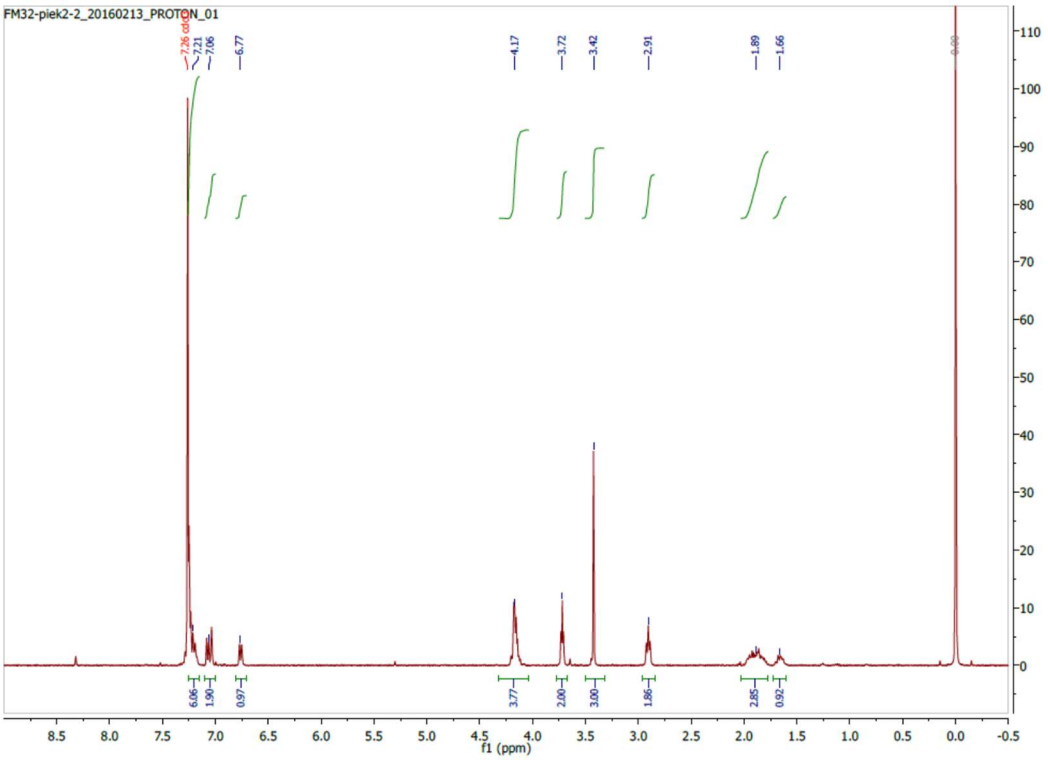

Figure S92. ^{13}C NMR of benzhydryl pyrrolidine derivative 2.6d-II.

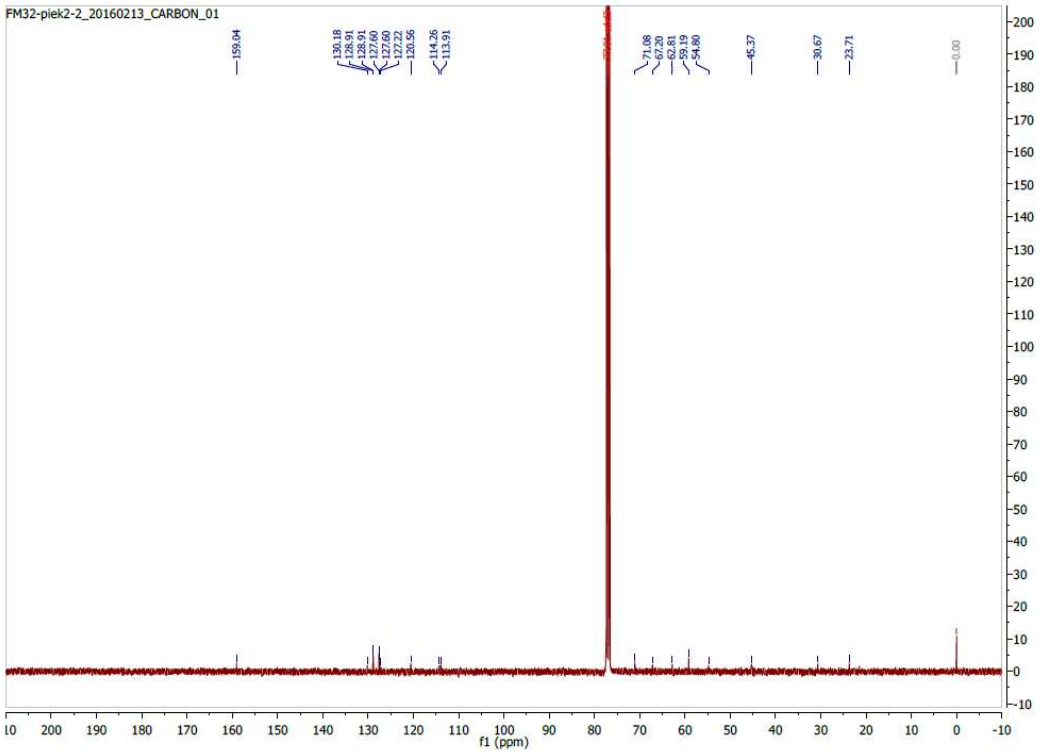

Figure S93. LC-MS of of benzhydryl pyrrolidine derivative 2.6d-II.

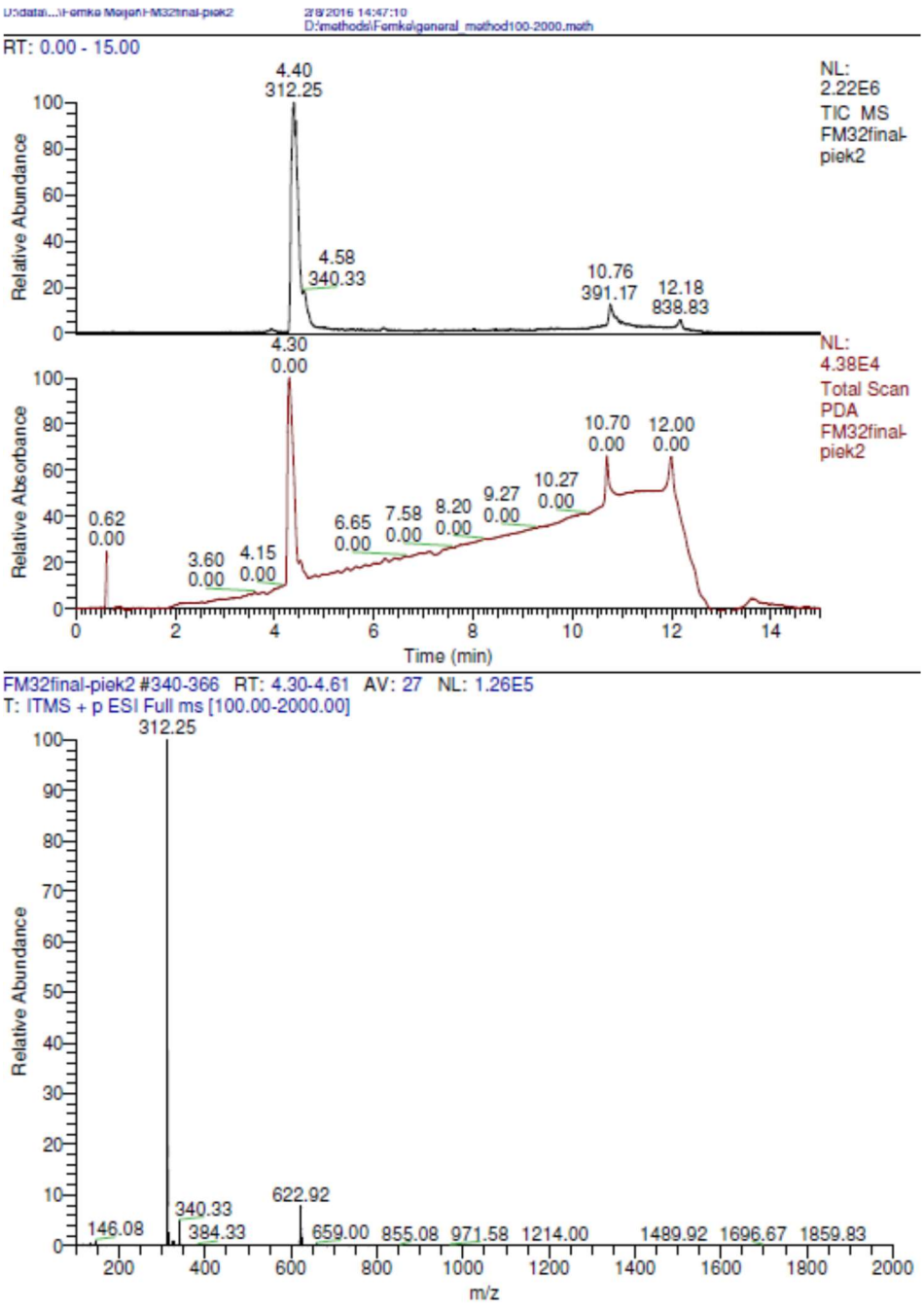

Figure S94. ^{1}H NMR of benzhydryl pyrrolidine derivative 2.6e-I.

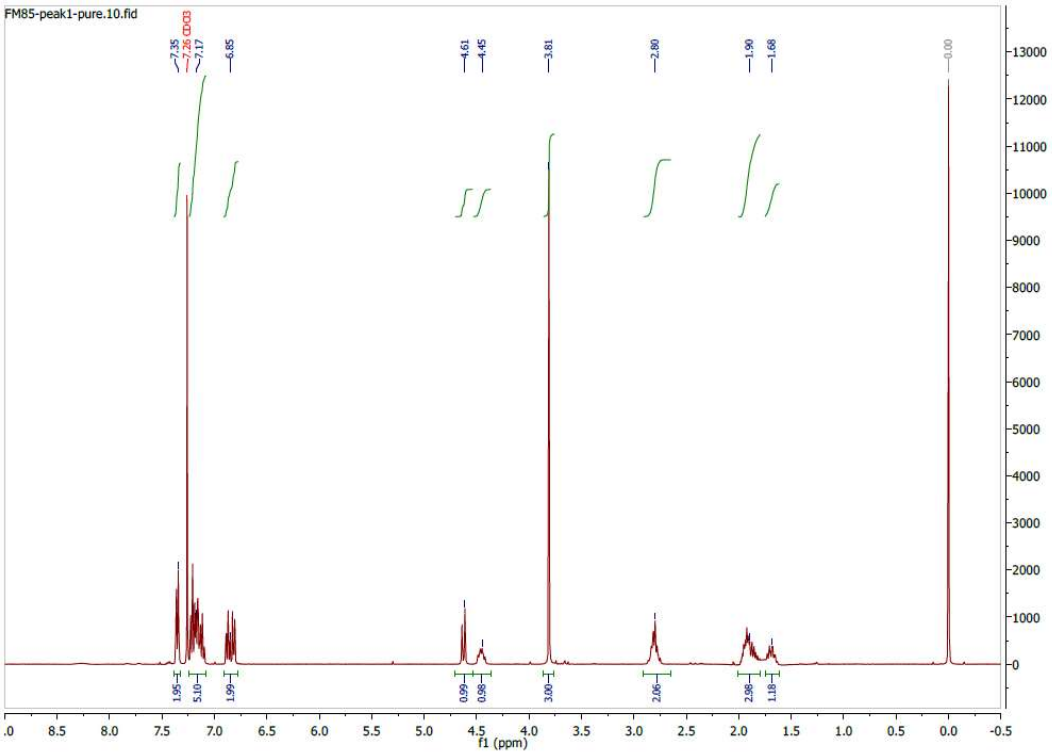

Figure S95. ^{13}C NMR of benzhydryl pyrrolidine derivative 2.6e-I.

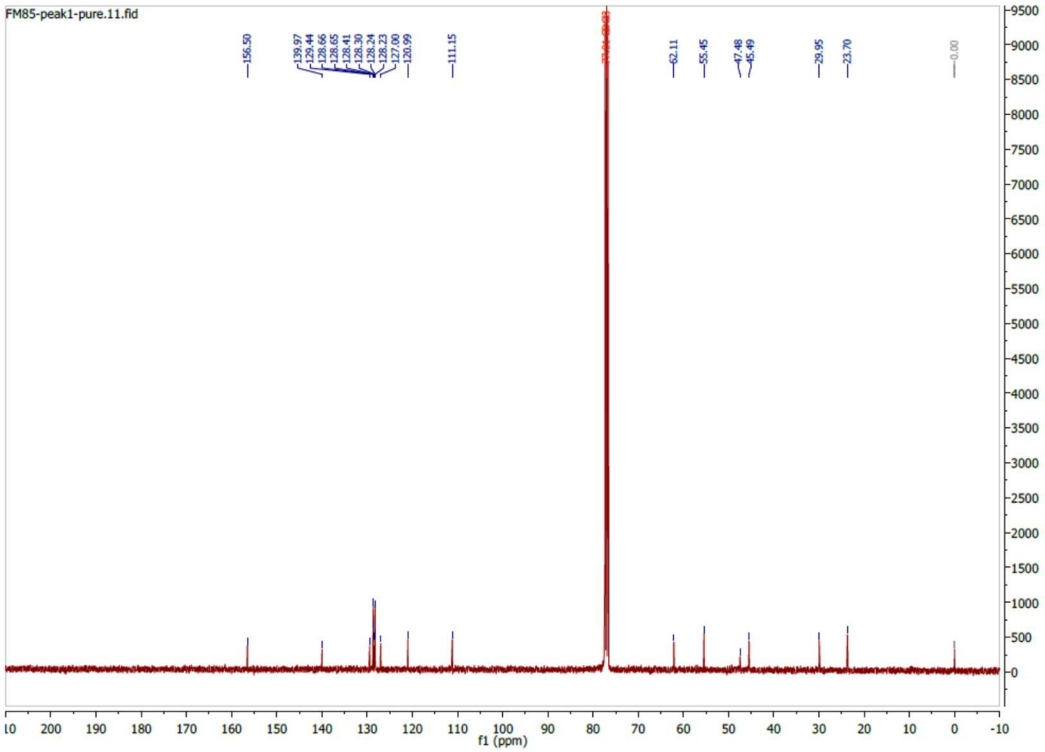

Figure S96. LC-MS of benzhydryl pyrrolidine derivative 2.6e-I.

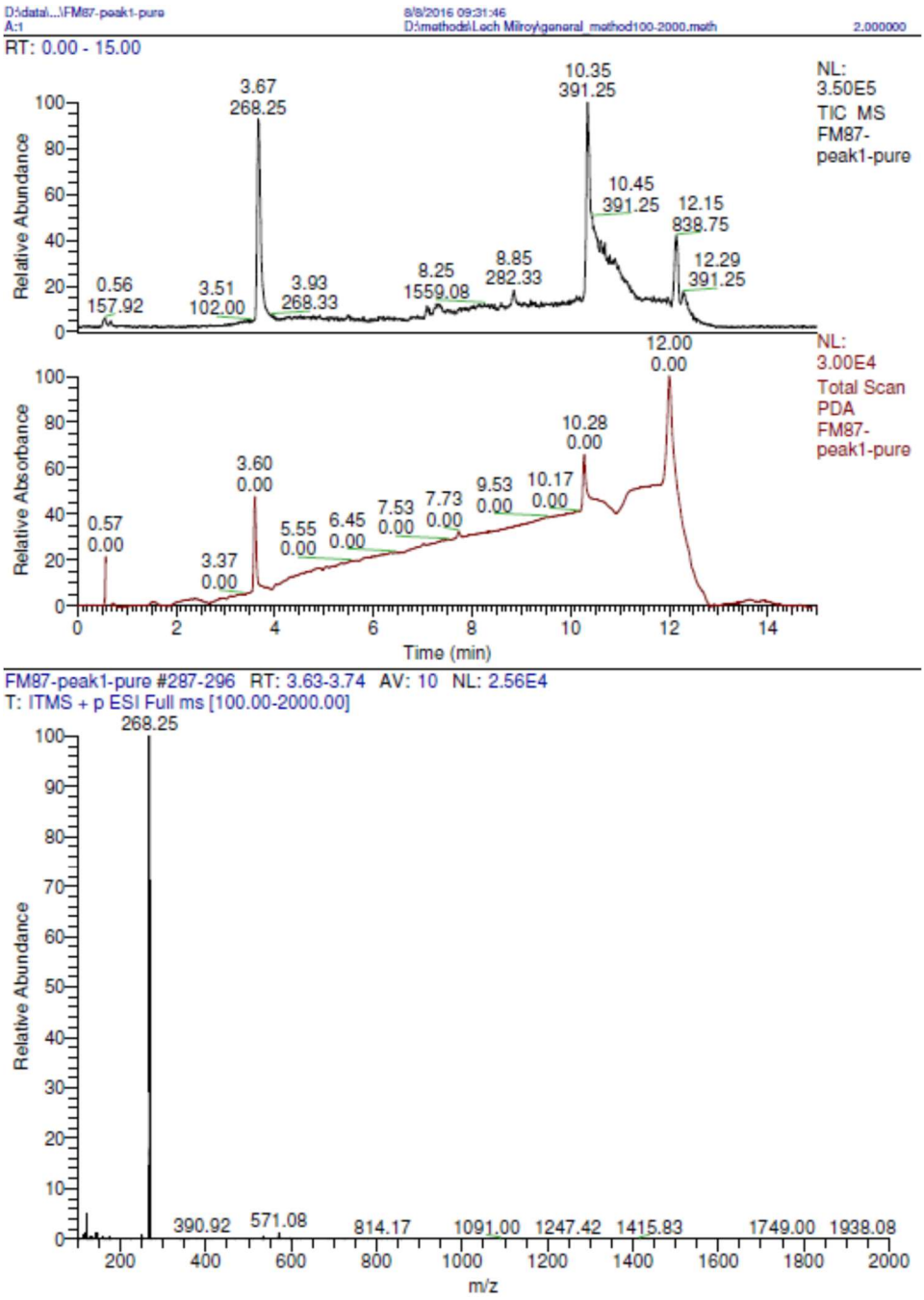

Figure S97. ^{1}H NMR of benzhydryl pyrrolidine derivative 2.6e-II.

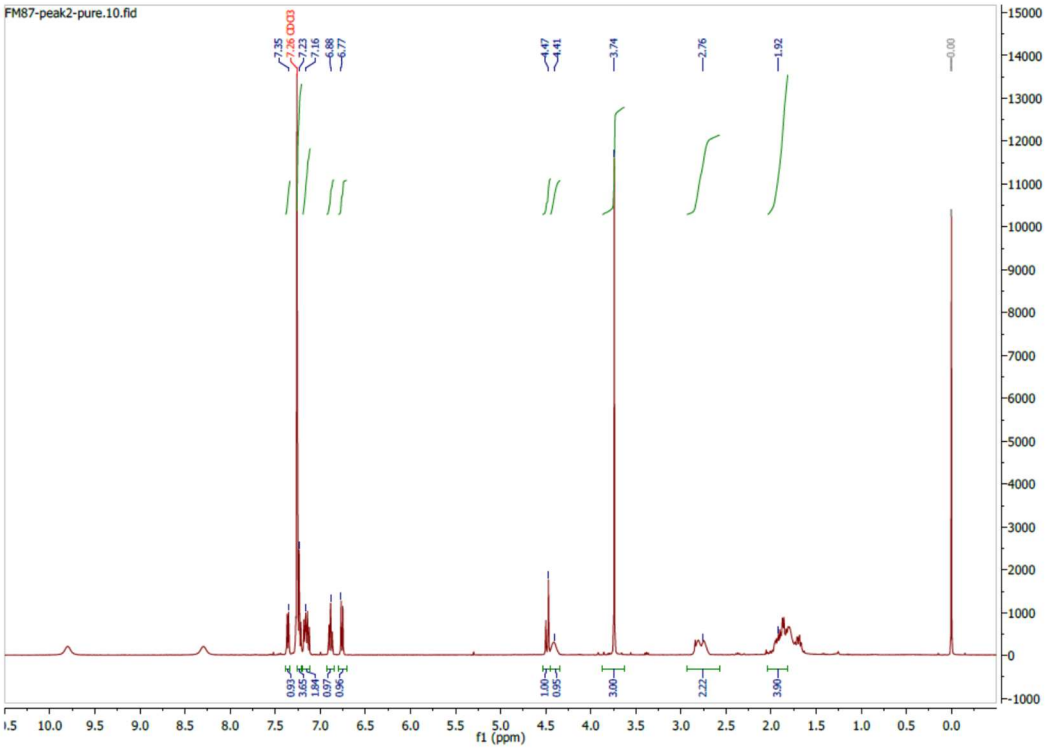

Figure S98. ^{13}C NMR of benzhydryl pyrrolidine derivative 2.6e-II.

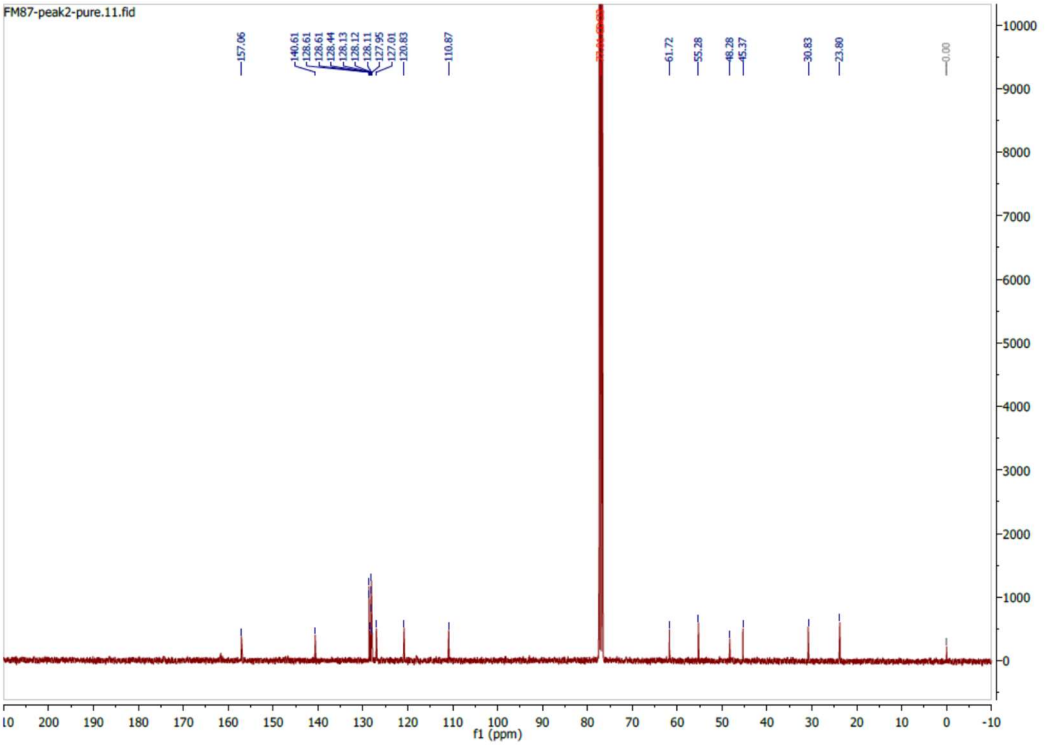

Figure S99. LC-MS of benzhydryl pyrrolidine derivative 2.6e-II.

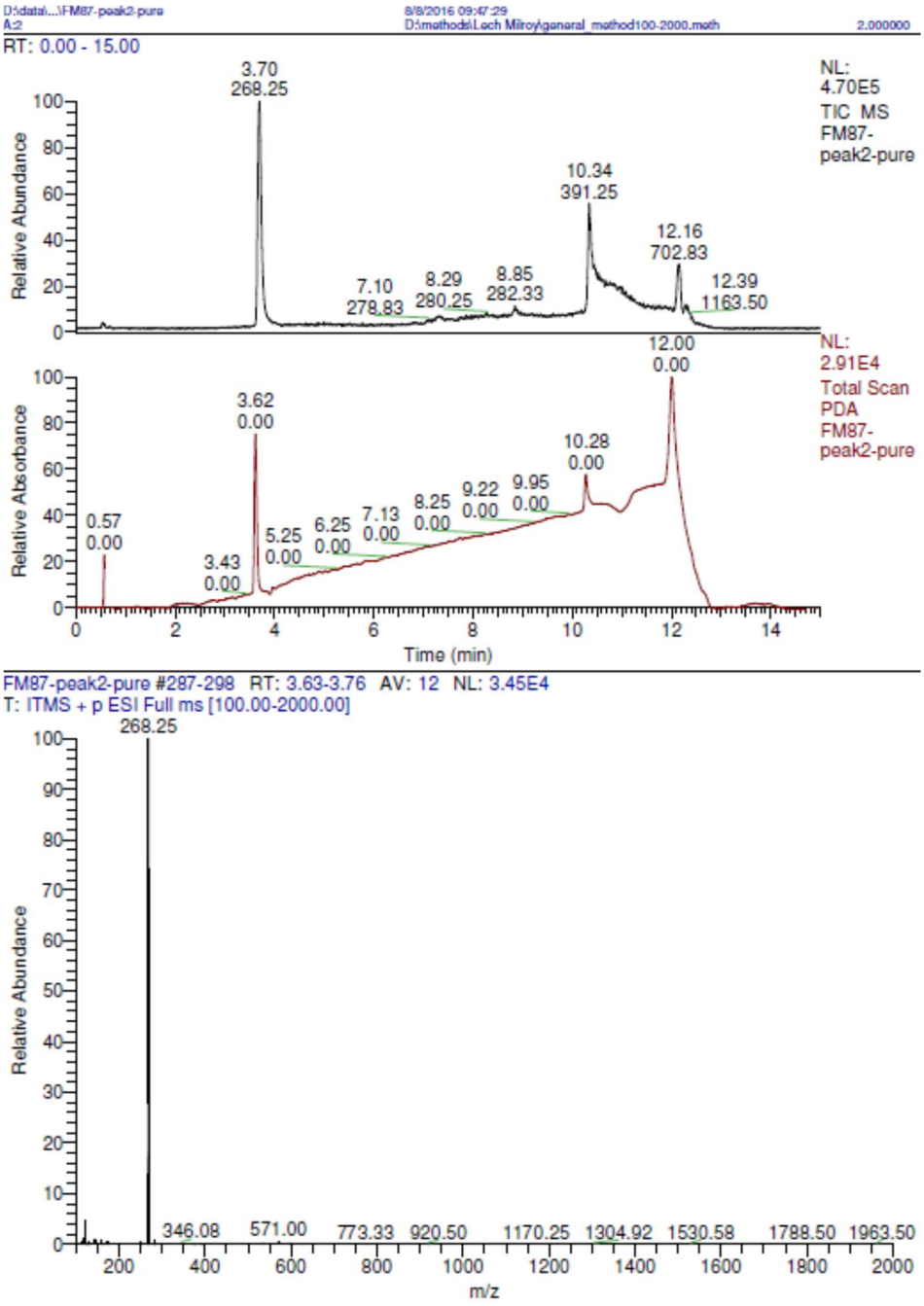

Figure S100. ^{1}H NMR of benzhydryl pyrrolidine derivative 2.6f-I.

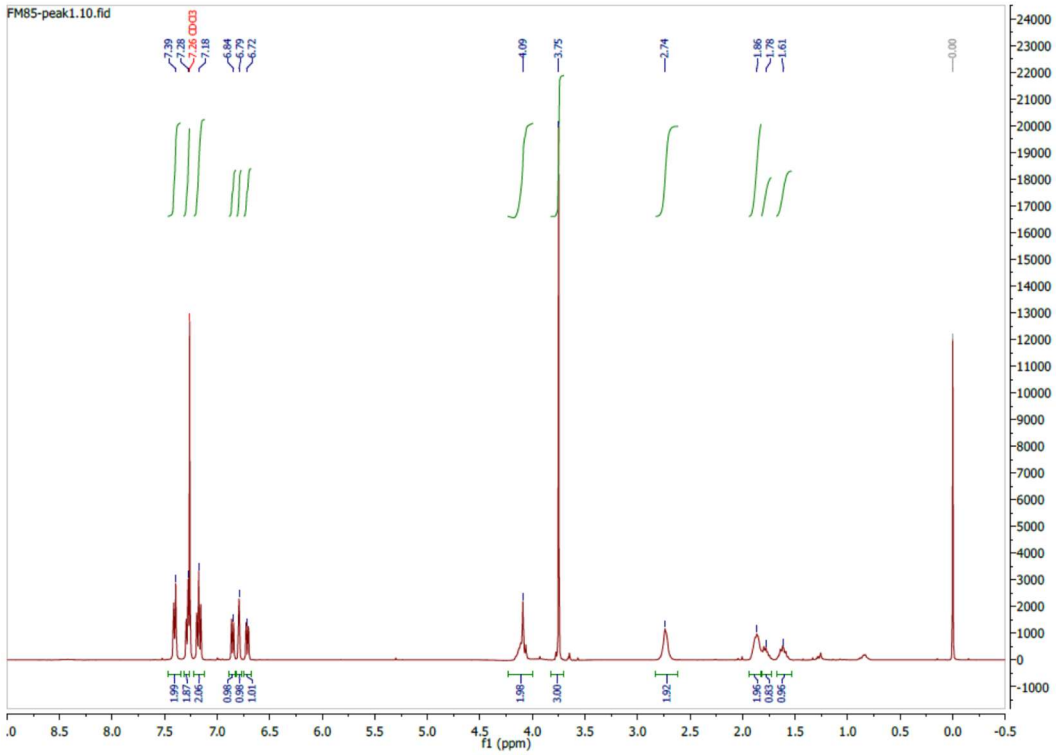

Figure S101. ^{13}C NMR of benzhydryl pyrrolidine derivative 2.6f-I.

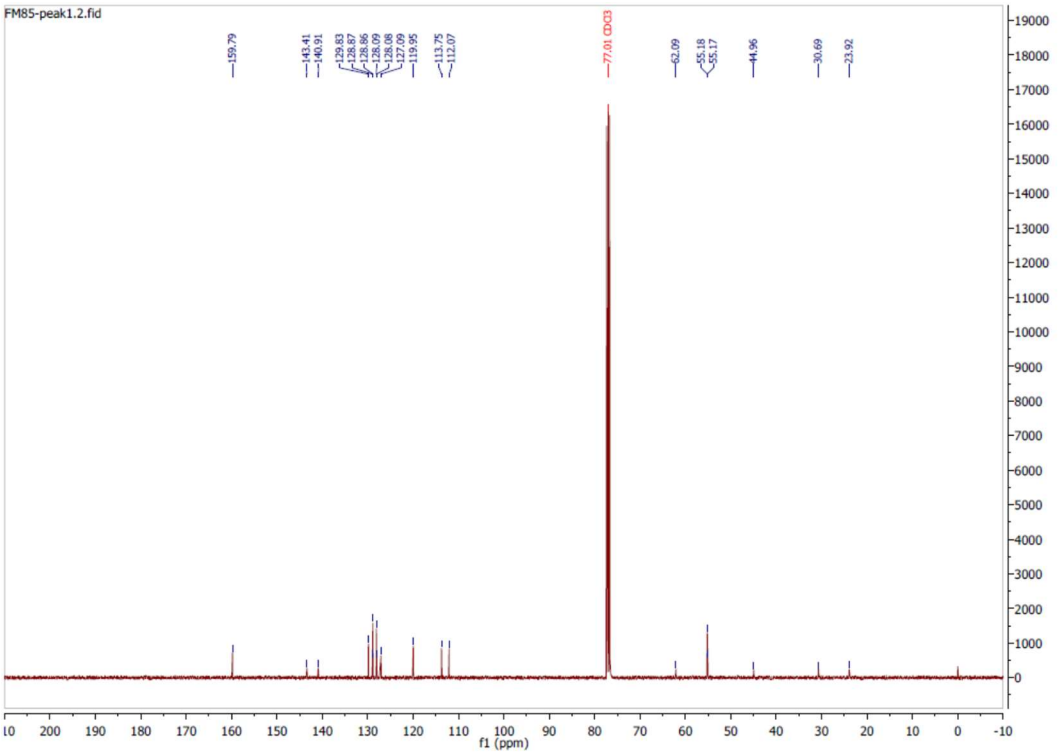

Figure S102. LC-MS of benzhydryl pyrrolidine derivative 2.6f-I.

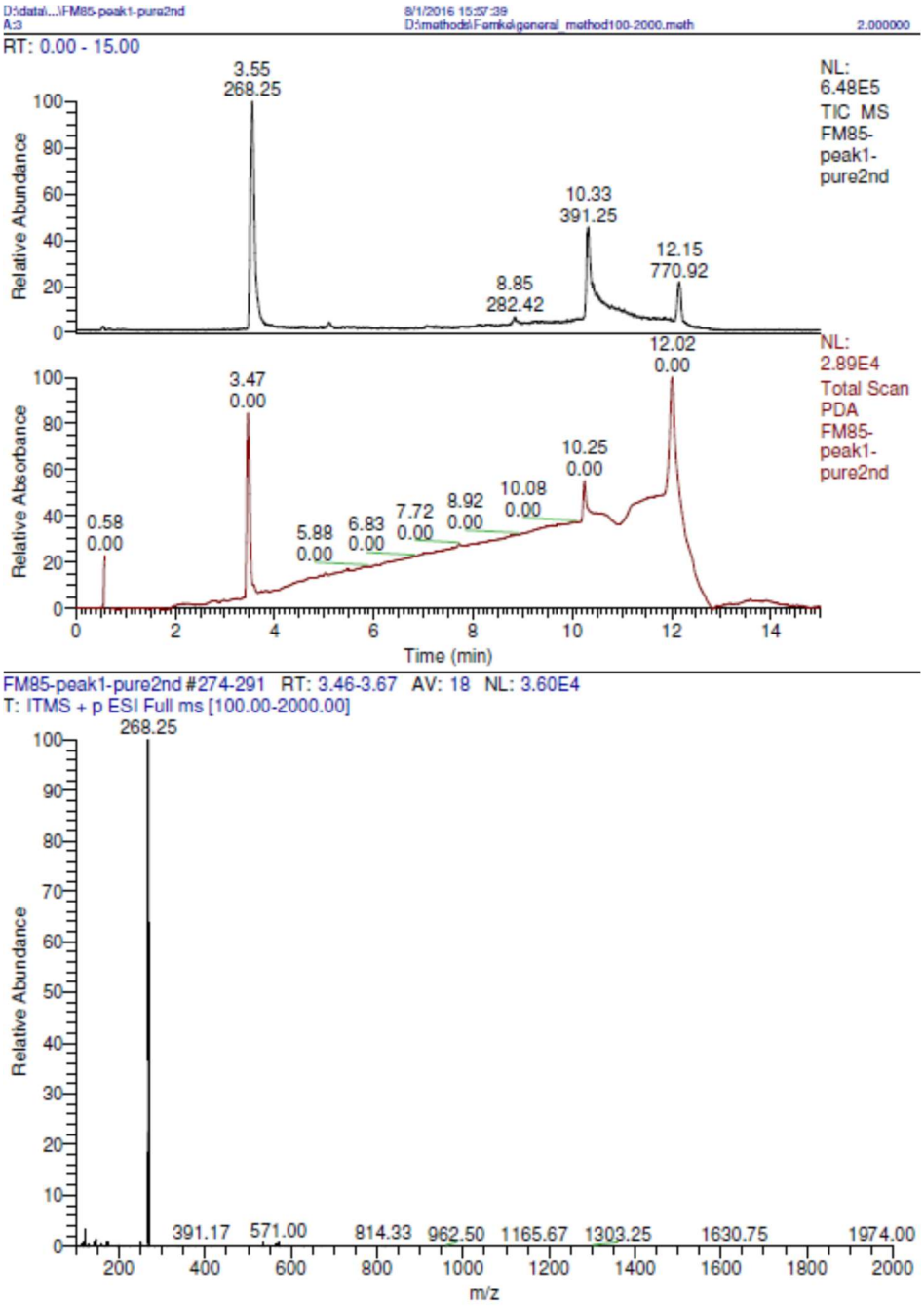

Figure S103. ^{1}H NMR of benzhydryl pyrrolidine derivative 2.6f-II.

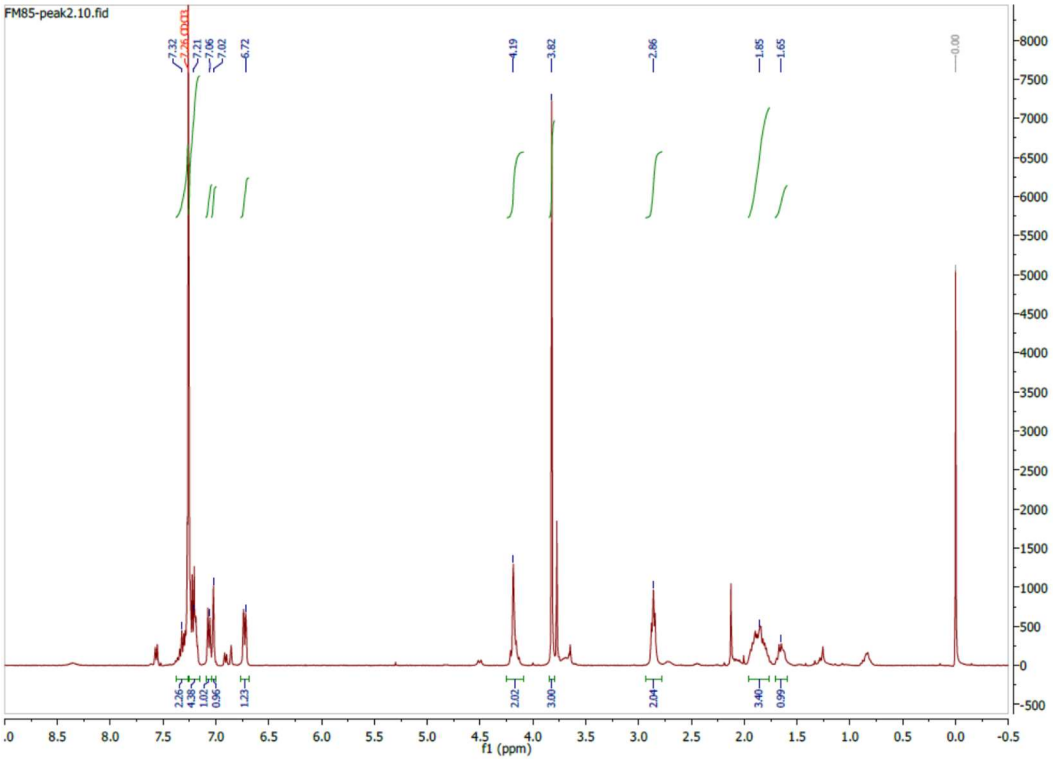

Figure S104. ^{13}C NMR of benzhydryl pyrrolidine derivative 2.6f-II.

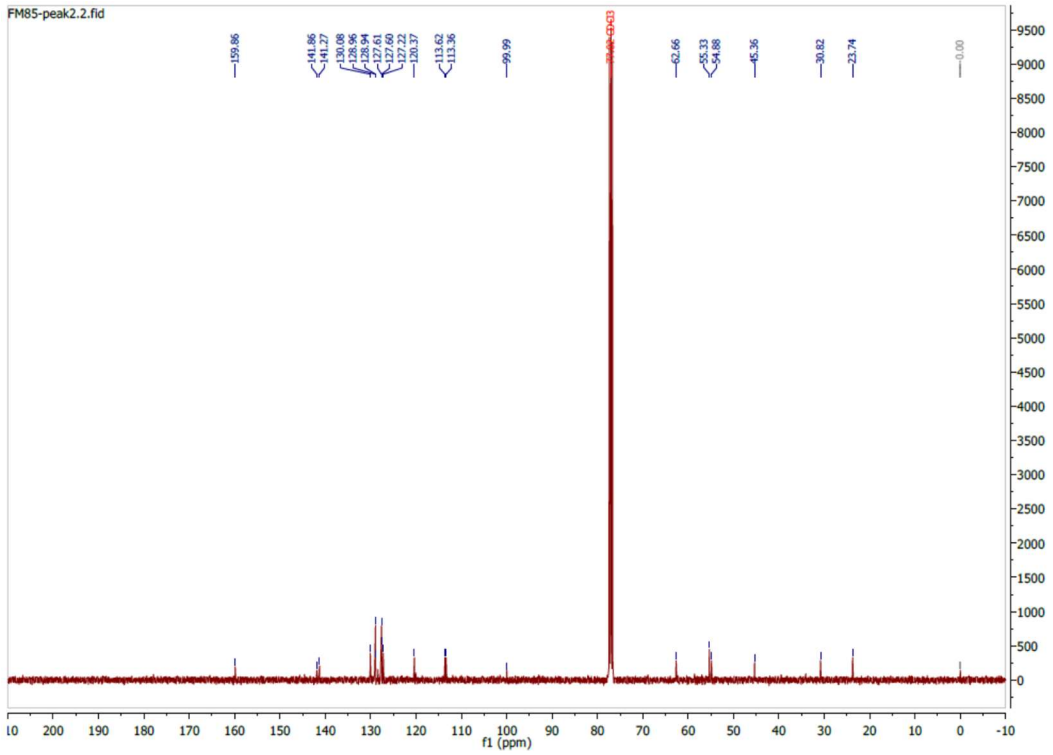

Figure S105. LC-MS of benzhydryl pyrrolidine derivative 2.6f-II.

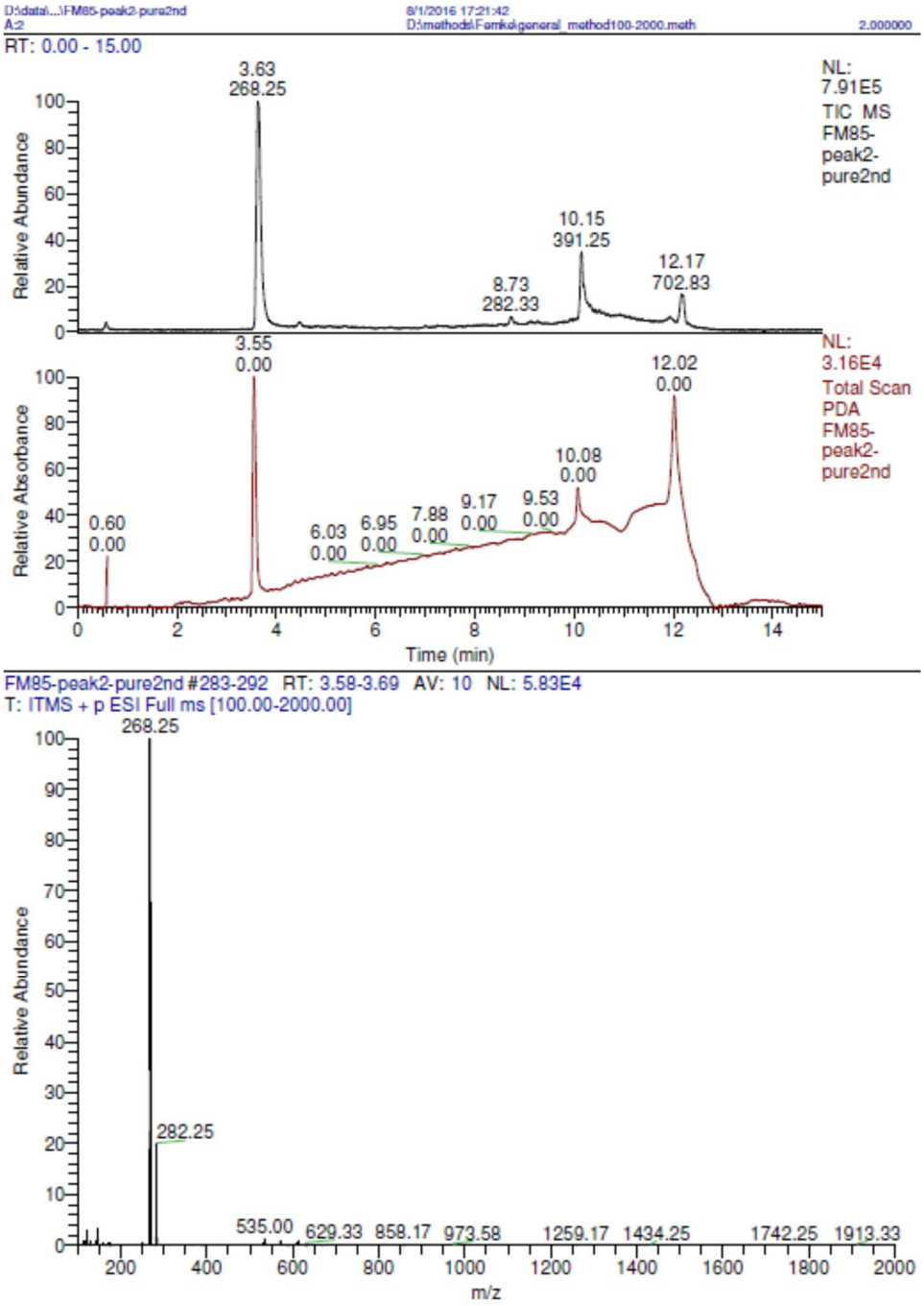

Figure S106. ^{1}H NMR of benzhydryl pyrrolidine derivative 2.6g.

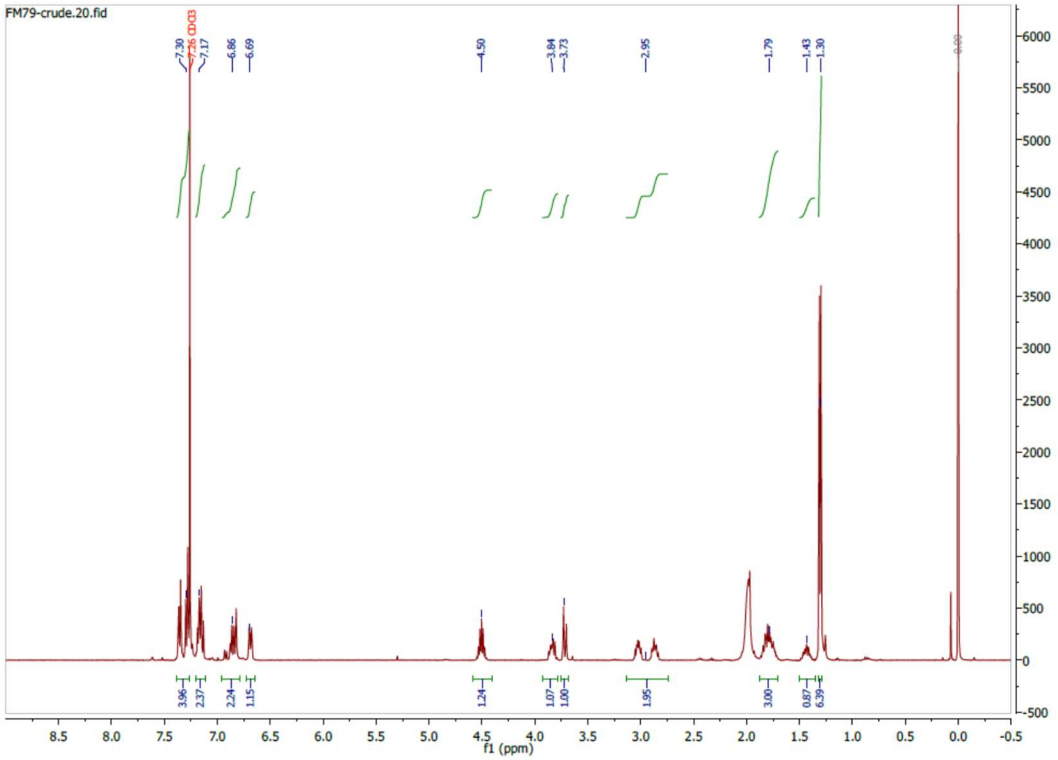

Figure S107. ^{13}C NMR of benzhydryl pyrrolidine derivative 2.6g.

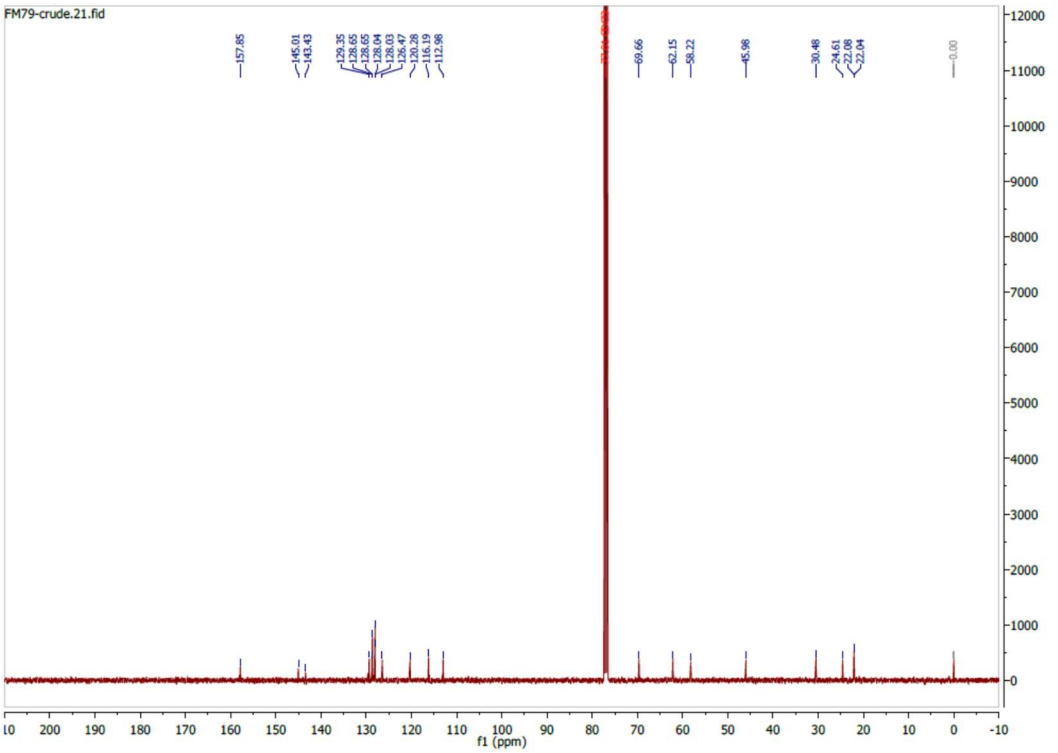

Figure S108. LC-MS of benzhydryl pyrrolidine derivative 2.6g.

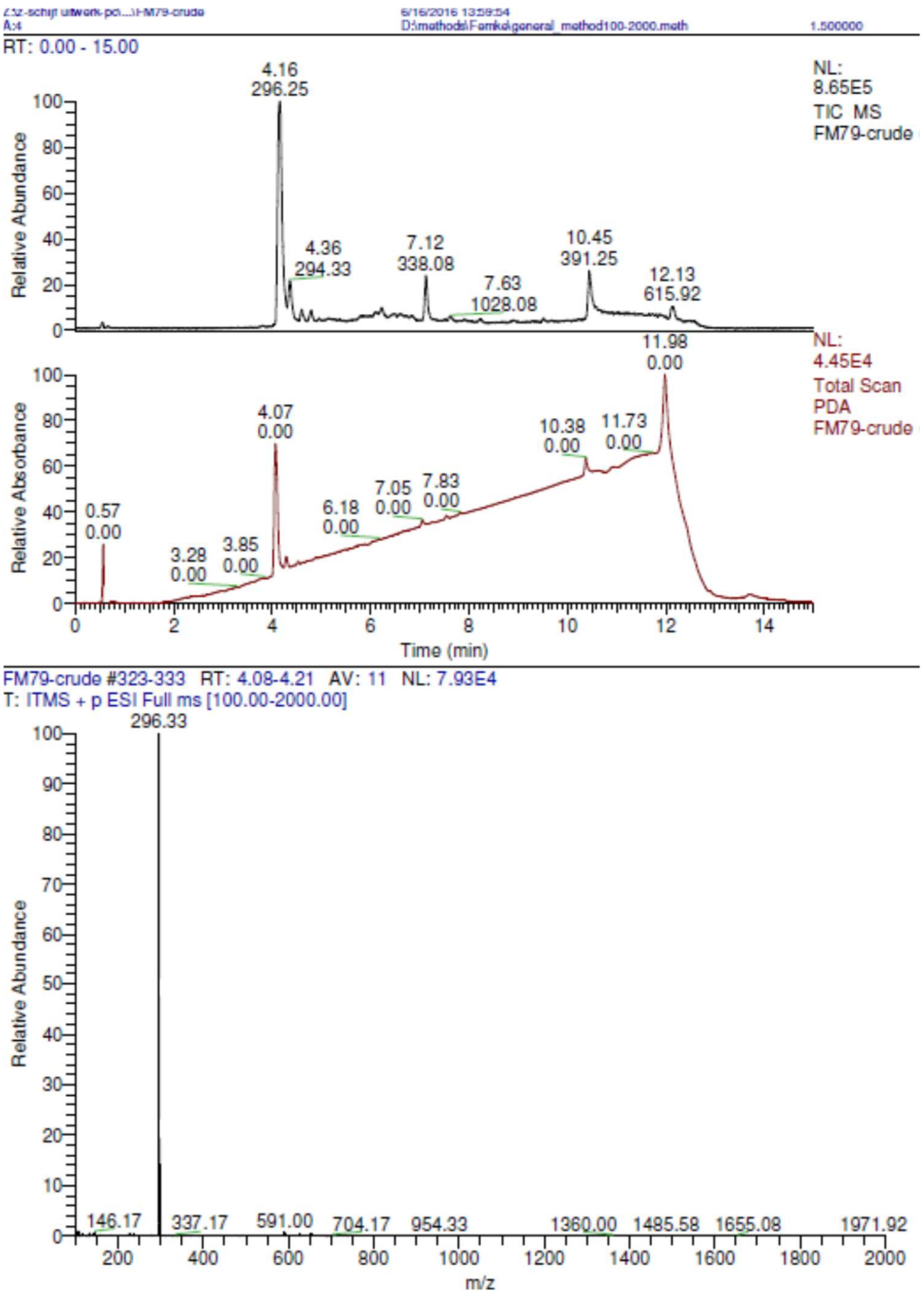

Figure S109. LC-MS of partially protected Tau peptide 3.1a.

LC-MS (ESI): calc. for $C_{63}H_{99}N_{11}O_{18}S_1P_1$ $[M+H]^+$ calculated = 1347.66, observed = 1347.58.

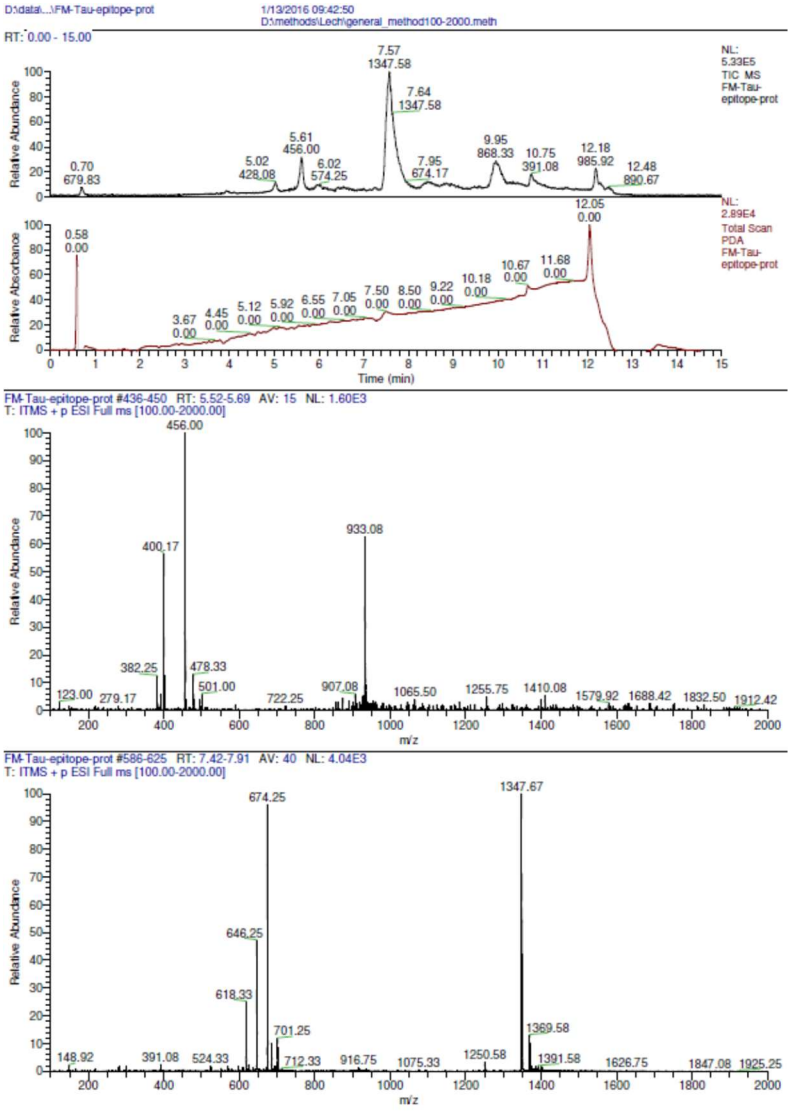

Figure S110. LC-MS (Method A) of partially protected Tau peptide 3.1b.

LC-MS (ESI): calc. for $C_{57}H_{87}N_{11}O_{17}S_1P_1$ $[M+H]^+$: 1247.57, observed 1247.67.

.

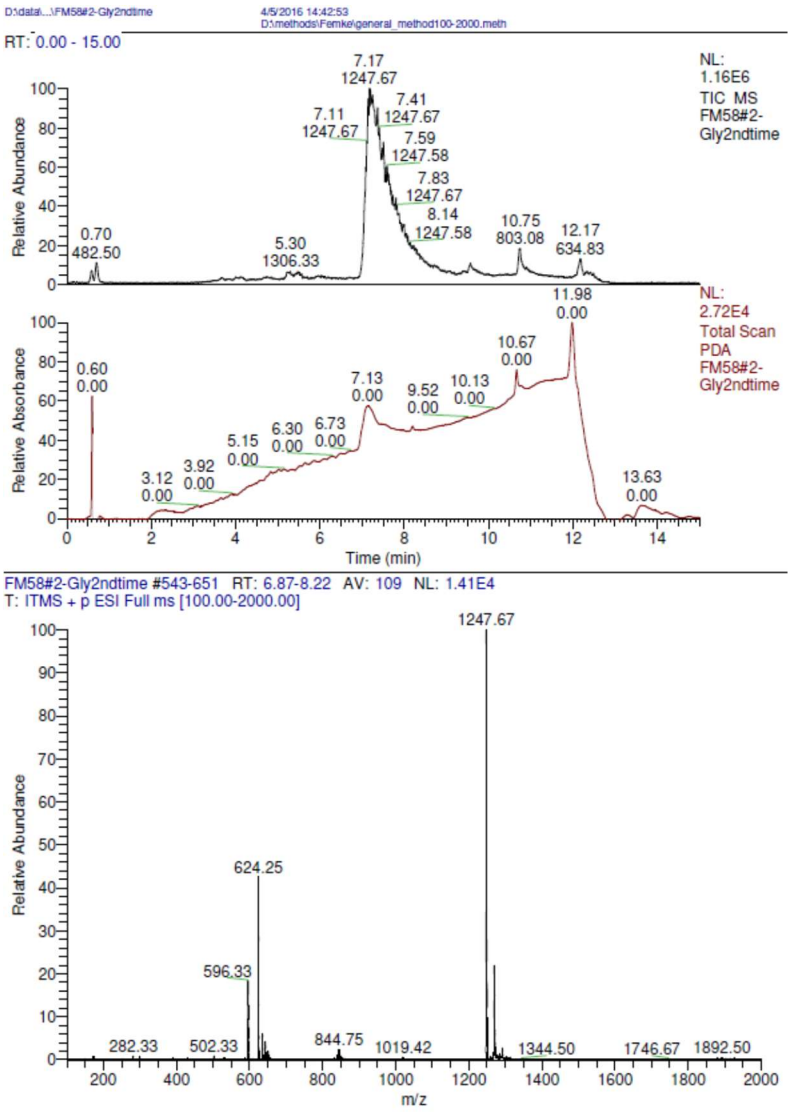

Figure S111. LC-MS (Method A) of partially protected Tau peptide 3.1c.

LC-MS (ESI): calc. for $C_{58}H_{89}N_{11}O_{17}S_1P_1$ $[M+H]^+$: 1261.59, observed 1261.75.

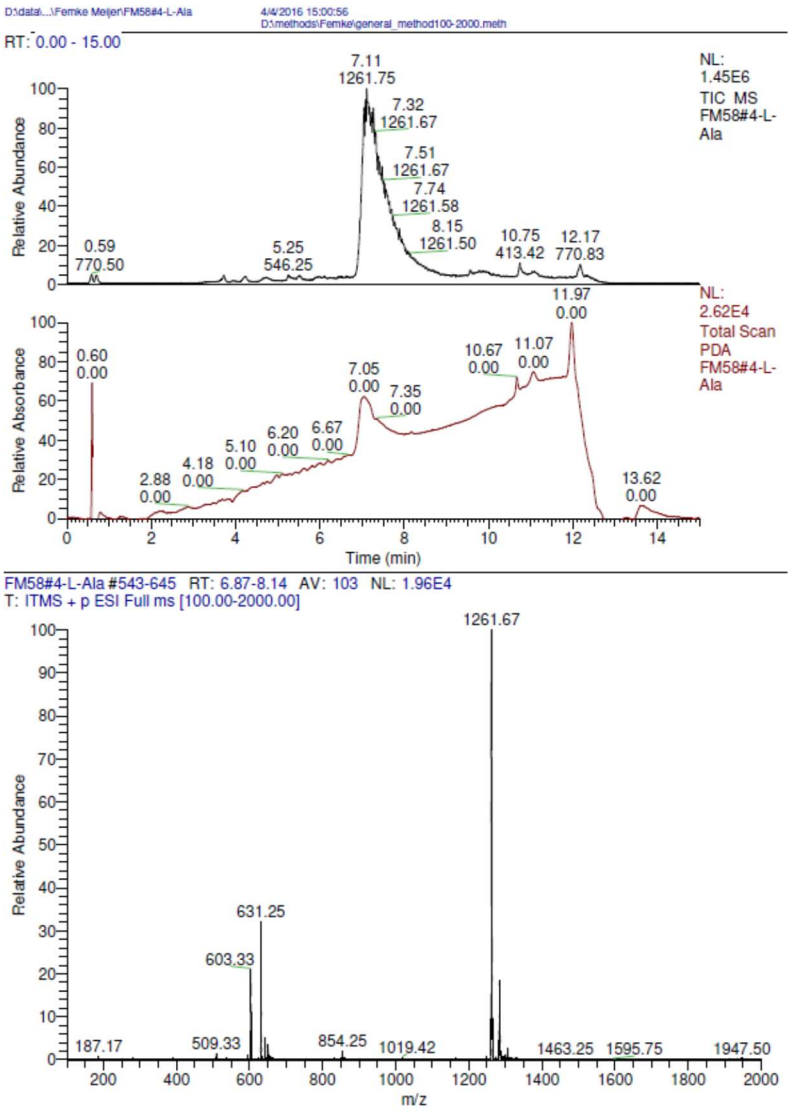

Figure S112. LC-MS (Method A) of partially protected Tau peptide 3.1d.

LC-MS (ESI): calc. for $C_{58}H_{89}N_{11}O_{17}S_1P_1$ $[M+H]^+$: 1261.59, observed 1261.67.

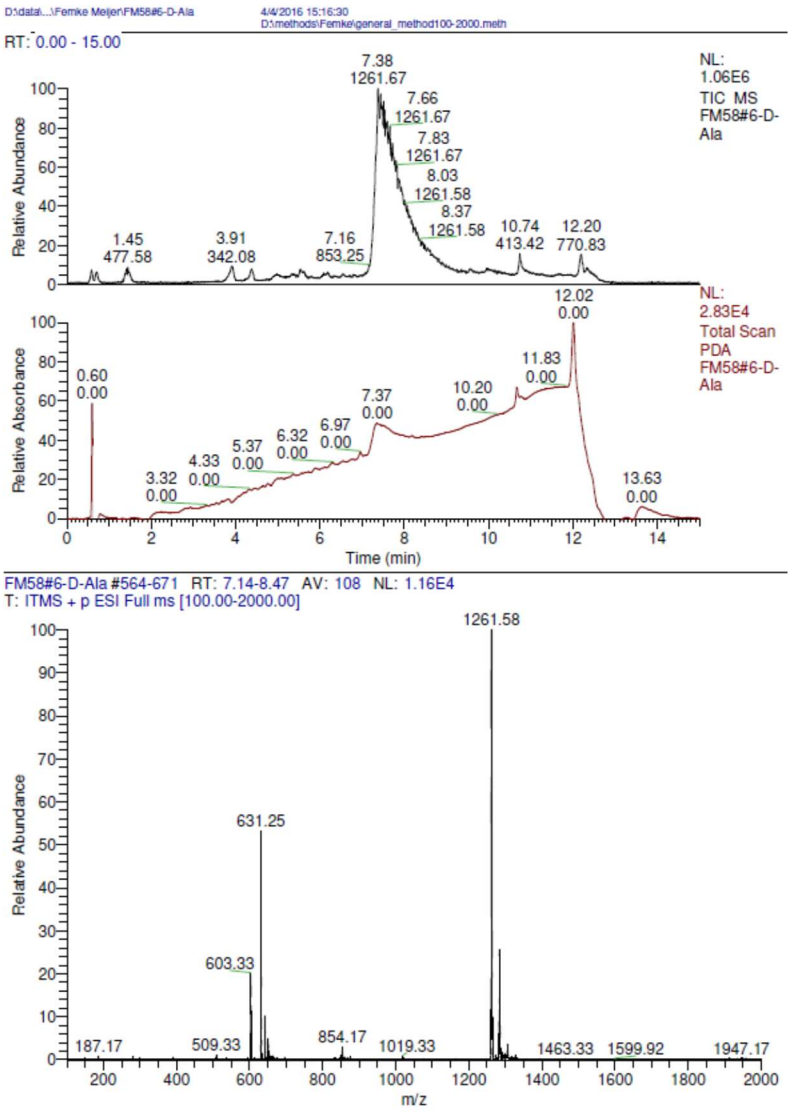

Figure S113. LC-MS (Method B) of partially protected Tau peptide 3.1e.

LC-MS (ESI): calc. for $C_{60}H_{93}N_{11}O_{17}S_1P_1$ $[M+H]^+$: 1289.62, observed 1289.50.

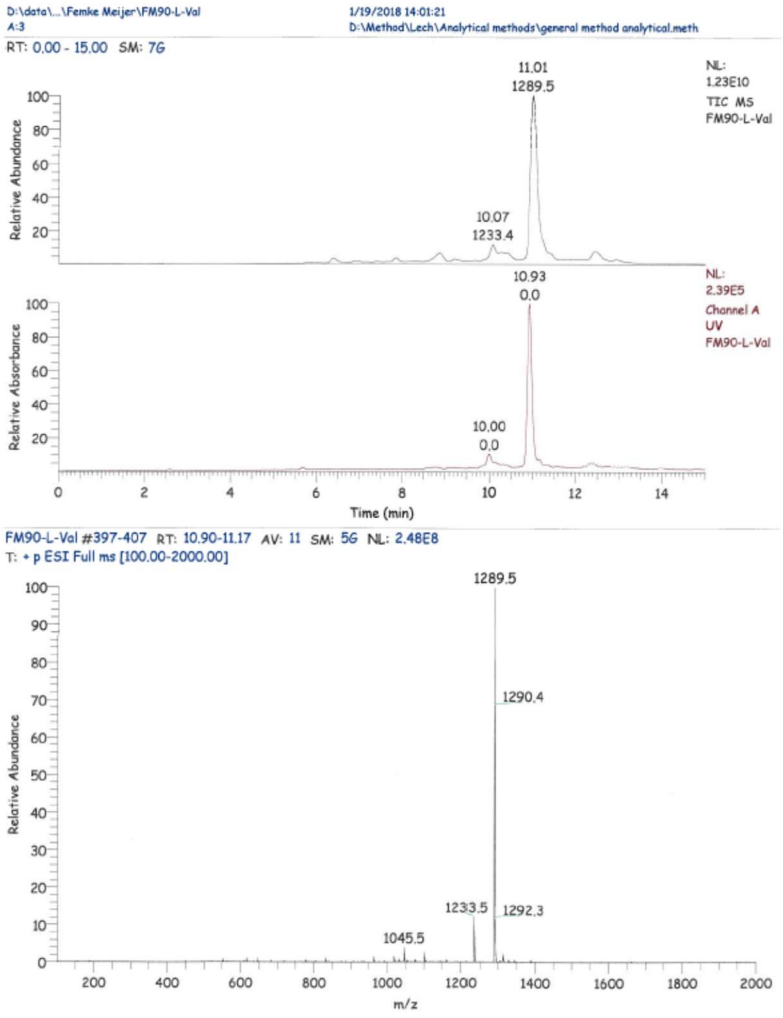

Figure S114. LC-MS (Method B) of partially protected Tau peptide 3.1f.

LC-MS (ESI): calc. for $C_{60}H_{93}N_{11}O_{17}S_1P_1$ $[M+H]^+$: 1289.62, observed 1289.50.

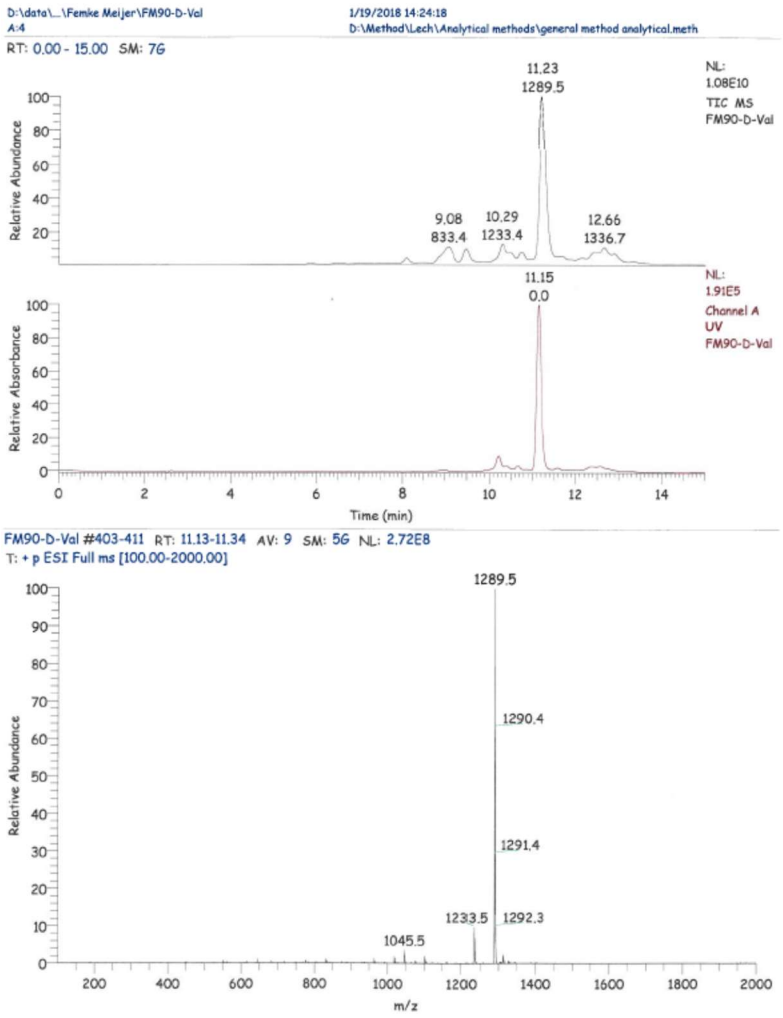

Figure S115. LC-MS of purified tau inhibitor 3.2a.

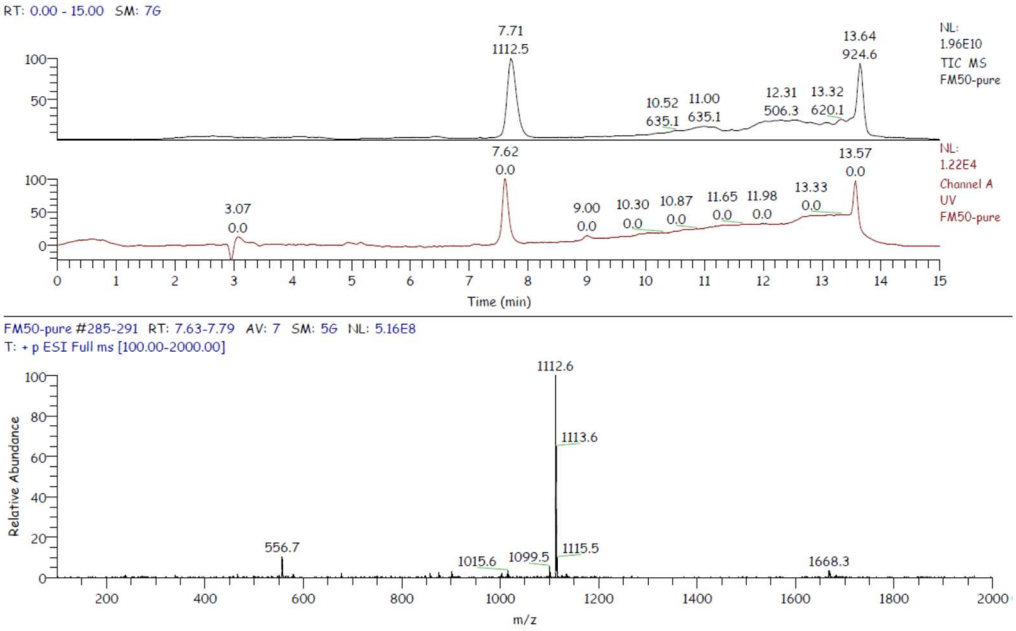

Figure S116. LC-MS of purified tau inhibitor 3.2b.

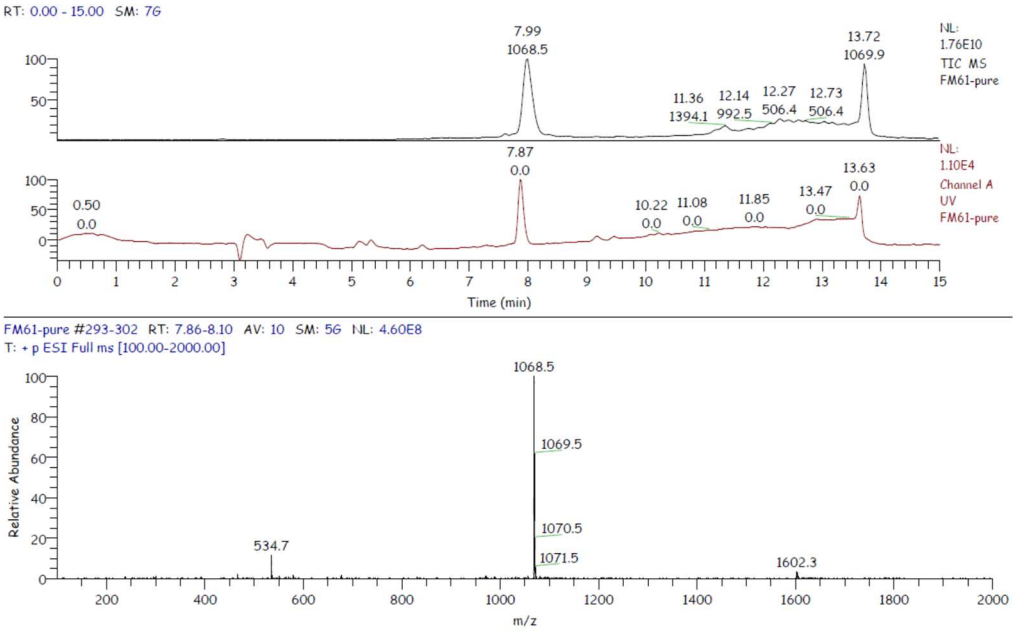

Figure S117. LC-MS of purified tau inhibitor 3.2c.

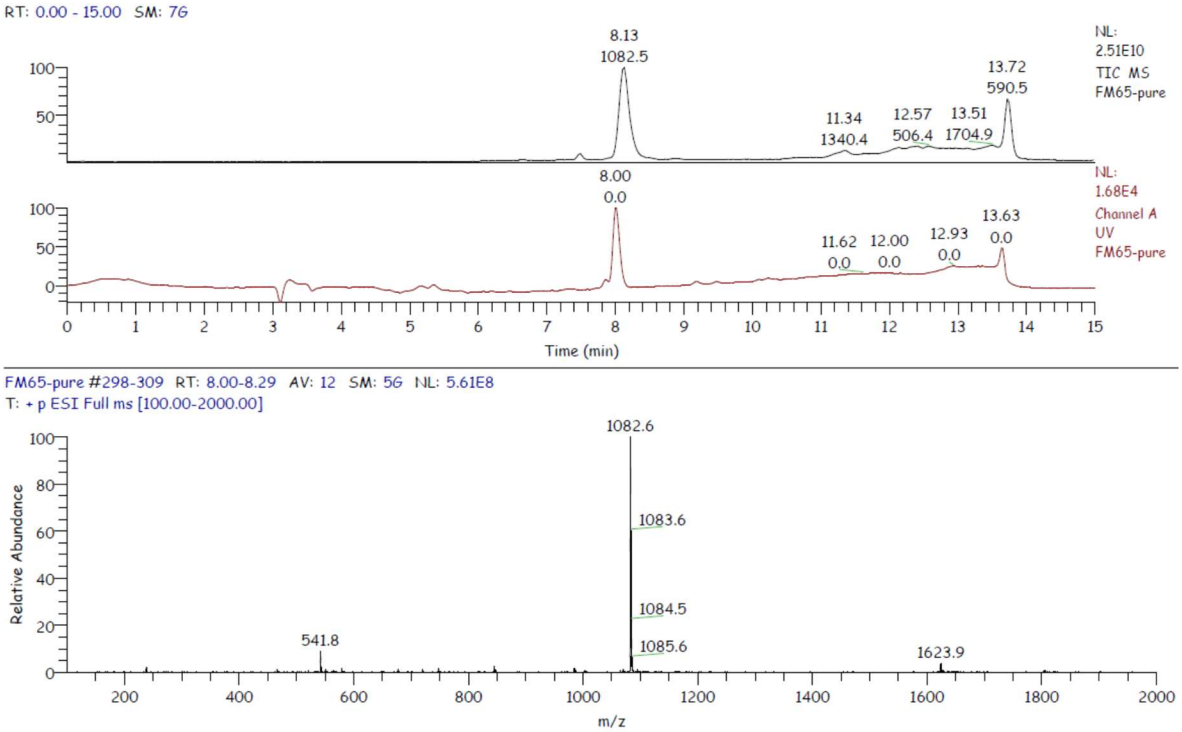

Figure S118. LC-MS of purified tau inhibitor 3.2d.

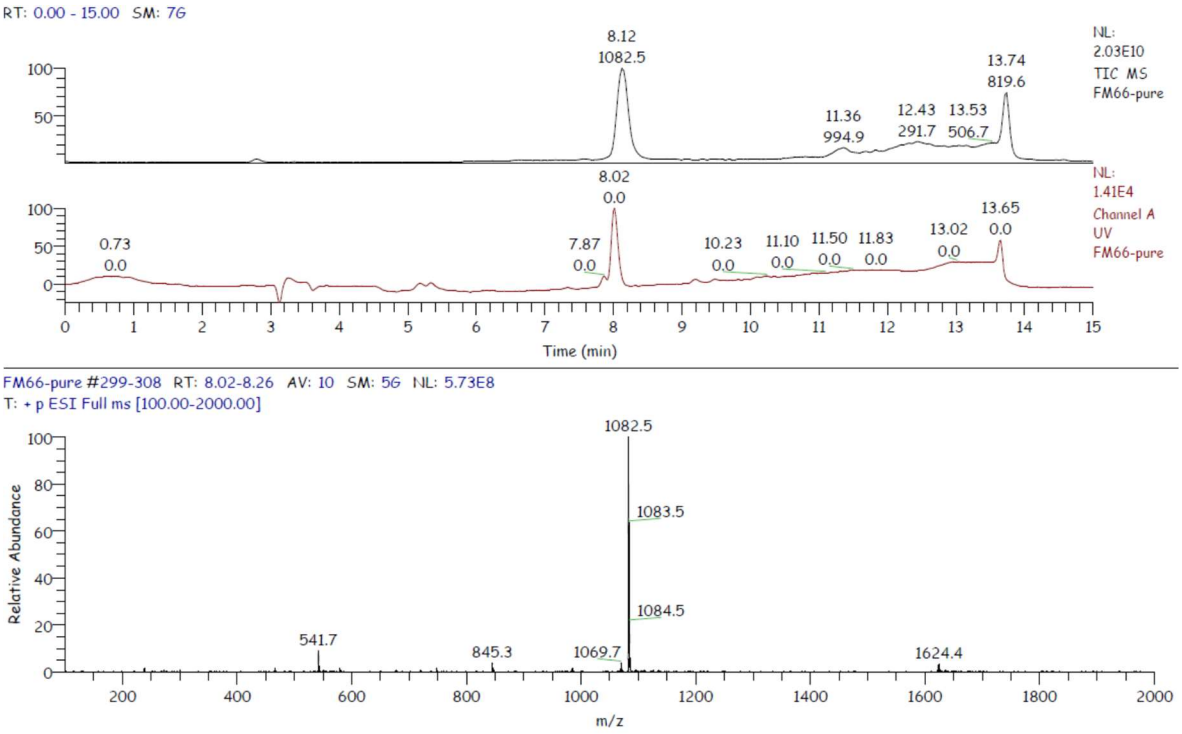

Figure S119. LC-MS of purified tau inhibitor 3.2e.

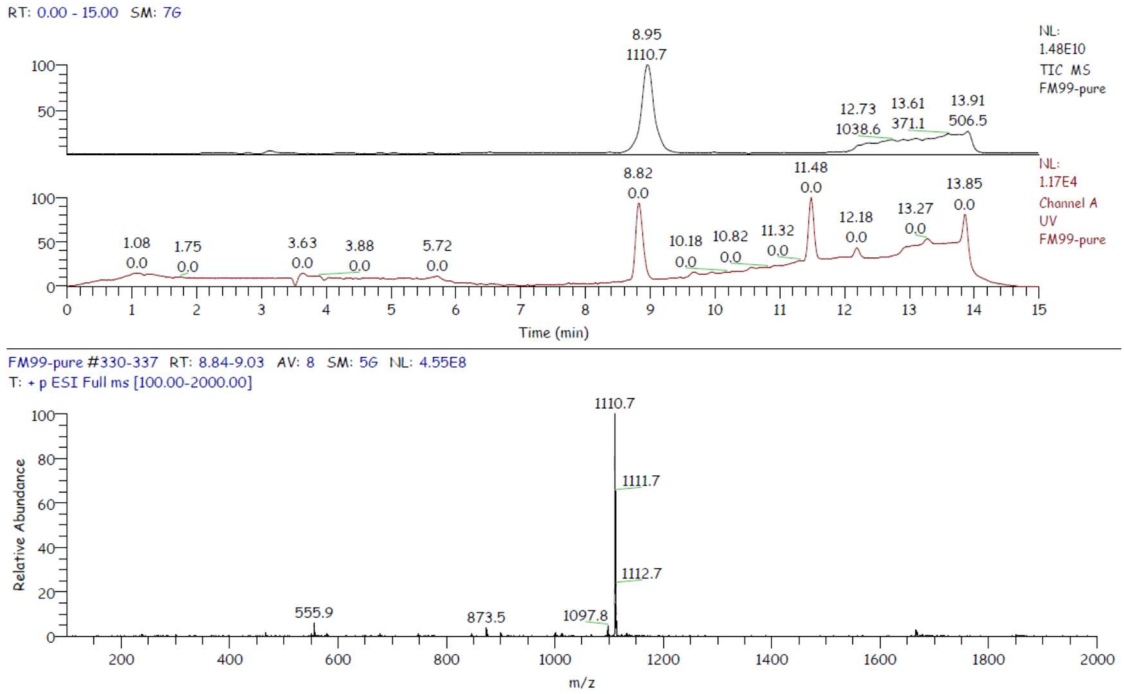

Figure S120. LC-MS of purified tau inhibitor 3.2f.

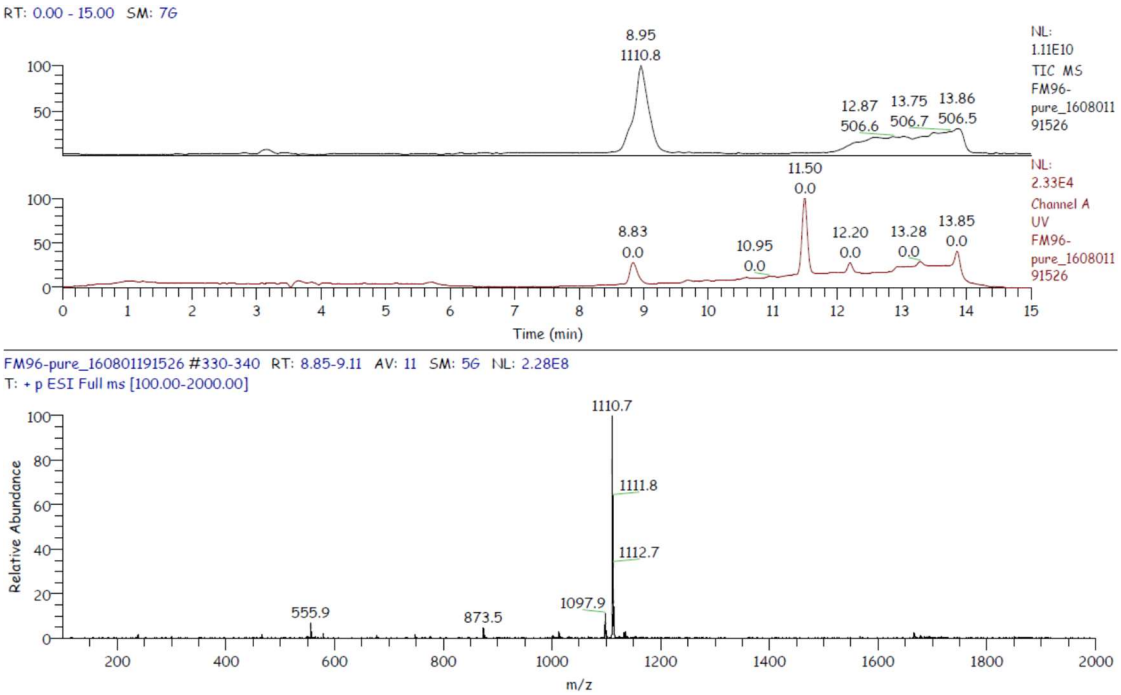

Figure S121. LC-MS of purified tau inhibitor 4.2a.

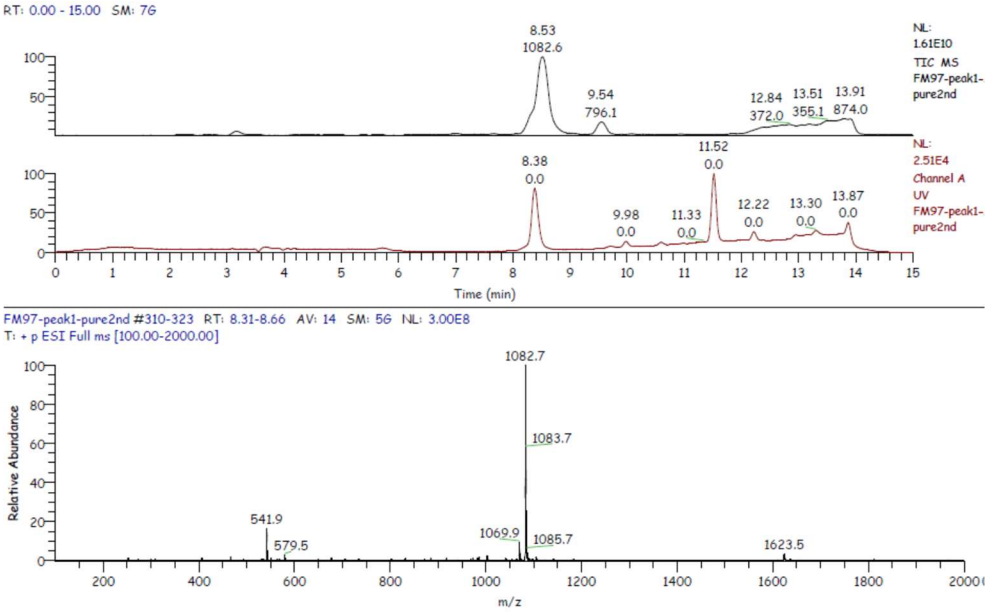

Figure S122. LC-MS of purified tau inhibitor 4.2b.

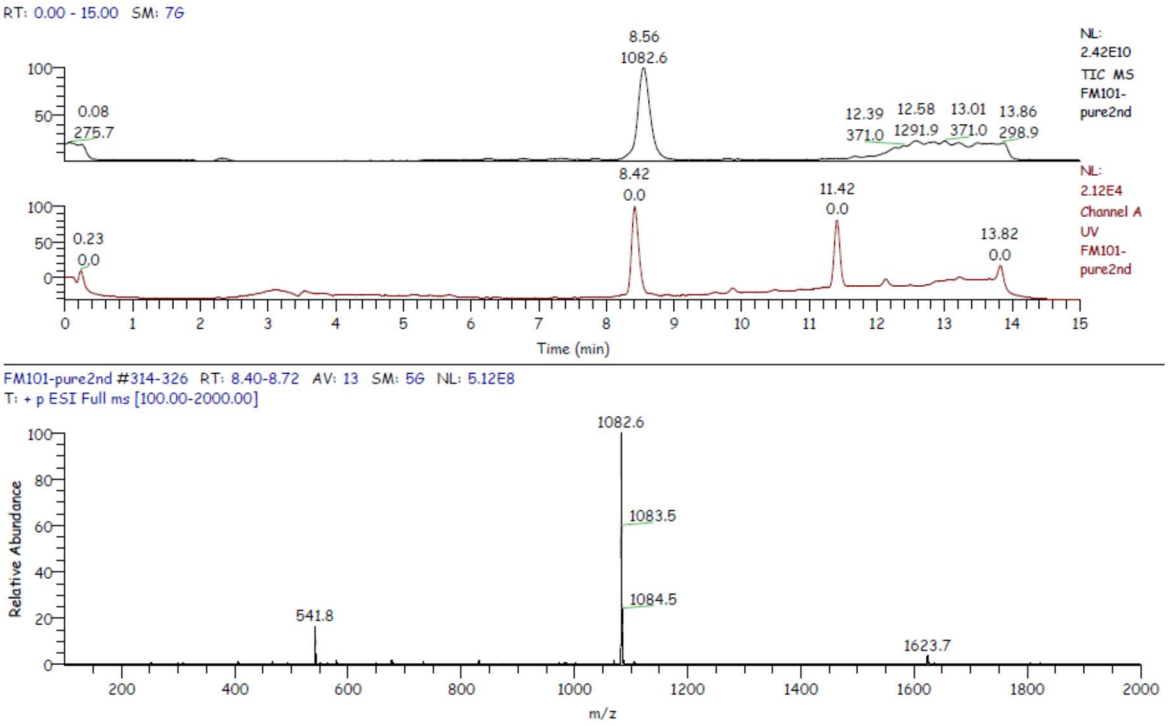

Figure S123. LC-MS of purified tau inhibitor 4.2c-I.

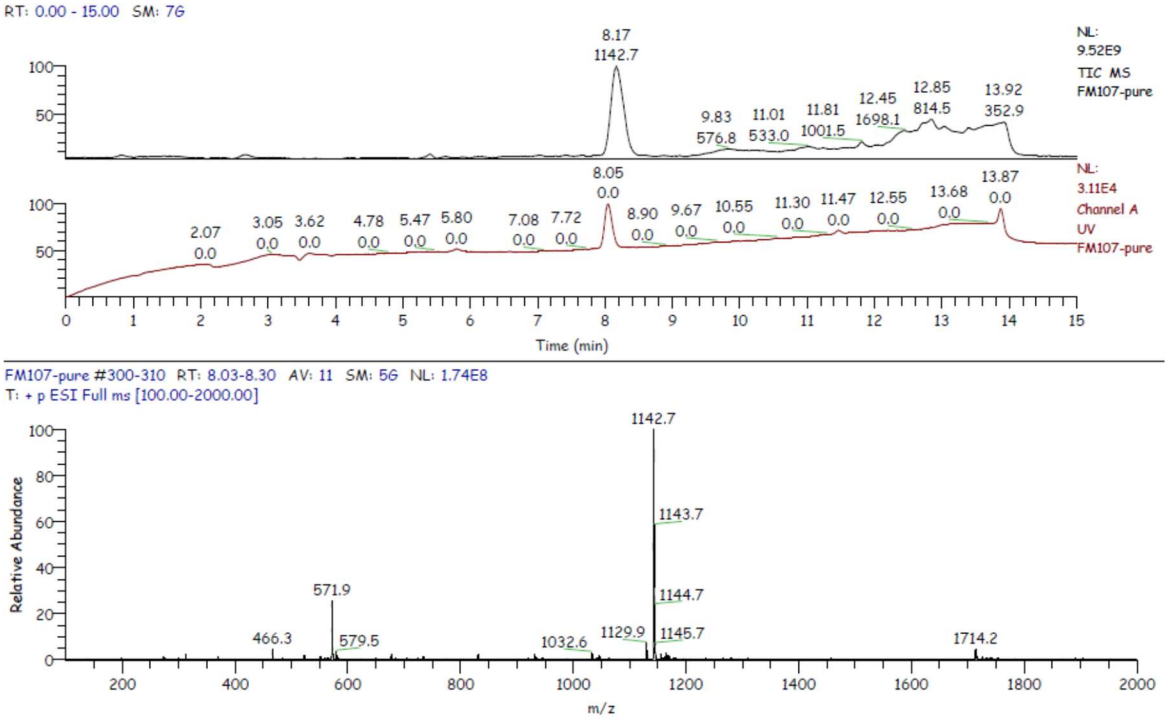

Figure S124. LC-MS of purified tau inhibitor 4.2c-II.

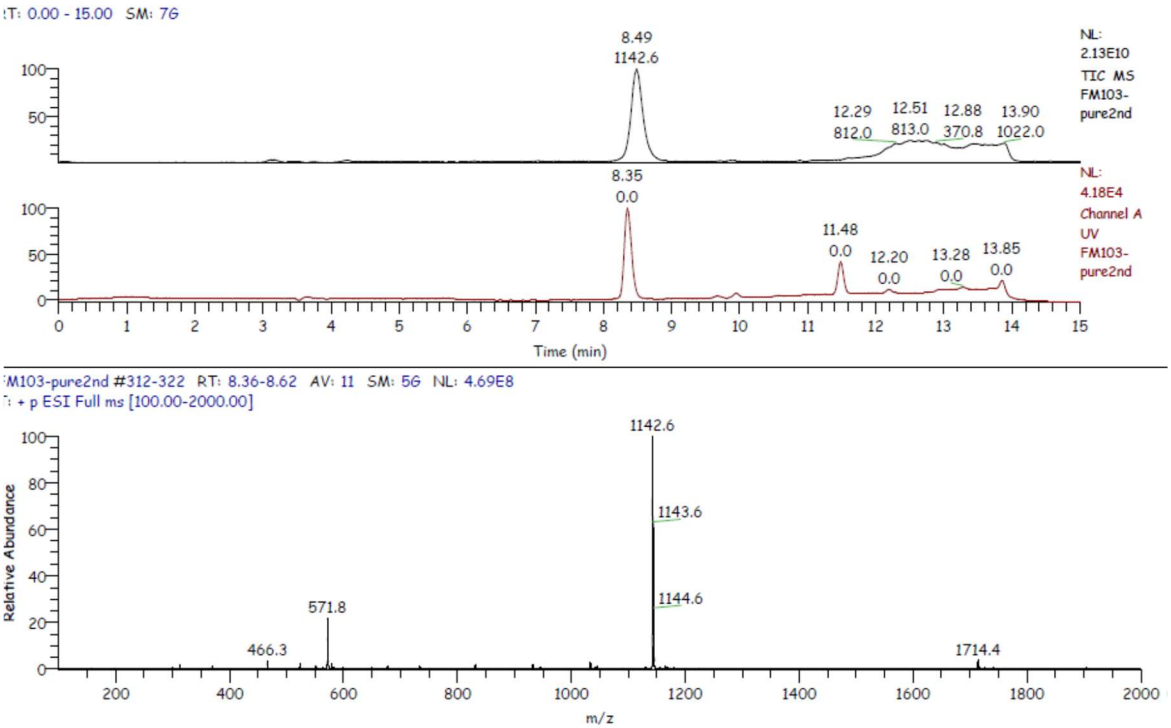

Figure S125. LC-MS of purified tau inhibitor 4.2d-I.

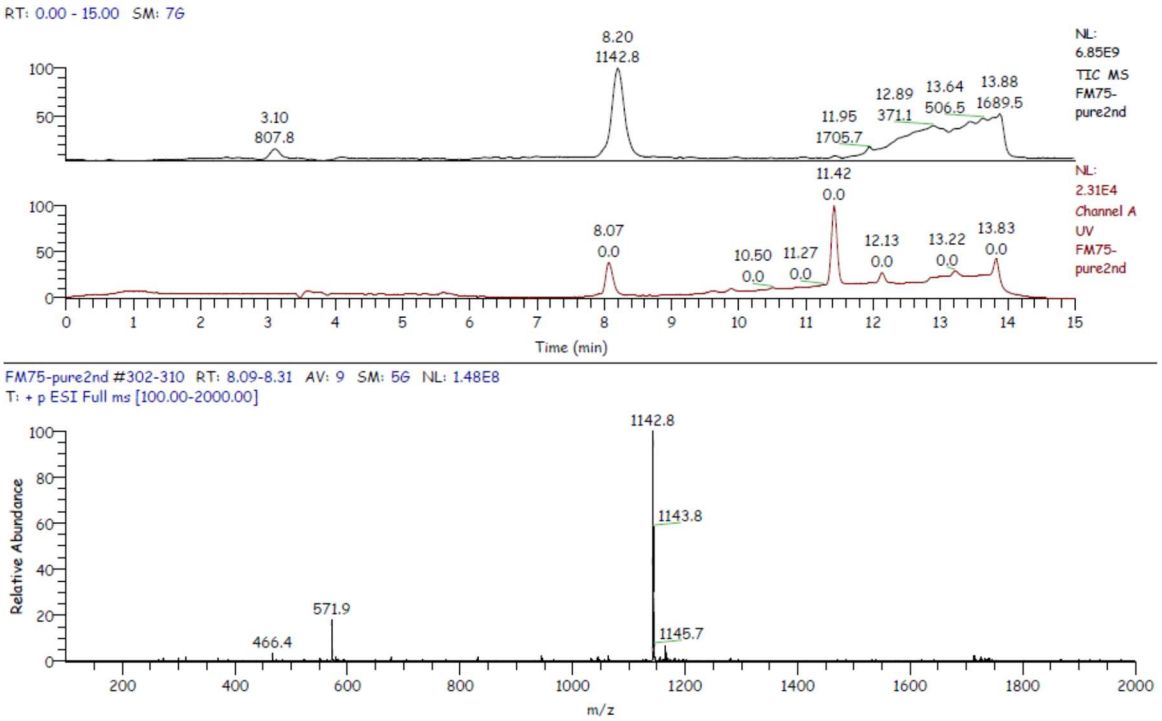

Figure S126. LC-MS of purified tau inhibitor 4.2d-II.

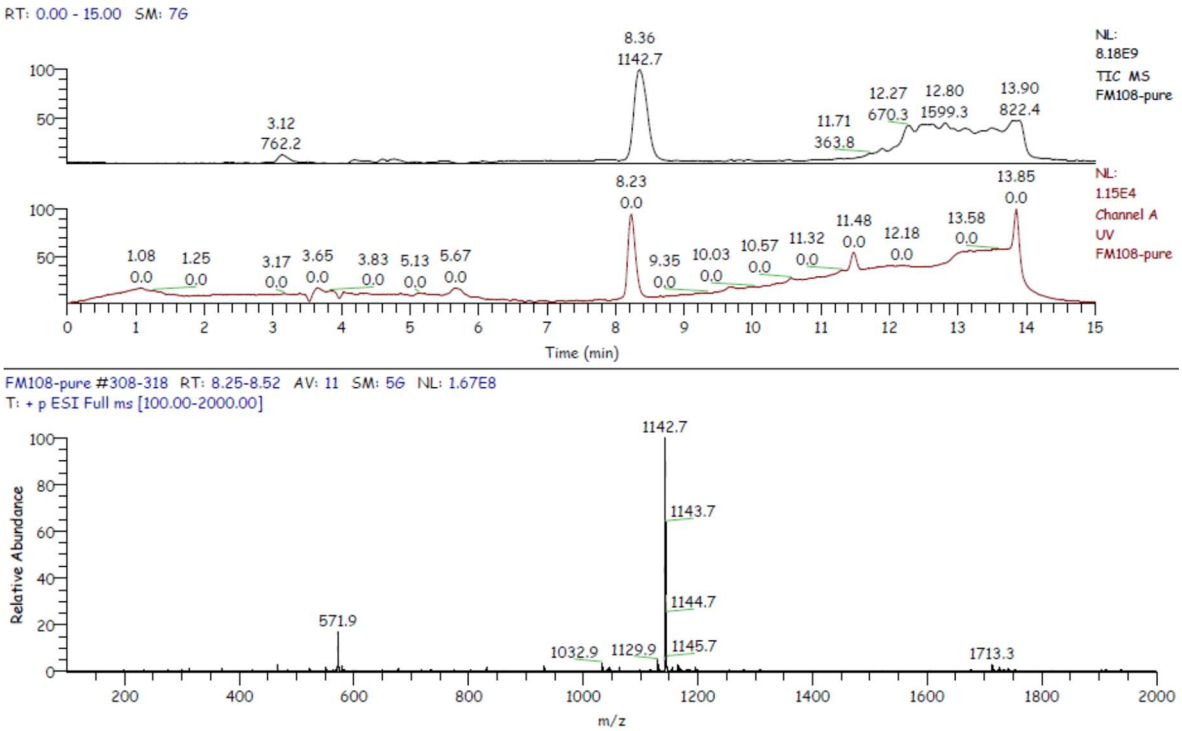

Figure S127. LC-MS of purified tau inhibitor 4.2e-I.

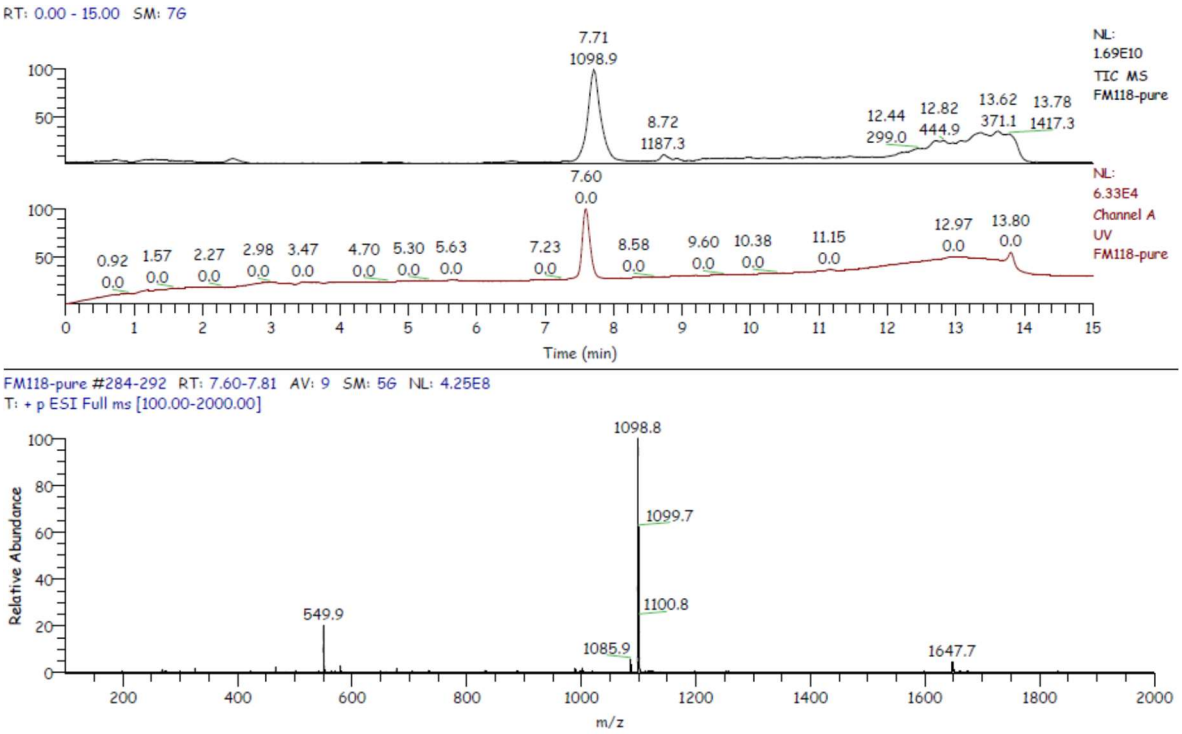

Figure S128. C-MS of purified tau inhibitor 4.2e-II.

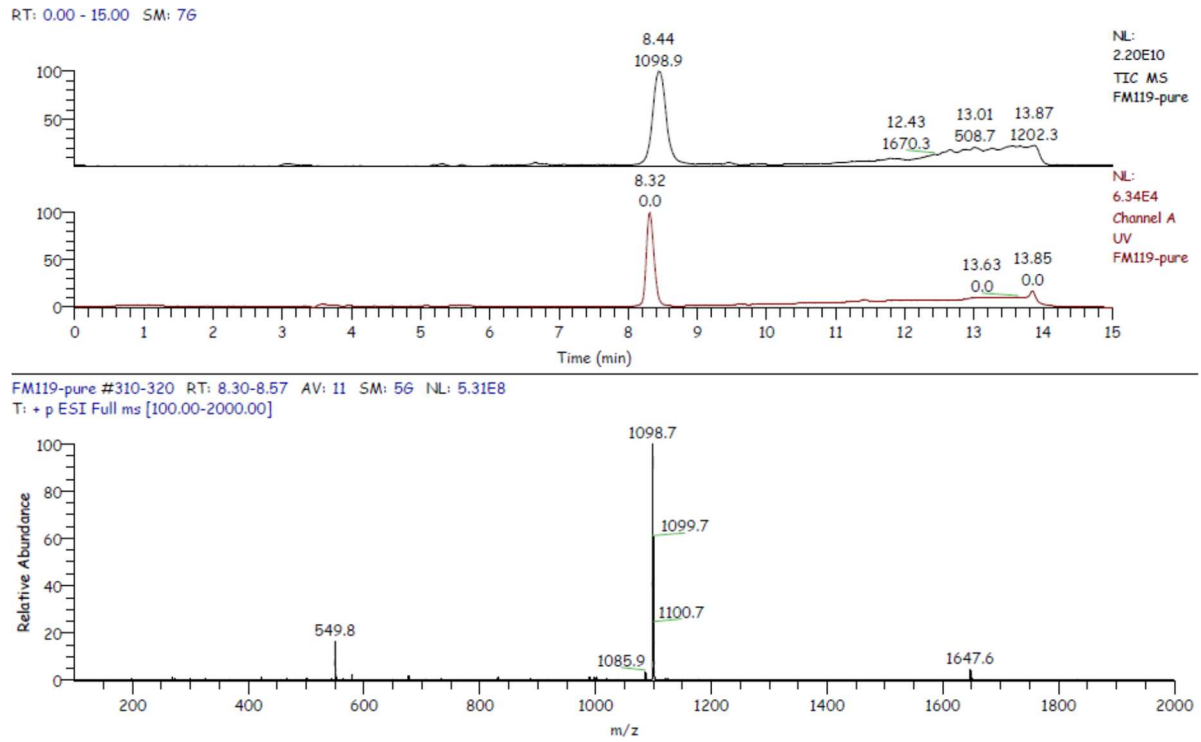

Figure S129. LC-MS of purified tau inhibitor 4.2f-I.

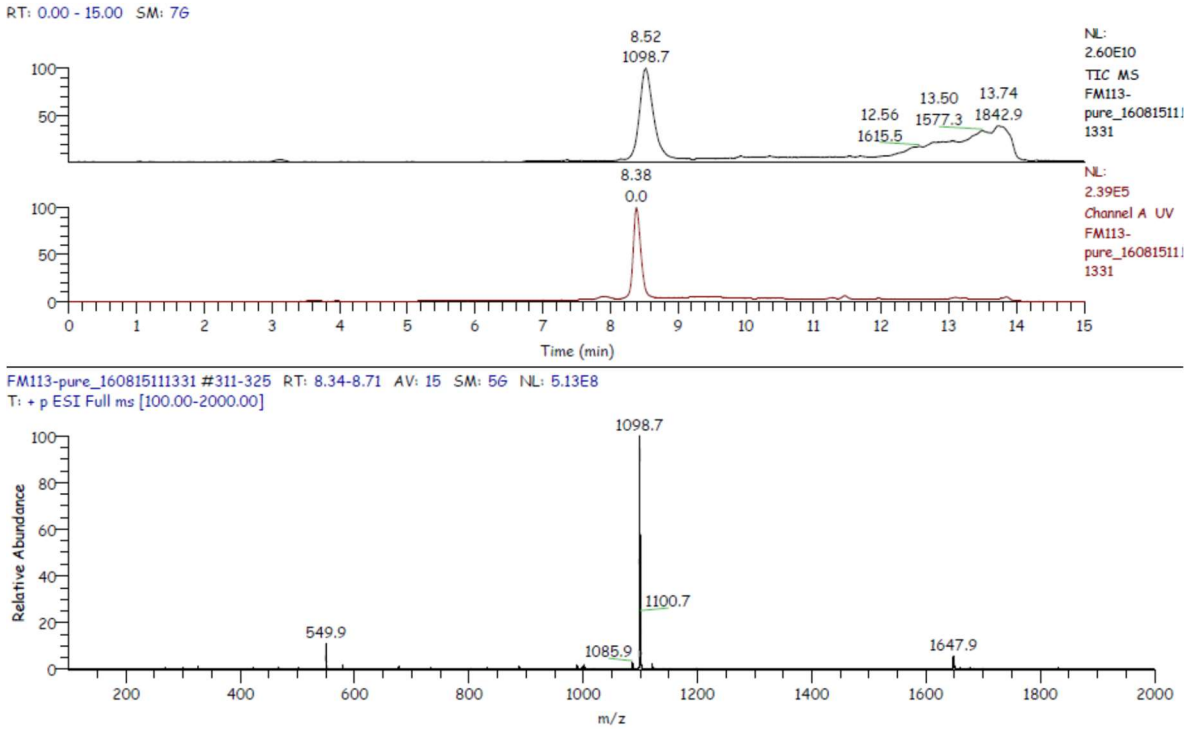

Figure S130. LC-MS of purified tau inhibitor 4.2f-II.

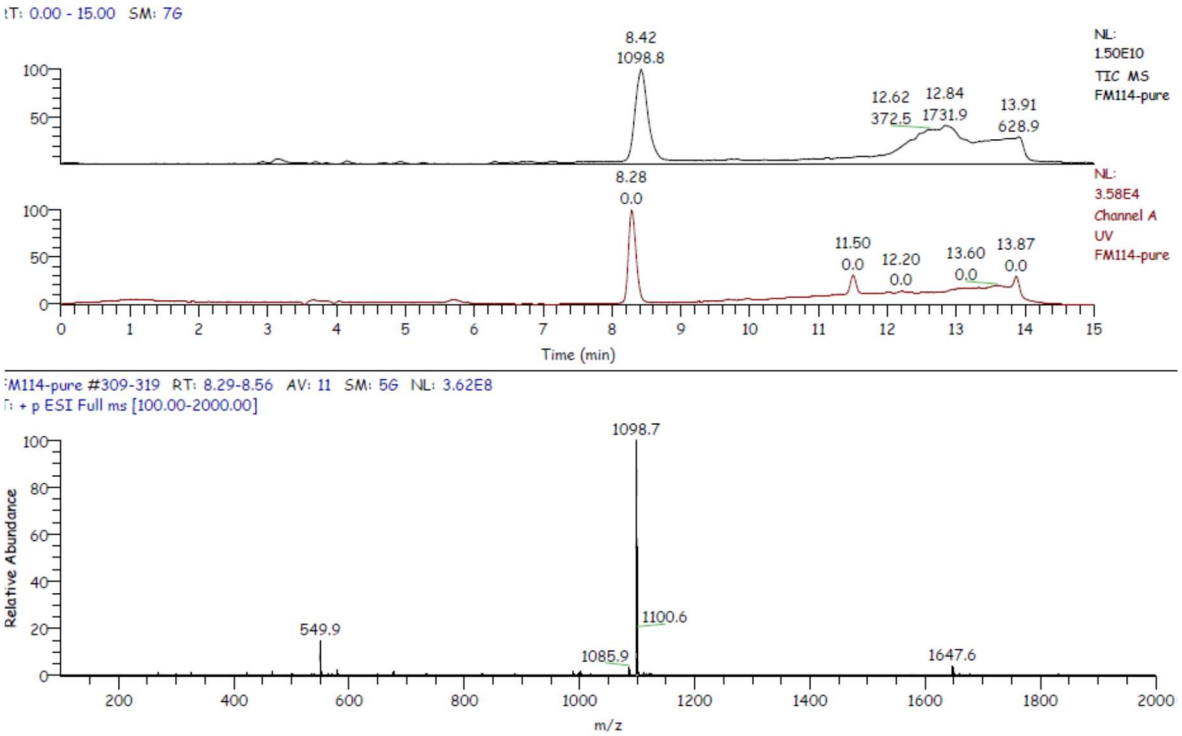

Figure S131. LC-MS of purified tau inhibitor 4.2g.

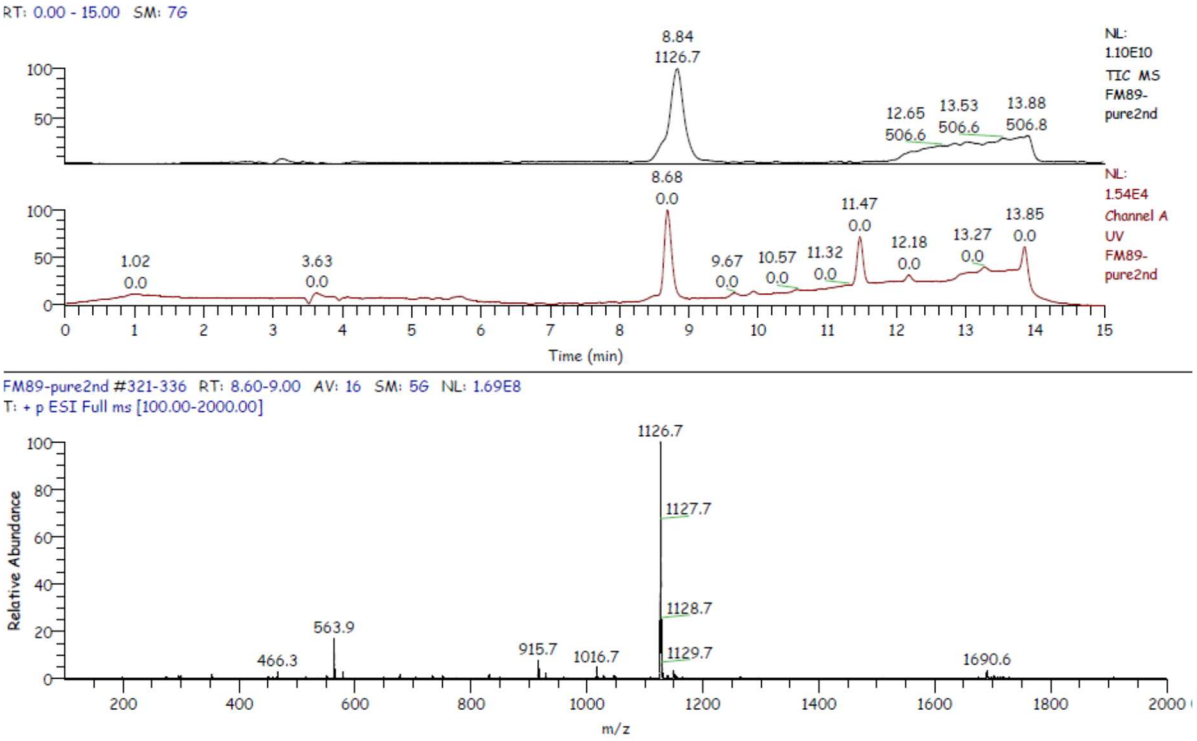

References

(1) Milroy, L.-G.; Bartel, M.; Henen, M. A.; Leysen, S.; Adriaans, J. M. C.; Brunsveld, L.; Landrieu, I.; Ottmann, C. Stabilizer-Guided Inhibition of Protein-Protein Interactions. *Angew. Chem. Int. Ed Engl.* **2015**, *54* (52), 15720–15724.

(2) Karplus, P. A.; Diederichs, K. Linking Crystallographic Model and Data Quality. *Science* **2012**, *336* (6084), 1030–1033.

(3) Burkhardt, A.; Pakendorf, T.; Reime, B.; Meyer, J.; Fischer, P.; Stübe, N.; Panneerselvam, S.; Lorbeer, O.; Stachnik, K.; Warmer, M.; et al. Status of the Crystallography Beamlines at PETRA III. *Eur. Phys. J. Plus* **2016**, *131* (3), 56.

(4) Meents, A.; Reime, B.; Stuebe, N.; Fischer, P.; Warmer, M.; Goeries, D.; Roever, J.; Meyer, J.; Fischer, J.; Burkhardt, A.; et al. Development of an In-Vacuum x-Ray Microscope with Cryogenic Sample Cooling for Beamline P11 at PETRA III; International Society for Optics and Photonics, 2013; Vol. 8851, p 88510K.

(5) Evans, P. R.; Murshudov, G. N. How Good Are My Data and What Is the Resolution? *Acta Crystallogr. D Biol. Crystallogr.* **2013**, *69* (7), 1204–1214.

(6) McCoy, A. J.; Grosse-Kunstleve, R. W.; Adams, P. D.; Winn, M. D.; Storoni, L. C.; Read, R. J. Phaser Crystallographic Software. *J. Appl. Crystallogr.* **2007**, *40* (4), 658–674.

(7) Emsley, P.; Cowtan, K. Coot: Model-Building Tools for Molecular Graphics. *Acta Crystallogr. D Biol. Crystallogr.* **2004**, *60* (12), 2126–2132.

(8) Adams, P. D.; Afonine, P. V.; Bunkóczi, G.; Chen, V. B.; Davis, I. W.; Echols, N.; Headd, J. J.; Hung, L.-W.; Kapral, G. J.; Grosse-Kunstleve, R. W.; et al. PHENIX: A Comprehensive Python-Based System for Macromolecular Structure Solution. *Acta Crystallogr. D Biol. Crystallogr.* **2010**, *66* (2), 213–221.